



Theses and Dissertations

2013-03-20

Microfabrication Processes and Advancements in Planar Electrode Ion Traps as Mass Spectrometers

Brett Jacob Hansen
Brigham Young University - Provo

Follow this and additional works at: <https://scholarsarchive.byu.edu/etd>



Part of the [Electrical and Computer Engineering Commons](#)

BYU ScholarsArchive Citation

Hansen, Brett Jacob, "Microfabrication Processes and Advancements in Planar Electrode Ion Traps as Mass Spectrometers" (2013). *Theses and Dissertations*. 3479.
<https://scholarsarchive.byu.edu/etd/3479>

This Dissertation is brought to you for free and open access by BYU ScholarsArchive. It has been accepted for inclusion in Theses and Dissertations by an authorized administrator of BYU ScholarsArchive. For more information, please contact scholarsarchive@byu.edu, ellen_amatangelo@byu.edu.

Microfabrication Processes and Advancements in Planar Electrode
Ion Traps as Mass Spectrometers

Brett J. Hansen

A dissertation submitted to the faculty of
Brigham Young University
in partial fulfillment of the requirements for the degree of

Doctor of Philosophy

Aaron R. Hawkins, Chair
Daniel E. Austin
Stephen M. Schultz
Milton L. Lee
Karl F. Warnick

Department of Electrical and Computer Engineering

Brigham Young University

March 2013

Copyright © 2013 Brett J. Hansen

All Rights Reserved

ABSTRACT

Microfabrication Processes and Advancements in Planar Electrode Ion Traps as Mass Spectrometers

Brett J. Hansen

Department of Electrical and Computer Engineering, BYU
Doctor of Philosophy

This dissertation presents advances in the development of planar electrode ion traps. An ion trap is a device that can be used in mass analysis applications. Electrode surfaces create an electric field profile that trap ionized molecules of an analyte. The electric fields can then be manipulated to mass-selectively eject ions out of the trap into a detector. The resulting data can be used to analyze molecular structure and composition of an unknown compound.

Conventional ion traps require machined electrode surfaces to form the electric trapping field. This class of electrode presents significant obstacles when attempting to miniaturize ion traps to create portable mass spectrometers. Machined electrodes lose required precision in shape, smoothness, and alignment as trapping dimensions decrease. Simplified electrode geometries are essential to open the way to miniaturized ion traps.

The planar electrode ion trap presents a simplified geometry that utilizes photolithography processes in its fabrication. Patterns of electrodes are patterned on a planar ceramic substrate. Electric fields generated by these patterns can be nearly identical to those of ideal ion traps. The microfabrication processes involve the challenge of patterning on ceramic, patterning on two sides of a substrate, and patterning on a substrate with high topographic features.

Four successful designs of planar ion traps are presented in this work: the planar Paul, toroidal, coaxial, and linear ion trap. These four designs have different strengths and weaknesses. The planar Paul trap is simpler to design and operate, the toroidal has a larger ion storage volume and so can be a more sensitive instrument, and the coaxial trap is a hybrid planar Paul and toroidal trap. The linear trap combines the simplicity of the planar Paul trap with the increased storage capacity of the toroidal trap. This work presents how these four designs advance work in miniaturized ion traps. In addition, microfabrication techniques and trap performance for these designs are presented.

Keywords: Brett Hansen, mass spectrometry, ion trap, microfabrication, lithography, high topography, toroidal ion trap, linear ion trap, MEMS

ACKNOWLEDGEMENTS

I would like to express gratitude to those that have been instrumental to the success in my career. In particular, I am grateful for the support of my advisor, Dr. Aaron R. Hawkins. Dr. Hawkins has been a mentor to me since early in my undergraduate career. His mentorship and advice have been vital in guiding me through my career as a student, researcher, and engineer.

I also would like to express thanks to Dr. Daniel E. Austin. Dr. Austin has helped guide me in learning all I know about ion traps. I am grateful for the opportunities for learning and growth that he provided me. He has given me invaluable support and guidance as I have progressed in my career.

I also am grateful for the other members of my committee: Dr. Stephen M. Schultz, Dr. Milton L. Lee, and Dr. Karl F. Warnick. They have all aided my education and progress. I am grateful for their willingness to provide assistance to me.

I have also been fortunate to work with several helpful colleagues in this work. These include Dr. Ying Peng, Dr. Miao Wang, Dr. Zhiping Zhang, Dr. Jeffrey Maas, Hannah Quist, and Richard Niemi. Working with these individuals gave me valuable team and leadership experience.

Finally, I am particularly grateful for my wife, Rebecca. She has been a constant source of encouragement for me. The successful conclusion of this work can be attributed to her support.

TABLE OF CONTENTS

LIST OF TABLES	ix
LIST OF FIGURES	x
1 INTRODUCTION	1
1.1 Introduction	1
1.2 Contributions	3
1.3 Organization	5
References	5
2 ION TRAP THEORY	9
2.1 Ion Trap Theory	9
2.2.1 Mathieu Equations	11
2.2.2 Ion Stability Diagram	14
2.2.3 Secular Frequencies	18
2.2.4 Potential Well Depth	20
2.2.5 Higher Order Field Effects	21
2.2 Benchmarks of Ion Trap Performance	23
2.2.1 Mass Resolution	23
2.2.2 Signal to Noise Ratio	23
2.2.3 Mass Range	23
2.3 Ion Trap Development	24

2.3.1 Early Ion Trap History	24
2.3.2 Mass Filters	25
2.3.3 Cylindrical Traps	26
2.3.4 Toroidal Traps.....	27
2.3.5 Linear Traps.....	29
2.4 Linear Ion Trap Specific Theory.....	31
References.....	34
3 MINIATURIZATION EFFORTS IN ION TRAPS	38
3.1 Motivations for Miniaturization.....	38
3.2 Effects of Trap Miniaturization on System Size and Design.....	39
3.2.1 Benefits of Miniaturization	39
3.2.2 Challenges of Miniaturization.....	40
3.3 Miniaturization Techniques	42
3.3.1 Conventionally Machined Devices	42
3.3.2 Microfabrication Techniques with Quadrupolar Devices.....	44
3.4 Discrete Patterned Planar Electrode Traps	50
References.....	53
4 ION TRAP FABRICATION	59
4.1 Development History	59
4.2 Current Designs	71

4.3 Multiple Trap Designs	73
4.4 Microfabrication Technique.....	74
4.4.1 Prominent Challenges	76
4.4.2 Microfabrication Process	81
References.....	83
5 THE TOROIDAL, PAUL, AND COAXIAL TRAPS.....	85
5.1 The Toroidal Trap.....	85
5.1.1 Radial Ejection.....	85
5.1.2. Axial Ejection	90
5.2 The Planar Paul Trap	94
5.2.1 Field Design.....	97
5.2.2 Results.....	98
5.3 The Coaxial Trap	103
5.3.1 Field Design.....	107
5.3.2 Results.....	110
References.....	112
6 THE PLANAR LINEAR ION TRAP.....	114
6.1 Introduction.....	114
6.2 Field Design.....	117
6.3 Experimental Setup.....	123

6.3.1 Trap Assembly	123
6.3.2 Equipment Specifications	125
6.3.3 Experimental Parameters	127
6.4 Results.....	129
6.4.1 Frequency Sweep.....	129
6.4.2 Amplitude Ramp.....	132
6.5 Miniaturized Trap Spacing	135
6.5.1 Theory and Simulation.....	135
6.5.2 Experimental Investigations with the PLIT	137
References.....	138
7 CONCLUSIONS AND FUTURE WORK	140
7.1 Conclusions.....	140
7.2 Future Work	141
References.....	147
APPENDIX A – PUBLICATION LIST.....	149
Papers	149
Conference Proceedings.....	150
Publications unrelated to Ion Traps	152
APPENDIX B – MICROFABRICATION RECIPES	153
B.1 Plate Cleaning	153

B.2 Metal Deposition	153
B.3 Lithography	156
B.4 Specialized Spin Recipes	158
B.4.1 Toroidal Trap (large central hole)	158
B.4.2 Toroidal Trap (slit design).....	158
B.4.3 Linear Trap	158
APPENDIX C – GERMANIUM AND MULTIPOLE CALCULATION CONVENTIONS....	159
C.1 SIMION.....	159
C.2 Matlab.....	160
C.3 Sample MATLAB code	160

LIST OF TABLES

Table 5.1: The electrode layout of the axial-ejection toroidal ion trap.....	91
Table 5.2: RF potentials applied to the specific rings of the 24 ring ceramic to create the coaxial trap.....	109
Table 6.1: Locations of the electrodes on the PLIT.....	115
Table 6.2: Calculated equations for the curves in Figure 6-4.	118

LIST OF FIGURES

Figure 2-1: A representation of the quadrupole field.....	10
Figure 2-2: (top) (bottom) Hyperbolic electrode arrangement of the quadrupole ion trap. (bottom) Contour plot of the electric field generated between electrodes.....	11
Figure 2-3: Solutions of the Mathieu equation in the r and z directions. Figure adapted from “An Introduction to Quadrupole Ion Trap Mass Spectrometry,” <i>J. Mass Spectrom.</i> 32, pp. 351-369, 1997.....	16
Figure 2-4: Overlapping of the r and z stability regions, with the primarily used stability region indicated. Figure adapted from “An Introduction to Quadrupole Ion Trap Mass Spectrometry,” <i>J. Mass Spectrom.</i> 32, pp. 351-369, 1997.....	16
Figure 2-5: The ion stability diagram of the quadrupole ion trap. Figure adapted from “An Introduction to Quadrupole Ion Trap Mass Spectrometry,” <i>J. Mass Spectrom.</i> 32, pp. 351-369, 1997.....	17
Figure 2-6: Various ion masses m are depicted on a stability diagram. (top) A representation of ion ejection using the boundary of the stability diagram. (bottom) A representation of ion ejection by resonant excitation at secular frequencies.....	19
Figure 2-7: The original ion trap developed by Wolfgang Paul. Figure from http://big.physics-astro.uni-bonn.de/index.php?id=76	24
Figure 2-8: A quadrupole mass filter. Diagram from Dr. Paul Gates, University of Bristol (http://www.bris.ac.uk/nerclsmsf/techniques/gcms.html)	26
Figure 2-9: (top) A cylindrical ion trap. (bottom) The similarity of electric field profiles between the Paul trap, on the left, and the CIT, on the right.	27
Figure 2-10: The arrangement of electrodes in a toroidal ion trap and their relationship to the Paul trap arrangement. Figure adapted from “Design, optimization and initial performance of a toroidal rf ion trap mass spectrometer,” <i>Int. J. Mass Spectrom.</i> , 212, pp. 25-40, 2001.	28
Figure 2-11: A standard linear ion trap. Figure adapted from “A two-dimensional quadrupole ion trap mass spectrometer,” <i>J. Amer. Soc. Mass Spec.</i> , 13, pp. 659-669, 2002.	30
Figure 2-12: The rectilinear ion trap electrode arrangement.	31
Figure 2-13: Relationship of effective potentials for multipole components of LIT trapping field. Figure from “Linear ion traps in mass spectrometry,” <i>Mass Spectrom. Rev.</i> , 24, pp. 1-29, 2005.	33
Figure 3-1: Development paths from the original Paul trap that allow for miniaturized traps.....	43

Figure 3-2: (left) An arrayed RIT structure. (right) Electrical field created by the four trapping regions, where each slit in the surface either helps create the electric field profile and provide a path for ion ejection or separates the different trapping regions. Figure from “Ion Trap Array Mass Analyzer: Structure and Performance,” <i>Anal. Chem.</i> , 81, pp. 4840-4846, 2009.....	44
Figure 3-3: A MEMS based approach to a quadrupole device. Figure from “Fabrication of a Microengineered Quadrupole Electrostatic Lens,” <i>Electron. Lett.</i> , 32, pp. 2094-2095, 1996.....	45
Figure 3-4: The out-of-plane approach to microfabricating a quadrupole mass filter. Figure from “An Application of 3-D MEMS Packaging: Out-of-Plane Quadrupole Mass Filters,” <i>J. Microelectromechanical Sys.</i> , 17, pp. 1430-1438, 2008.....	46
Figure 3-5: (left) A microfabricated CIT array. (right) Cross-sectional view. (unpublished photos).....	47
Figure 3-6: The coaxial ring ion trap. Figure from “Microelectromechanical System Assembled Ion Optics: An Advance to Miniaturization and Assembly of Electron and Ion Optics,” <i>Rev. Sci. Instrum.</i> , 80, p. 093302, 2009.....	48
Figure 3-7: A circular array of polymer based miniaturized RITs. (top) Schematic view of the electrode arrangement. (bottom) Trap array assembly. Figure from “Circular arrays of polymer-based miniature rectilinear ion traps,” <i>Analyst</i> , 134, pp. 1338-1347, 2009.	49
Figure 3-8: Single plate ion trap. (left) Schematic view of the trapping surface. (right) A cross-sectional view of the electric field profile using one, two, and three rings. Figure from “Planar Geometry for Trapping and Separating Ions and Charged Particles,” <i>Anal. Chem.</i> , 79, pp. 6857-6861, 2007.....	50
Figure 3-9: (top) A planar electrode pattern for creating a planar Paul trap. (bottom) A planar electrode pattern for creating an LIT type trap.	52
Figure 4-1: The ion trap array on silicon. (top) Completed wafer substrate. (bottom) Electrode arrangement and ion storage areas are shown.	60
Figure 4-2: The second generation of the silicon-etched trap array.	62
Figure 4-3: (left) A cross-sectional view of an individual trapping electrode geometry. (right) A microscope picture taken of the etched hole.....	63
Figure 4-4: The metal on silicon ring design.	64
Figure 4-5: (top) Arrangement of the metal on silicon toroidal trap. (bottom) A cross-sectional view of the contour plot of the trapping field.	65
Figure 4-6: A cross-sectional view of the fabrication process for the metal on silicon trap. (a) Metal deposited on silicon with an oxide layer, (b) metal patterned into RF leads, (c)	

oxide grown as an insulative layer, (d) vias etched into the oxide, (e) rings patterned onto the substrate, (f) resistive germanium layer deposited over the rings.....	66
Figure 4-7: (left) Patterning of rings on ceramic substrate. (right) Finished substrate after depositing germanium over rings.....	68
Figure 4-8: Fabrication process for the first design to incorporate back-side packaging.	69
Figure 4-9: The circuit representation for the back-side packaging design.....	69
Figure 4-10: Schematic diagram illustrating the PCB/Plate Assembly	72
Figure 4-11: Back side metal patterning on ceramic, germanium covering the trapping side, and a populated PCB forming the plate/PCB assembly.	72
Figure 4-12: Schematic view of the entire trap assembly.....	73
Figure 4-13: Most recent electrode layouts for four trap designs.....	75
Figure 4-14: An over etched via, with the height being demonstrated by the difference in the depth of focus in the microscope.	77
Figure 4-15: Photoresist application when spinning resist over a deep via. Figure adapted from “Lithographic Challenges and Solutions for 3D Interconnect,” in <i>Proc. IWLPC</i> , 2008.	78
Figure 4-16: Vias that are not covered in a thick metal layer. (left) A ring electrode that was supposed to run over the via. The photoresist pattern is seen, but it has not adhered to the via bottom, allowing metal etchant to etch away the metal connection. (right) A via that should be completely covered in metal.....	79
Figure 4-17: Photoresist streak and shadowing effects on the toroidal trap.....	79
Figure 4-18: Photoresist shadowing in the PLIT. The electrode around the slit should be a solid bar.....	80
Figure 4-19: Cross-section view of the fabrication steps for planar electrode surfaces. (a) bare aluminum oxide substrate; (b) ejection slit, alignment holes, and metal-filled vias formed; (c) metal deposited on both sides of substrate, photoresist spun on top side and painted on bottom side; (d) top side patterned by photolithography and etching; (e) photoresist spun on bottom side, photoresist painted on already-patterned side, and bottom side patterned and etched; (f) germanium layer deposited over top of trapping side of substrate. Figure adapted from “A Lithographically Patterned Discrete Planar Electrode Linear Ion Trap Mass Spectrometer,” <i>J. Microelectromech. Sys.</i> , (in press).	82
Figure 4-20: PLIT plate taped to 4” wafer for IML processing.....	83
Figure 5-1: Illustrated steps of mass analysis in the toroidal trap. (a) RF applied on plates, (b) sample ionized by way of electron gun, (c) ions stored in a toroidal region, (d) ions	

swept into detector by application of resonant ejection AC signal. Figure adapted from “Halo Ion Trap Mass Spectrometer,” <i>Anal. Chem.</i> 79, pp. 2927-2932, 2007.	86
Figure 5-2: Timing of control signals in the toroidal ion trap. Figure from “Halo Ion Trap Mass Spectrometer,” <i>Anal. Chem.</i> 79, pp. 2927-2932, 2007.	86
Figure 5-3: The toroidal trap for radial ion ejection. Figure from “Halo Ion Trap Mass Spectrometer,” <i>Anal. Chem.</i> , 79, pp. 2927-2932, 2007.	88
Figure 5-4: Potential function and electric field of the radial-ejection toroidal trap. Figure from “Halo Ion Trap Mass Spectrometer,” <i>Anal. Chem.</i> 79, 2927-2932, 2007.	88
Figure 5-5: Results from the radial-ejection toroidal trap. (a) dichloromethane, (b) toluene. Figure adapted from “Halo Ion Trap Mass Spectrometer,” <i>Anal. Chem.</i> , 79, pp. 2927-2932, 2007.	89
Figure 5-6: The axial-ejection toroidal trap.	90
Figure 5-7: The two methods for ion ejection used in the toroidal ion trap. (a) Radial ejection, (b) axial ejection. Figure from "Performance of a Halo Ion Trap Mass Analyzer with Exit Slits for Axial Ejection," <i>J. Am. Soc. Mass Spectrom.</i> 22, pp. 369-378, 2011.	91
Figure 5-8: Benzene spectra using different values of octopole. (a) 1%, (b) 3%, (c) 5%, (d) 7%. Figure from "Performance of a Halo Ion Trap Mass Analyzer with Exit Slits for Axial Ejection," <i>J. Am. Soc. Mass Spectrom.</i> , 22, pp. 369-378, 2011.	92
Figure 5-9: A measured dichloromethane spectrum with 5% octopole. Figure from "Performance of a Halo Ion Trap Mass Analyzer with Exit Slits for Axial Ejection," <i>J. Am. Soc. Mass Spectrom.</i> , 22, pp. 369-378, 2011.	93
Figure 5-10: The planar Paul trap electrode pattern.	94
Figure 5-11: The timing of signals controlling the Paul trap. Figure from “Paul Trap Mass Analyzer Consisting of Opposing Microfabricated Electrode Plates,” <i>Anal. Chem.</i> , 81, pp. 5241-5248, 2009.	96
Figure 5-12: Comparison of resolution ($m/\Delta m$, FWHM) and signal-to-noise (S/N) ratio for the m/z 43 and 58 ions of acetone using electric fields with different octopole/dodecapole combinations. These values are from individual spectra. Each data point represents the average of three measurements. Sample pressure: 10–5 Torr; ionization time: 4.0 ms; ac frequency: 345 kHz. Figure from “Effects of higher-order multipoles on the performance of a two-plate quadrupole ion trap mass analyzer,” <i>Int. J. Mass Spectrom.</i> , 299, pp 151-157, 2011.	100
Figure 5-13: Comparison of resolution ($m/\Delta m$, FWHM) for the m/z 84 and 86 ions of dichloromethane and the m/z 130 and 132 ions of trichloroethylene under the electric fields with different octopole/dodecapole combinations by using forward and reverse scan modes. These values are from individual spectra. Each data point represents the average of	

three measurements. Figure from “Effects of higher-order multipoles on the performance of a two-plate quadrupole ion trap mass analyzer,” <i>Int. J. Mass Spectrom.</i> , 299, pp. 151-157, 2011.....	101
Figure 5-14: Comparison of peak intensity for the m/z 84 and 86 ions of dichloromethane using the electric field with 0.0% octopole and -4.0% dodecapole components. Both forward (a) and reverse scan modes (b) are shown. Figure from “Effects of higher-order multipoles on the performance of a two-plate quadrupole ion trap mass analyzer,” <i>Int. J. Mass Spectrom.</i> , 299, pp 151-157, 2011.....	103
Figure 5-15: Mass spectra of (a) heptane, (b) toluene and (c) trichloroethylene using 2.14% octopole and 10.49% dodecapole components. Other conditions: (a) ionization time: 10 ms, scan speed: 330 Th/s, ac frequency: 345 kHz, scan mode: forward scan; (b) ionization time: 10 ms, scan speed: 110 Th/s, ac frequency: 340 kHz; scan mode: forward scan; and (c): ionization time: 4 ms, scan speed: 110 Th/s, ac frequency: 340 kHz, scan mode: reverse scan, and ac amplitude (1.4 V_{0-p}) is same for all cases. Figure from “Effects of higher-order multipoles on the performance of a two-plate quadrupole ion trap mass analyzer,” <i>Int. J. Mass Spectrom.</i> , 299, pp 151-157, 2011.....	104
Figure 5-16: The two trapping regions of the coaxial trap. Figure from "Coaxial Ion Trap Mass Spectrometer: Concentric Toroidal and Quadrupolar Trapping Regions," <i>Anal. Chem.</i> , 83, pp. 5578-5584, 2011.....	105
Figure 5-17: Experimental set-up for coaxial ion trap. Figure from "Coaxial Ion Trap Mass Spectrometer: Concentric Toroidal and Quadrupolar Trapping Regions," <i>Anal. Chem.</i> , 83, pp. 5578-5584, 2011.....	106
Figure 5-18: The various phases of the mass analysis performed with the coaxial trap. Figure from "Coaxial Ion Trap Mass Spectrometer: Concentric Toroidal and Quadrupolar Trapping Regions," <i>Anal. Chem.</i> , 83, pp. 5578-5584, 2011.....	107
Figure 5-19: Control signal timing for (a) a single toroidal transfer experiment and (b) multiple toroidal transfer experiments. Figure from "Coaxial Ion Trap Mass Spectrometer: Concentric Toroidal and Quadrupolar Trapping Regions," <i>Anal. Chem.</i> , 83, pp. 5578-5584, 2011.....	108
Figure 5-20: The fields and potentials of the coaxial ion trap. (a) Equipotential contour plot, (b) Axial Potential and Field, designed to approximate the Paul trap, (c) Radial Potential and Field, designed to approximate the toroidal trap. Figure from "Coaxial Ion Trap Mass Spectrometer: Concentric Toroidal and Quadrupolar Trapping Regions," <i>Anal. Chem.</i> , 83, pp. 5578-5584, 2011.....	110
Figure 5-21: Coaxial ion trap mass spectrum of bromopentafluorobenzene: (a) data acquired during entire experiment (b) mass spectrum for the first quadrupole scan, (c) mass spectrum for the third quadrupole scan (after the first toroidal transfer). Figure from "Coaxial Ion Trap Mass Spectrometer: Concentric Toroidal and Quadrupolar Trapping Regions," <i>Anal. Chem.</i> , 83, pp. 5578-5584, 2011.....	111

Figure 6-1: Schematic view of the PLIT plate design. Figure from “A Lithographically Patterned Discrete Planar Electrode Linear Ion Trap Mass Spectrometer,” <i>J. Microelectromech. Sys.</i> , (in press).....	114
Figure 6-2: The electrode arrangement and stored ions in a planar electrode PLIT.....	116
Figure 6-3: (top) Electropotential contour plots of the PLIT at $z = 0$, or the center of the slit. (middle) Electropotential contour plots of the PLIT at $y = 0$, or halfway between the plates. (bottom) SIMION simulation of ejected ion trajectory.....	116
Figure 6-4: The potential created in the trapping region (between the plates) by each line pair with 1000 V applied to a single line pair and independent of other pairs. The plate surfaces are represented by dashed vertical lines. Area on the graph not between these lines is the potential seen as particles travel through the ejection slit. Figure from “A Lithographically Patterned Discrete Planar Electrode Linear Ion Trap Mass Spectrometer,” <i>J. Microelectromech. Sys.</i> , (in press).....	118
Figure 6-5: A trapping potential used when adding weighted individual line pair functions.....	120
Figure 6-6: A field with higher order components of 0.803% octopole and -2.676% dodecapole. (a) The electric field of the PLIT compared to an ideal field. (b) The difference between the ideal field and the calculated field. (c) A zoomed in view of plot (b).....	121
Figure 6-7: A field with higher order components of 2.14% octopole and -2.58% dodecapole. (a) The electric field of the PLIT compared to an ideal field. (b) The difference between the ideal field and the calculated field. (c) A zoomed in view of plot (b).....	122
Figure 6-8: (left) Trapping side of the PLIT. (right) Voltage connection side of the PLIT.	123
Figure 6-9: Actual plate/PCB assembly. (left) Top PCB removed. (right) Complete plate/PCB assembly. Figure from “A Lithographically Patterned Discrete Planar Electrode Linear Ion Trap Mass Spectrometer,” <i>J. Microelectromech. Sys.</i> , (in press).....	124
Figure 6-10: (left) The ion trap assembly secured together with electron gun. (right) Trap assembly mounted to a vacuum flange in its completed operational form.	124
Figure 6-11: Diagram of trap inputs and outputs.....	126
Figure 6-12: Lab bench for the PLIT setup.	126
Figure 6-13: A diagram showing the timing of various control signals of the LIT system. (top) Frequency sweep scan. (bottom) Linear amplitude ramp. Figure from “A Lithographically Patterned Discrete Planar Electrode Linear Ion Trap Mass Spectrometer,” <i>J. Microelectromech. Sys.</i> , (in press).....	128

Figure 6-14: A comparison between two identical mass analysis experiments but with different sample pressure. (top) 5×10^{-5} torr sample pressure, (bottom) 1×10^{-5} torr sample pressure.	128
Figure 6-15: Frequency sweep with 0.803% octopole and -2.676% dodecapole. Isobutylbenzene mass analysis data. (top) Raw mass scan data over the 100 ms scan. (bottom) Mass scale for the top plot. Figure adapted from "A Lithographically Patterned Discrete Planar Electrode Linear Ion Trap Mass Spectrometer," <i>J. Microelectromech. Sys.</i> , (in press).....	130
Figure 6-16: Frequency sweep with 2.14% octopole and -2.56% dodecapole of (a) dichloromethane, and (b) toluene.	131
Figure 6-17: A frequency sweep scan of dichloromethane at a higher trapping voltage. The three dominant peaks shown are the m/z 84/86/88 peaks.	132
Figure 6-18: (top) Mass spectrum of toluene obtained from the PLIT using a linear RF ramp. (middle) A comparison toluene spectrum from the Thermo Scientific ITQ900. (bottom) Mass spectrum obtained on the PLIT using a linear RF ramp. Figure from "A Lithographically Patterned Discrete Planar Electrode Linear Ion Trap Mass Spectrometer," <i>J. Microelectromech. Sys.</i> , (in press).	134
Figure 6-19: Electric fields shown in electrode surfaces spaced at different distances. Figure from "Novel Ion Traps Using Planar Resistive Electrodes: Implications for Miniaturized Mass Analyzers," <i>J. Am. Soc. Mass Spectrom.</i> , 35, pp. 1435-1441, 2008.....	136
Figure 6-20: Simulated ion trajectories in miniaturized trapping volumes. Figure from "Novel Ion Traps Using Planar Resistive Electrodes: Implications for Miniaturized Mass Analyzers," <i>J. Am. Soc. Mass Spectrom.</i> , 35, pp. 1435-1441, 2008.....	136
Figure 6-21: Mass spectra taken from the miniaturized planar linear ion trap with (top) PFTBA, (middle) bromonaphthalene, and (bottom) toluene.	137
Figure 7-1: (a) The capacitive voltage divider circuit in the ion trap with a varactor used in parallel with standard surface mount capacitors. (b) A commonly used isolating circuit to employ varactors, but isolate them from RF.....	142
Figure 7-2: The five degrees of freedom of plate alignment.	143
Figure 7-3: Five piezoelectric actuators to allow positions for all directions and angles of plate alignment. Figure adapted from "Novel ion traps using planar resistive electrodes: implications for miniaturized mass analyzers," in 6th Workshop of Harsh-Environment Mass Spectrometry, Cocoa Beach, FL, 2007.....	144
Figure 7-4: Possible electrode arrangement that matches the electrode geometry between the RF and DC regions.....	145

Figure 7-5: Electropotential contour plots for the electric trapping fields in linear ion traps. (a) A linear ion trap with electrode geometries matched. (b) A linear ion trap with biased end plates for axial trapping. Figure adapted from "A two-dimensional quadrupole ion trap mass spectrometer," *J. Am. Soc. Mass Spectrom.*, 13, pp. 659-669, 2002. 147

1 INTRODUCTION

1.1 Introduction

Mass spectrometry is the determination of the masses of ions arising from molecules, atoms, and molecular fragments and is an important technique in analytical chemistry. The information that can be gleaned from mass spectrometry experiments consists of the atomic weight of the different molecular components of an analyte, structural characteristics of those molecules, and elemental composition of the base molecules and the fragment ions of a compound. This technique is used in a wide range of applications. Examples of these applications include biology [1], forensics [2, 3], environmental sciences [4], medical research [5], and space exploration [6].

Quadrupole ion traps have been a significant source of progress in the development of mass spectrometer instruments. Quadrupole ion traps utilize a radio frequency (RF) electric field to trap the ionized form of an analyte, and then mass selectively eject those ions into a detector. The specific timing of electric field conditions as they relate to signals at the ion detector indicate the mass-to-charge ratio of each detected ion.

Quadrupole ion trap devices are attractive because of their inherent sensitivity and specificity and because they can be miniaturized and operated at higher pressures relative to other mass analyzer types [7, 8]. These characteristics are particularly important due to the need to make instruments more portable. As instruments become more portable, field research

becomes less difficult due to eliminating the need to constantly send samples back to large laboratories for analysis. In some applications, such as space exploration, it can even be impossible to send samples back to Earth for analysis as many exploration missions currently being undertaken are not designed for return trips. Portable instruments that are also capable of high performance enable analysis of environments that would otherwise remain completely unknown. Portable systems also provide a great benefit in situations where rapid analysis must be performed. One example of this is seen in applications of national defense, where a chemical or biological sample may need to be analyzed quickly and on site to determine proper response procedures and protect lives.

My work on ion traps has focused on designs that included all of the benefits of conventional ion traps, but also increase the ease and precision of the miniaturization process of the trap. This benefit is due to the use of microfabrication techniques to create the electrode structures that form the ion trap. These electrode structures also allow for a study of the electric fields used to trap the ions of the trap. Ion trap theory assumes specific and precise electric fields to accurately predict the behavior of an ion trap. However, real world instruments will have imperfections introduced that will affect ion trap performance and cause deviations from expected behavior. The design of the electrodes used in my research allow for compensation of these imperfections. The electrode pattern yields a degree of flexibility and optimization not present in other traps.

My efforts have been part of the development of four designs of planar electrode ion traps. These designs include traps based on 3-dimensional quadrupole, toroidal, coaxial, and linear trapping geometries. All of these traps have advantages and disadvantages. The simplest trap to work with is a planar Paul trap, a trap that conforms most closely to established ion trap theory,

and is the easiest to optimize. However, the ceiling on the optimized performance is lower than that on other designs. The toroidal trap is a more complex trap, but has an increased ion storage capacity, leading to a more sensitive instrument. The coaxial trap is a hybrid of the planar Paul trap and the coaxial trap, and attempts to combine the strengths of both traps. The linear trap conserves the simplicity of the planar Paul trap, but still has the benefit of increased ion storage capacity.

1.2 Contributions

The research presented in this work is the result of collaboration between the department of Electrical and Computer Engineering under the direction of Dr. Aaron Hawkins, and the department of Chemistry and Biochemistry under the direction of Dr. Daniel Austin. Dr. Stephen Lammert of Torion Technologies also provided useful consultation. My unique contributions to this work include the following:

1. Conceptual and theoretical development of the planar linear ion trap.
2. Simulation of electric fields for the linear ion trap using SIMION. This work with SIMION was also used in the design of the electrode patterns in order to create more effective designs for electric field control. As part of this work I also established conventions used by the entire ion trap group for calculating electric fields for planar electrode ion traps.
3. Electrode layout on the planar Paul, toroidal, coaxial, and linear ion trap designs using CADENCE software for mask design used in the microfabrication processing of electrode surfaces.
4. Development of microfabrication recipes for ion trap electrode surfaces.

5. Microfabrication of the electrode structures used in the Paul, toroidal, coaxial, and linear ion traps.
6. Printed circuit board (PCB) design using EAGLE layout software to be used in conjunction with the ion trap electrode surfaces and partial fabrication of those PCBs for use in the planar Paul, toroidal, coaxial, and linear ion trap devices.
7. Design, assembly, and construction of vacuum chambers for the planar Paul and linear ion traps, along with accompanying mechanical mounts, electronic signal feedthroughs, gauges, and gas inlets.
8. Design of electronics controls on the planar Paul, coaxial, and linear ion traps. This consisted of the planning and design of needed electronics signals for varied types of experiments, procuring the necessary components to generate those signals, and then programming and arranging those multiple components to operate together.
9. Design of experiments to test the planar Paul trap and linear ion trap designs. This included optimization work to find ideal conditions under which to operate the ion trap device.
10. All design, simulation, fabrication, testing, and optimization done with the miniaturized version of the linear ion trap.

To date my work has been included in seven peer-reviewed publications [9-15], and in 23 conference talks [16-38]. My work with ion traps gave me the opportunity to be involved in every phase of the development of an instrument. I was involved in conceptual development, theory, simulation work, component design, process design, microfabrication, assembly, packaging, experimental design, testing, and optimization. In addition to these publications, I was involved in publishing on multiple other projects unrelated to ion traps.

The list of those publications are included in my complete list of publications in Appendix A.

With the toroidal ion trap, my efforts focused on component design and microfabrication. With the planar Paul trap and the coaxial trap, I was involved in all phases except for the theoretical design and simulation work. The linear ion trap represents a design that was based solely on my work in all phases of development.

1.3 Organization

This dissertation describes the operation of ion trap devices, current research efforts on ion traps, and details the development of planar electrode ion traps. Chapter 2 lays out the theory of quadrupole ion trap devices, including how they operate and benchmarks of trap performance. Chapter 3 describes current efforts in ion trap miniaturization and how the planar electrode ion traps build off current research. Chapter 4 describes the history of the development of the design and the microfabrication approaches used to create the planar electrode ion traps. Chapter 5 describes the operation of the planar Paul, toroidal, and coaxial ion traps. Chapter 6 details the linear ion trap. Chapter 7 will summarize significant results of this work and future directions that have opened up as a result of my efforts.

References

- [1] M. Careri and A. Mangia, "Trends in analytical atomic and molecular mass spectrometry in biology and the life sciences," *Anal. Bioanal. Chem.*, vol. 399, no. 8, pp. 2585-2595, 2011.

- [2] O. Curcuruto, F. Guidugli, P. Traldi, A. Sturaro, F. Tagliaro and M. Marigo, "Ion-trap mass spectrometry applications in forensic sciences. I. Identification of morphine and cocaine in hair extracts of drug addicts," *Rapid Commun. Mass Spectrom.*, vol. 6, no. 7, pp. 434-437, 1992.
- [3] R. D. Johnson and S. Botch, "The Screening of Forensic Blood, Urine, and Tissue Specimens for Xenobiotics Usings Ion-Trap Liquid Chromatography-Tandem Mass Spectrometry," *J. Anal. Toxicol.*, vol. 35, no. 2, pp. 65-74, 2011.
- [4] S. Becker, *Inorganic Mass Spectrometry: Principles and Applications*, West Sussex, England: John Wiley and Sons, Ltd., 2007.
- [5] K. Vekey, A. Telekes and A. Vertes, *Medical Applications of Mass Spectrometry*, Amsterdam, Netherlands: Elsevier Science, 2007.
- [6] J. F. Spann, M. M. Abbas, C. C. Venturini and R. H. Comfort, "Electrodynamic Balance for Studies of Cosmic Dust Particles," *Phys. Scr.*, vol. T89, pp. 147-153, 2001.
- [7] D. E. Austin, M. Wang, S. E. Tolley, J. D. Maas, A. R. Hawkins, A. L. Rockwood, H. D. Tolley, E. D. Lee and M. L. Lee, "Halo Ion Trap Mass Spectrometer," *Anal. Chem.*, vol. 79, no. 7, pp. 2927-2932, 2007.
- [8] L. Gao, Q. Song, G. E. Patterson, R. G. Cooks and Z. Ouyang, "Handheld Rectilinear Ion Trap Mass Spectrometer," *Anal. Chem.*, vol. 78, no. 17, pp. 5994-6002, 2006.
- [9] D. E. Austin, Y. Peng, B. J. Hansen, I. W. Miller, A. L. Rockwood, A. R. Hawkins and S. E. Tolley, "Novel Ion Traps Using Planar Resistive Electrodes: Implications for Miniaturized Mass Analyzers," *J. Am. Soc. Mass Spectrom.*, vol. 19, no. 10, pp. 1435-1441, 2008.
- [10] Z. Zhang, Y. Peng, B. J. Hansen, I. W. Miller, M. Wang, M. L. Lee, A. R. Hawkins and D. E. Austin, "Paul Trap Mass Analyzer Consisting of Opposing Microfabricated Electrode Plates," *Anal. Chem.*, vol. 81, no. 13, pp. 5241-5248, 2009.
- [11] D. E. Austin, B. J. Hansen, Y. Peng and Z. Zhang, "Multipole expansion in quadrupolar devices comprised of planar electrode arrays," *Int. J. Mass Spectrom.*, vol. 295, no. 3, pp. 153-158, 2010.
- [12] Z. Zhang, H. Quist, Y. Peng, B. J. Hansen, J. Wang, A. R. Hawkins and D. E. Austin, "Effects of higher-order multipoles on the performance of a two-plate quadrupole ion trap mass analyzer," *Int. J. Mass Spectrom.*, vol. 299, no. 2-3, pp. 151-157, 2011.
- [13] M. Wang, H. E. Quist, B. J. Hansen, Y. Peng, Z. Zhang, A. R. Hawkins and D. E. Austin, "Performance of a Halo Ion Trap Mass Analyzer with Exit Slits for Axial Ejection," *J. Am. Soc. Mass Spectrom.*, vol. 22, no. 2, pp. 369-378, 2011.
- [14] Y. Peng, B. J. Hansen, H. Quist, Z. Zhang, M. Wang, A. R. Hawkins and D. E. Austin, "Coaxial Ion Trap Mass Spectrometer: Concentric Toroidal and Quadrupolar Trapping Regions," *Anal. Chem.*, vol. 83, no. 14, pp. 5578-5584, 2011.

- [15] B. J. Hansen, R. J. Niemi, A. R. Hawkins, S. A. Lammert and D. E. Austin, "A Lithographically Patterned Discrete Planar Electrode Linear Ion Trap Mass Spectrometer," *J. Microelectromech. Syst.*, in press.
- [16] S. Tolley, A. R. Hawkins, D. E. Austin, B. J. Hansen, E. D. Lee and M. L. Lee, "Coaxial Ion Trap Using Concentric Planar Electrode Arrays," in *Pittcon, March 2-6*, New Orleans, LA, 2008.
- [17] D. E. Austin, S. Tolley, M. Wang, Y. Peng, B. Hansen, A. Hawkins, M. Lee and E. Lee, "New Types of Ion Traps Using Planar Electrode Arrays," in *Pittcon, March 2-6*, New Orleans, LA, 2008.
- [18] Y. Peng, I. W. Miller, Z. Zhang, B. Hansen, M. Wang, S. Tolley, M. Lee, A. Hawkins and D. Austin, "Planar Resistive Electrode Ion Traps," in *56th ASMS Conference on Mass Spectrometry & Allied Topics*, Denver, CO, 2008.
- [19] Y. Peng, I. W. Miller, Z. Zhang, B. J. Hansen, M. Wang, S. E. Tolley, M. L. Lee, A. R. Hawkins and D. E. Austin, "Planar Resistive Electrode Ion Traps," in *Annual Meeting of the American Society for Mass Spectrometry*, Denver, Colorado, June 1-5, 2008.
- [20] E. D. Lee, S. E. Tolley, A. R. Hawkins, D. E. Austin, B. J. Hansen, M. L. Lee and D. L. Later, "Planar Electrode Array Ion Traps including a unique Coaxial Geometry," in *56th ASMS Conference on Mass Spectrometry & Allied Topics*, Denver, CO, 2008.
- [21] Y. Peng, I. W. Miller, Z. Zhang, B. J. Hansen, S. E. Tolley, M. L. Lee, A. R. Hawkins and D. E. Austin, "Novel Planar Ion Traps with Resistive Electrodes," in *Joint Northwest & Rocky Mountain Regional Meeting of the American Chemical Society*, Park City, UT, 2008.
- [22] M. Wang, D. E. Austin, S. E. Tolley, B. J. Hansen, A. R. Hawkins and M. Lee, "Design and Performance of a Halo Ion Trap Mass Analyzer," in *Joint Northwest & Rocky Mountain Regional Meeting of the American Chemical Society*, Park City, UT, 2008.
- [23] Y. Peng, Z. Zhang, I. Miller, B. Hansen, S. E. Tolley, M. L. Lee, A. R. Hawkins and D. Austin, "Designing Custom Electric Fields in Resistive Electrode Ion Traps," in *Pittcon*, Chicago, IL, 2009.
- [24] D. E. Austin, Z. Zhang, Y. Peng, B. J. Hansen, M. Wang, M. L. Lee and A. R. Hawkins, "Planar Electrode Ion traps," in *Annual Meeting of the American Society for Mass Spectrometry*, Philadelphia, PA, May 31 - June 2, 2009.
- [25] Z. Zhang, Y. Peng, M. Wang, B. J. Hansen, A. R. Hawkins and D. E. Austin, "Ion Trap Mass Analyzers Made Using Microfabricated Electrode Plates," in *The 18th International Mass Spectrometry Conference*, Bremen, Germany, Aug 30-Sept 4, 2009.
- [26] D. E. Austin, Z. Zhang, Y. Peng, B. Hansen, A. Hawkins and M. Wang, "Progress in Two-plate Ion Trap Mass Analyzers," in *7th Harsh Environment Mass Spectrometry Workshop*, Santa Barbara, CA, Sept 21-24, 2009.

- [27] D. E. Austin, B. J. Hansen and e. al, "Microfabricated Planar Electrode Ion Traps: Combining Accuracy with Simplicity for Miniaturization," in *Pittcon*, Orlando, FL, Feb 28-Mar 4, 2010.
- [28] M. Wang, D. E. Austin, B. J. Hansen, H. E. Quist, A. R. Hawkins, E. D. Lee and M. L. Lee, "Custom Electric Fields in a Halo Ion Trap Mass Analyzer," in *Pittcon*, Orlando, FL, 2010.
- [29] Z. Zhang, Y. Peng, B. J. Hansen, M. Wang, M. L. Lee, A. R. Hawkins and D. E. Austin, "High Mass Resolution and Tandem Capabilities of a Microfabricated Two-Plate Paul Trap Mass Spectrometer," in *Pittcon*, Orlando, FL, 2010.
- [30] Y. Peng, Z. Zhang, B. J. Hansen, M. Wang, M. L. Lee, A. R. Hawkins and D. E. Austin, "Coaxial Ion Trap: Two Superimposed Trapping Regions in One Analyzer," in *Pittcon*, Orlando, FL, 2010.
- [31] D. E. Austin, B. J. Hansen and e. al, "Microfabricated planar ion trap mass spectrometers," in *Pittcon*, Atlanta, GA, Mar 13-17, 2011.
- [32] D. E. Austin, Z. Zhang, B. J. Hansen and Y. Peng, "Planar Quadrupole and Coaxial Ion Trap Mass Analyzers: Effects of Field SHape," in *59th annual conference of the American Society for Mass Spectrometry*, Denver, CO, June 5-9, 2011.
- [33] B. J. Hansen, H. E. Quist, A. R. Hawkins, Z. Zhang, Y. Peng, M. Wang, M. L. Lee and D. E. Austin, "Quadrupole Ion Traps Realized by Planar Microfabricated Electrodes for Compensation of High Order Multipole Effects," in *Pittcon*, Orlando, FL, 2010.
- [34] Z. Zhang, Y. Peng, H. Quist, J. Wang, B. J. Hansen, A. R. Hawkins and D. E. Austin, "Optimization of Multipole Components in a Planar Paul Trap," in *58th ASMS Conference on Mass Spectrometry*, Salt Lake City, UT, 2010.
- [35] D. E. Austin, Y. Peng, Z. Zhang, B. J. Hansen and A. R. Hawkins, "Ion Trap Mass Analyzers Consisting of Lithographically Patterned Plates," in *2011 FACSS Meeting*, Oct 2-6, 2011.
- [36] B. Hansen, H. Quist, B. Barney, A. Hawkins and D. Austin, "A Linear-type Ion Trap Realized with Two Lithographically Patterned Substrates," in *58th ASMS Conference on Mass Spectrometry*, Salt Lake City, UT, 2010.
- [37] D. E. Austin, Z. Zhang, B. J. Hansen, Y. Peng and A. R. Hawkins, "Microfabricated ion trap mass spectrometers for planetary missions: the planar Paul trap and the coaxial ion trap," in *International Workshop on Instrumentation for Planetary Missions*, Greenbelt, MD, Oct 10-12, 2012.
- [38] Y. Peng, Z. Zhang, B. J. Hansen, M. Wang, M. Lee, A. R. Hawkins and D. E. Austin, "Design and Performance of a Coaxial Ion Trap: Transferring Ions between Two Trapping Regions in One Mass Analyzer," in *58th ASMS Conference on Mass Spectrometry*, Salt Lake City, UT, 2010.

2 ION TRAP THEORY

2.1 Ion Trap Theory

The ion trap is a class of device that uses radio frequency (RF) electric fields in order to form a trapping region with which to store ions. When using the device as a mass spectrometer, this device can mass-selectively eject ionized molecules from the trapping region to a detector. The detector will indicate when groups of ions of a specific mass reach the detector as peaks in signal intensity. The relative timing of these peaks can be used to characterize and identify a compound by comparing the observed peaks with established mass spectra from a database such as those from the National Institute of Standards and Technology (NIST). Currently, commercial ion traps are characterized by their small size, relatively low cost, high sensitivity, and ability to perform tandem mass spectrometry, a type of mass analysis that explores additional fragmentation of base molecules [1, 2].

In order to understand how ions are both stored in and ejected out of a trap, an understanding of ion motion within the trap is required. The quadrupole potential ϕ in an ion trap is defined mathematically as having the form

$$\phi = \frac{\phi_0}{r_0^2}(\lambda x^2 + \sigma y^2 + \gamma z^2), \quad (2.1)$$

where ϕ_0 is the magnitude of the RF potential that is applied on the electrode surfaces that form the trapping field, r_0 is the radius of the trapping, and λ , σ , and γ are constants. In an ion trap, a

positive RF potential is placed on one axis, and a negative potential on a perpendicular axis. The shape of this field is shown in Figure 2-1. The parameter ϕ_0 in Equation 1 has a time varying component. The four poles in Figure 2-1 oscillate at the same frequency, but with poles along different axes oscillating in opposite phase of each other. This oscillation and field shape forms an effective trap for charged particles.

A quadrupole trapping field is established when a potential is placed onto four facing hyperbolic electrodes. Electrodes on one axis of symmetry are given an RF potential, while electrodes along the other axis of symmetry are given the same RF potential, but in opposite phase. Figure 2-2 demonstrates a cross-sectional view of this arrangement of the electrode surfaces. A contour plot of the electric field in the ion storage region is seen in Figure 2-2. The four mathematical poles of the field are located at the hyperbolic electrode surfaces.

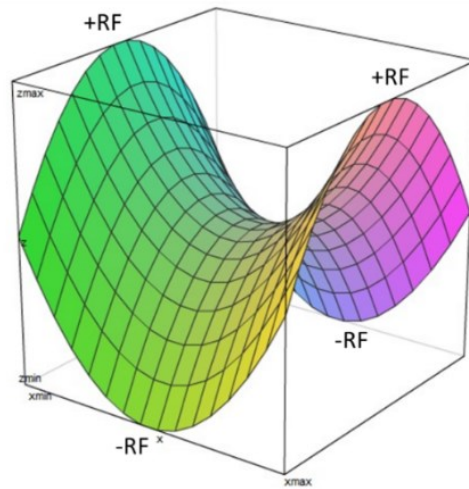


Figure 2-1: A representation of the quadrupole field.

The shape of this electric field forms the basis in understanding ion motion within the trap. Ions remain trapped in the field because the four poles of the field oscillate together. This field is effective because the further ions travel from the middle of the ion storage region, the stronger

a restorative force pushes them back to the middle of the ion storage region. The frequency and the amplitude of this oscillation is largely what determines whether or not an ion is trapped or ejected.

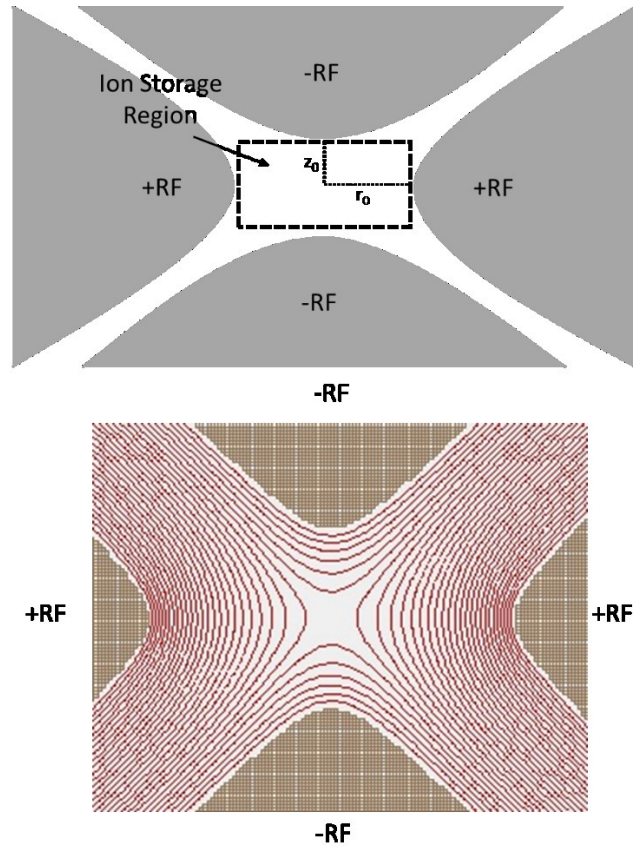


Figure 2-2: (top) (bottom) Hyperbolic electrode arrangement of the quadrupole ion trap. (bottom) Contour plot of the electric field generated between electrodes.

2.2.1 Mathieu Equations

Ion motion in a quadrupole device differs from instruments that use static fields. As a result, specific equations must be used to model ion behavior in a trap. The second-order linear differential equation known as the Mathieu equation [3] was originally developed to model the vibrating motions of materials like the heads of a drum. It has also been found that the Mathieu

equations provide an accurate mathematical description to understand ion motion within a trapping field [4]. The Mathieu equation is

$$\frac{d^2u}{d\xi^2} + (a_u - 2q_u \cos 2\xi) = 0, \quad (2.2)$$

where u represents a directional axis x , y , or z , ξ is a dimensionless parameter equal to $\Omega t/2$, Ω being the frequency of oscillation of the RF potential ($\Omega = 2\pi f$), and a_u and q_u are dimensionless parameters that determine the stability of an ion in a trap. Deriving useful expressions for a_u and q_u is the key to practical understanding of useful ion trap operation.

By substituting the value $\xi = \Omega t/2$ into Equation 2.1, it can be shown that

$$\frac{d^2u}{dt^2} = \frac{\Omega^2}{4} \frac{d^2u}{d\xi^2}. \quad (2.3)$$

By substituting Equation 2.2 into Equation 2.1, multiplying by m , and reorganizing terms, we see that

$$m \frac{d^2u}{dt^2} = \frac{-m\Omega^2}{4} (a_u - 2q_u \cos \Omega t)u. \quad (2.4)$$

The left side of Equation 2.3 can be used to represent the force on an ion as it is comparable to mass time acceleration.

The force in the ion can be independently calculated in all three dimensions to fully represent ion motion in the trap. The force on an ion as a result of electric potential can be described as

$$F_x = -e \frac{d\phi}{dx} = ma = m \frac{d^2x}{dt^2}, \quad (2.5)$$

where e is the charge of an electron, and ϕ is the potential at a spatial point within the trapping field. These same expressions are applicable on the y and on the z axis. The quadrupole potential ϕ , is expressed in Equation 2.1. In electric fields, the Laplace equation must be satisfied, which states

$$\nabla^2 \phi = 0. \quad (2.6)$$

The condition that allows the potential to satisfy the Laplace equation is found as

$$\lambda + \sigma + \gamma = 0. \quad (2.7)$$

In ion traps, $\lambda = \sigma = 1$ and $\gamma = -2$. Placing these values into Equation 2.5 leads to

$$\phi_{x,y,z} = \frac{\phi_0}{r_0^2} (x^2 + y^2 - z^2). \quad (2.8)$$

This equation can be converted to cylindrical coordinates and then simplified using trigonometric identities to obtain

$$\phi_{r,z} = \frac{\phi_0}{r_0^2} (r^2 - 2z^2). \quad (2.9)$$

The magnitude of the RF potential ϕ_0 is a combination of a DC and an AC component and is described as

$$\phi_0 = U + V \cos \Omega t. \quad (2.10)$$

Equation 2.10 is substituted into Equation 2.8, and differentiated with respect to x to obtain

$$\frac{d\phi}{dx} = \frac{2x}{r_0^2} (U + V \cos \Omega t). \quad (2.11)$$

Equation 2.11 can now be substituted into Equation 2.4 to create a useful expression to describe the force on an ion in a trap. This substitution leads to

$$m \frac{d^2x}{dt^2} = \frac{-2e}{r_0^2} (U + V \cos \Omega t) x. \quad (2.12)$$

The right sides of Equation 2.12 and Equation 2.3 can now be compared in order to get values for a_u and q_u in the Mathieu equation, remembering that u represents different axes. This comparison leads to the following equations that will be useful in determining the behavior of ions in a trap:

$$a_x = a_y = \frac{8eU}{mr_0^2\Omega^2}, \quad (2.13)$$

$$q_x = q_y = \frac{-4eV}{mr_0^2\Omega^2}, \quad (2.14)$$

$$a_z = \frac{-8eU}{mr_0^2\Omega^2}, \quad (2.15)$$

$$q_z = \frac{4eV}{mr_0^2\Omega^2}. \quad (2.16)$$

The a and q values are called stability parameters and will be critical to determining the effectiveness of the ion trapping field in retaining ions within the ion trapping region. As these values are partially controlled by the mass of the ion m , these values will also be useful in predicting the mass-selective ejection process from the trap.

2.2.2 Ion Stability Diagram

Solutions to the Mathieu equation will indicate whether or not an ion is stable within the ion trapping region. In order for an ion to remain trapped, its motion must remain bounded in the

r and z directions as indicated in Figure 2-1. If the motion of an ion exceeds this boundary, the ion will collide with and discharge on the electrode surface, or if there is an ejection path, the ion will be ejected out of the trap.

It is generally assumed that to create an ideal quadrupole field, $r_0^2 = 2z_0^2$, where r_0 and z_0 are half the spacing distance between hyperbolic electrodes as seen in Figure 2-2. In practice, this condition is rarely met [4]. When stating the a and q parameters in a more general form with respect to r and z , the parameters become

$$a_r = \frac{8eU}{m(r_0^2 + 2z_0^2)\Omega^2}, \quad (2.17)$$

$$q_r = \frac{-4eV}{m(r_0^2 + 2z_0^2)\Omega^2}, \quad (2.18)$$

$$a_z = \frac{-16eU}{m(r_0^2 + 2z_0^2)\Omega^2}, \quad (2.19)$$

$$q_z = \frac{8eV}{m(r_0^2 + 2z_0^2)\Omega^2}. \quad (2.20)$$

Note, that if $r_0^2 = 2z_0^2$, Equations 2.19 and 2.20 are identical to Equations 2.15 and 2.16. Stable solutions to this equation are shown in Figure 2-3 in both the r and z directions. Shaded areas indicate ion stability within the bounded trapping region. In order to have an ion remain trapped, solutions in both the r and z directions must overlap. Figure 2-4 overlays the plots from Figure 2-3 and shows where these regions overlap. A reading of the diagram shows that there are multiple regions of stability for values of a and q . Most research utilizes the primary region indicated on the figure, as relatively little exploration has been done in the other regions. A closer view of this region is shown in Figure 2-5.

Another important note about Equations 2.17-2.20 is in how masses of ions are mathematically described. These equations include the value $\frac{e}{m}$, or the inverse of the ratio of mass to charge of an ion. In mass spectra plots, mass values are denoted as the ratio of mass to charge, or m/z .

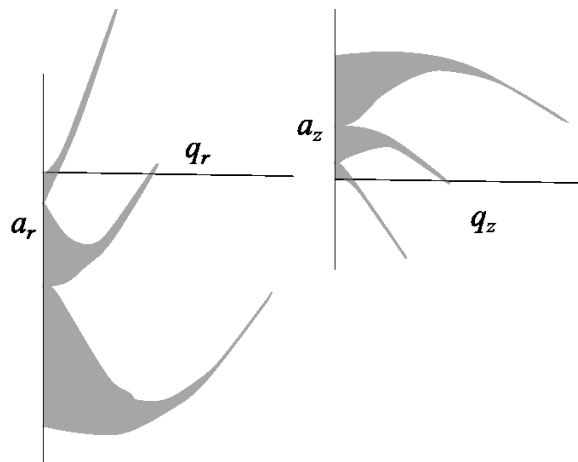


Figure 2-3: Solutions of the Mathieu equation in the r and z directions. Figure adapted from “An Introduction to Quadrupole Ion Trap Mass Spectrometry,” *J. Mass Spectrom.* 32, pp. 351-369, 1997.

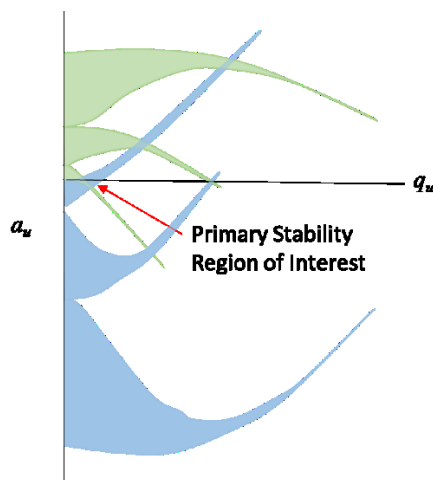


Figure 2-4: Overlapping of the r and z stability regions, with the primarily used stability region indicated. Figure adapted from “An Introduction to Quadrupole Ion Trap Mass Spectrometry,” *J. Mass Spectrom.* 32, pp. 351-369, 1997.

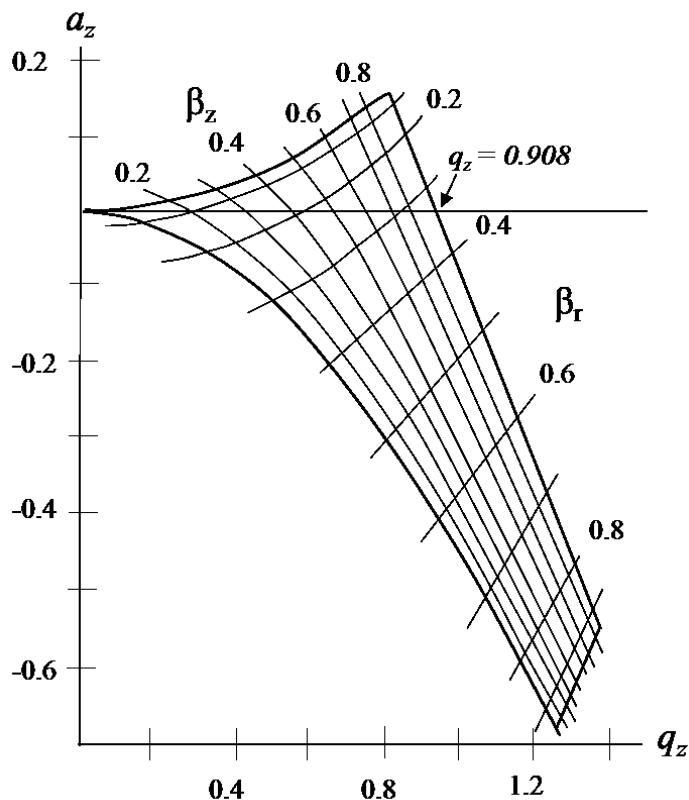


Figure 2-5: The ion stability diagram of the quadrupole ion trap. Figure adapted from “An Introduction to Quadrupole Ion Trap Mass Spectrometry,” *J. Mass Spectrom.* 32, pp. 351-369, 1997.

The value β from Figure 2-5 is used to describe an additional component of ion motion, secular frequency, which will be discussed later.

Analysis of this diagram and comparing with Equations 2.17-2.20 allow for prediction of ion behavior in a trap. In trap operation, it is customary to have zero or nearly zero values for the a_z term by setting the value of U , the DC component of the voltage on the electrodes, to zero. This means that in order to mass-selectively eject ions, the value of q_z is manipulated to eject single groups of molecules at a time. The value of q_z is generally modified by adjusting the value V , or the magnitude of the RF potential placed on the electrode surfaces. Note that the value of q_z is inversely proportional to the value m , or the mass of a trapped ion. This shows that

heavier ions will tend to the left side of the stability diagram, while lighter ions will tend more to the right side. By increasing the magnitude of the RF potential, ions can be mass-selectively made to be unstable within the defined trapping region and ejected out of the trap.

2.2.3 Secular Frequencies

As mentioned previously, there is an additional component of ion motion, β , which must be considered to have a proper understanding of ion trap operation. This term refers to a component of the ion motion in the trap known as its secular frequency. A trapped ion will have a secular frequency, ω , which will be made up of r and z components. The fundamental secular frequencies are termed as $\omega_{r,0}$ and $\omega_{z,0}$, which is defined by the equation

$$\omega_{u,n} = \left(n + \frac{1}{2}\beta_u \right) \Omega, \quad 0 \leq n \leq \infty, \quad (2.21)$$

where for $q_r < 0.2$ and $q_z < 0.4$,

$$\beta_u \approx \sqrt{\left(a_u + \frac{q_u^2}{2} \right)}. \quad (2.22)$$

The β term in Equation 2.22 corresponds to the β lines on the ion stability diagram on Figure 2-5. At higher values of q , the higher values of frequency components in Equation 2.21 become more important and the approximation of Equation 2.22 is less useful.

As already discussed, one method of mass selective ejection from an ion trap is by raising the value of the RF potential to the point of reaching a q_z value located on the boundary of the stability diagram. An alternate means for ion ejection, and often more effective for purposes of mass spectrometry, is to utilize the secular frequencies and the β values of ions within the trap to resonantly excite ions out of the trap [5]. This is done by introducing an additional AC

component to one of the electrode surfaces to resonantly excite ions along a specific axis. The end result of this signal is that as q_z is manipulated to eject ions, instead of requiring ions to reach the boundary of the stability diagram, the point of ion ejection can be made to be a point along the q_z axis which corresponds to a specific secular frequency and β value. This idea is illustrated in Figure 2-6.

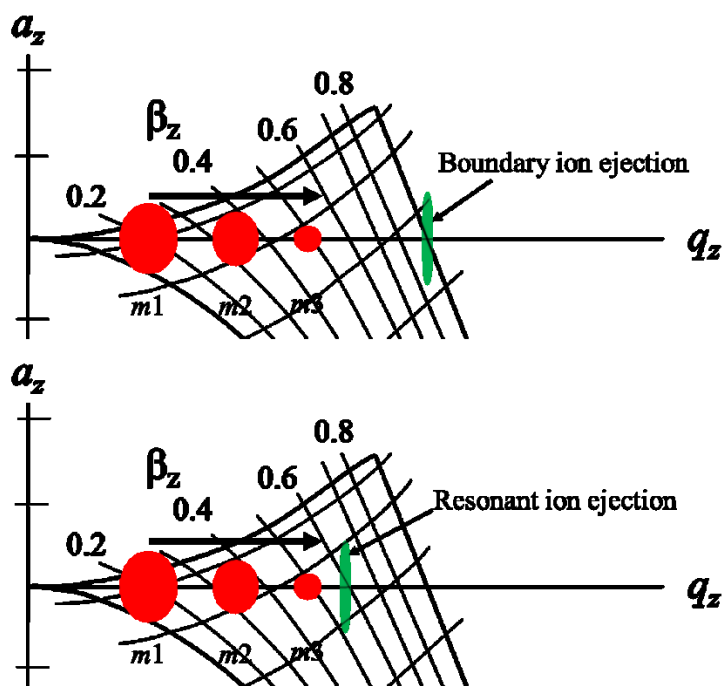


Figure 2-6: Various ion masses m are depicted on a stability diagram. (top) A representation of ion ejection using the boundary of the stability diagram. (bottom) A representation of ion ejection by resonant excitation at secular frequencies.

Resonant excitation of ions provides several possibilities for additional mass analysis experiments. Some additional experiments made possible by manipulating secular frequencies are the following:

1. Resonant excitation can be used to remove unwanted masses of ions, but leave a desired narrow range of ion masses.

2. Resonance can also be used to spur several different internal ion-molecule reactions, which can provide additional information on molecular structure.
3. Resonance can be used to internally excite specific ions, causing them to break apart and dissociate.
4. Introduce kinetic energy to ions to push them close to an electrode, where an image current may be detected allowing for non-destructive measurement, or repeated measurement on a single group of ions.
5. Resonant ejection of ions from a trap into a detector by way of a frequency sweeping AC signal with constant RF amplitude.
6. Resonant ejection of ions from a trap with ramping RF amplitude.

2.2.4 Potential Well Depth

The Mathieu equations and the resulting stability diagrams are a key part of the foundation of understanding ion trap operation, but another factor to consider is called the potential well depth. The potential well depth is essentially the depth of the saddle field shown in Figure 2-2. The Mathieu equations when describing ion motion assumes that there will be enough force on an ion within the field to turn it around and send it back towards the middle of the trap. However, this assumption does not always hold true. It is possible for an ion to be inside the stability diagram mathematically, but the voltage in the trap is just too low to overcome the ion's kinetic energy and push the ion back towards the middle of the trap. A physical analogy could be made to dropping a marble in a bowl and shaking the bowl back and forth, and comparing that to placing a marble on a plate of identical diameter, shaking the plate back and forth, and comparing the effective "trapping" of the marble on the bowl and on the plate. For $q_u < 0.4$, the potential well may be expressed as

$$D_u = \frac{mz_0^2\Omega^2}{16e} q_z^2. \quad (2.23)$$

When $r_0^2 = 2z_0^2$, such as in the standard ideal quadrupole device, the potential well-depth may be approximated by

$$D_z \approx q_z \frac{V}{8}. \quad (2.24)$$

The depth of the potential well helps give an estimation of the total storage capacity of a trap. The number of ions in a trap affects both the sensitivity of an instrument as a mass spectrometer, and the overall effect of space charge within a trap. The potential well model helps to offer a picture on the effect of space charge within a trap. Space charge is the effect that trapped ions have on the potential function. If space charge becomes sufficiently large, it effectively adds a DC component to the trapping field, which consequently begins to change the value of the a term on the stability diagram. This, in turn, effectively displaces the boundary of the stability diagram and the secular frequencies of the stored ions. The maximum ion density is calculated as

$$N_{max} = \frac{3}{\pi} \frac{V^2}{e^2} q_z^2. \quad (2.25)$$

2.2.5 Higher Order Field Effects

The derivations of the Mathieu equation assume that the potential function represented by Equation 2.9 is a purely quadratic function. In actual systems, imperfections are introduced that cause deviations from this assumption. For example, to create a purely quadratic field, electrode surfaces would have to be infinitely long. Other sources of these deviations is due to factors such as small misalignments of the four hyperbolic electrode surfaces and holes that are

intentionally placed into the electrodes for purposes of ion injection or ejection. To fully describe the potential function $\phi_{r,z}$, higher ordered variables are required.

The solution of the Laplace equation for the potential function of an axially symmetric quadrupole ion trap in spherical coordinates has the general form

$$\phi(\rho, \theta, \varphi) = \phi_0 \sum_{n=0}^{\infty} A_n \frac{\rho^n}{r_0^n} P_n(\cos\theta), \quad (2.26)$$

where A_n are weighting coefficients and $P_n(\cos\theta)$ is a Legendre polynomial. Converting to cylindrical coordinates, the full potential function now takes the form

$$\begin{aligned} \phi_{r,z} = \phi_0 [A_0 + A_1 z + A_2 \left(\frac{r^2 - 2z^2}{2r_0^2} \right) + A_3 z \left(\frac{3r^2 z - 2z^3}{2r_0^3} \right) + \\ A_4 \left(\frac{3r^4 - 24r^2 z^2 + 8z^4}{8r_0^4} \right) \dots]. \end{aligned} \quad (2.27)$$

The A_n coefficients where $n = 0, 1, 2, 3,$ and $4,$ respectively, correspond to the monopole, dipole, quadrupole, hexapole, and octopole components of the potential function. In a pure quadrupole field, all coefficients are 0 except for the monopole and the quadrupole components. The monopole component is not significant in ion trap mass spectrometer applications. Coefficients of odd ordered n values are generally negligible in traps with symmetric electrode arrangements, even in real world systems. However, the even ordered coefficients play a large role in ion trap performance. Proper design of the electric potential must account for the higher ordered terms to achieve optimized ion trap performance.

It is worth noting that for optimized performance, it is often not desirable to minimize the higher order field effects as much as may be possible. It has been found that traps yield superior performance when deliberate amounts of octopole are added to the potential function. However,

the amount of higher order component can vary between different types of ion trap systems. There is still much study that needs to be done to fully understand this phenomenon.

2.2 Benchmarks of Ion Trap Performance

When evaluating ion trap performance, there are certain criteria that generally are used. These criteria generally are defined by how effective the instrument traps ions, the ion ejection efficiency, and how effective the instrument is at providing a complete mass spectrum of a compound. There are some specific calculations that can be made in order to quantify this performance.

2.2.1 Mass Resolution

One of the strongest measurements of spectrometer performance is in the degree of resolution of the masses that are visible from an instrument. The resolution of a peak is defined as the ratio of mass to peak width, or $\frac{m}{\Delta m}$. This generally leads to a measurement of higher resolution for peaks of larger m/z values, so it is often necessary to report values for Δm in addition to resolution.

2.2.2 Signal to Noise Ratio

One of the advantages of ion traps is in their inherent sensitivity as mass spectrometers. The sensitivity of ion traps means that they are able to record mass spectra with a relatively small amount of analyte. The signal to noise ratio of the signal recorded from a mass spectrometer is critical in determining if relatively sparse m/z values of ions will be visible from the detector.

2.2.3 Mass Range

A mass spectrometer system is capable of ejecting ions over a range of m/z values. The range of the system is related to the q and a parameters of the stability diagram. These

parameters are dictated by the size of the trap, the frequency of the RF trapping field, and the magnitude of the RF potential. The mass range of a mass spectrometer is generally determined by the limits of the available RF power supply.

2.3 Ion Trap Development

Ion traps have been developed considerably since they were originally invented. The development of ion traps has pressed forward various objectives. These objectives include easier fabrication, higher performance, increased portability, and increased ion storage capacity.

2.3.1 Early Ion Trap History

The ion trap was originally invented in 1953 by Wolfgang Paul [6]. As part of this work, Paul won the 1989 Nobel Prize in Physics along with Hans Dehmelt and Norman Ramsey. Figure 2-7 shows the original Paul ion trap. At first, ion traps were used in conjunction with quadrupole mass filters or drift cells [7]. The ion trap served as an ion source for these devices. The quadrupole ion trap was also used as a storage device for ions to be studied in ion/molecule reactions [8-10] and as a low-pressure chemical ionization source [11-14]. Todd and March gave a review of the development of ion traps prior to their commercial development [15].



Figure 2-7: The original ion trap developed by Wolfgang Paul.
Figure from <http://bigs.physics-astro.uni-bonn.de/index.php?id=76>

In the 1980s, the potential of the ion trap as a mass spectrometer became apparent and has since assumed a prominent role in the development of mass spectrometry. Following the demonstration of the ion trap as a mass analyzer [12, 16], the first key to this prominent role came in the discovery that ions in a trap could be made to be mass-selectively unstable [17]. In addition to mass-selective instability in the trap, it was found that molecular ions could be fragmented to acquire more comprehensive mass spectra [18]. Also important in the development of ion traps as mass spectrometers was the beginning of the use of helium in ion traps as a background gas that would serve to cool ions down kinetically within the trap. The use of helium made the ion trap a viable mass spectrometer by improving mass resolution and trapping capacity of the device. After these discoveries, came the development of the first commercial ion trap mass spectrometer by Finnigan MAT. Finnigan developed the idea of breaking the constraints of $r_0^2 = 2z_0^2$ by creating a “stretched” ion trap. This stretching of the trap in the z direction led to the discovery that carefully-selected higher order multipoles could have a positive impact on the performance of an ion trap.

2.3.2 Mass Filters

The mass filter consists of four circular rods arranged in a manner similar to the hyperbolic electrodes of the quadrupole ion trap. The use of circular rods was found to be an acceptable shape of electrode for this application, but is simpler to make than a hyperbolic electrode. The reason circular rods are acceptable is because mass filters can work effectively even with significant deviations from a purely quadratic potential function. A mass filter works by applying a field that only allows specific masses to stably pass through the rods. Figure 2-8 demonstrates how a mass filter operates.

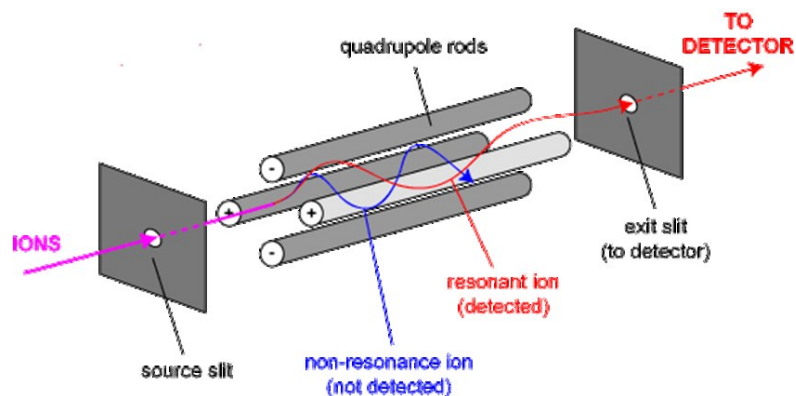


Figure 2-8: A quadrupole mass filter. Diagram from Dr. Paul Gates, University of Bristol (<http://www.bris.ac.uk/nerclsmsf/techniques/gcms.html>)

2.3.3 Cylindrical Traps

The cylindrical ion trap (CIT) was developed as a way to try to create an ion trap with a simpler fabrication process than that of the traditional Paul trap. Like the Paul trap, it was originally used for ion storage [19, 20], and was later developed for use as a mass analyzer. It was first used in a mass-selective stability scan [21], much like a filter, and was later demonstrated using mass-selective instability scans [22]. Instead of three hyperbolic electrodes that require precise machining and alignment, the cylindrical ion trap consists of an electrode arrangement of a cylindrical tube, with two planar end caps on either end of the tube. Because the CIT is much easier to fabricate than the Paul trap, much research work has been directed towards studying the effects of trap size. The CIT has provided fertile ground for studying increasingly miniaturized ion traps [23-29]. These approaches will be detailed later in this work. A cylindrical ion trap, along with the similarities in electric field profiles between the Paul trap and the CIT, is shown in Figure 2-9.

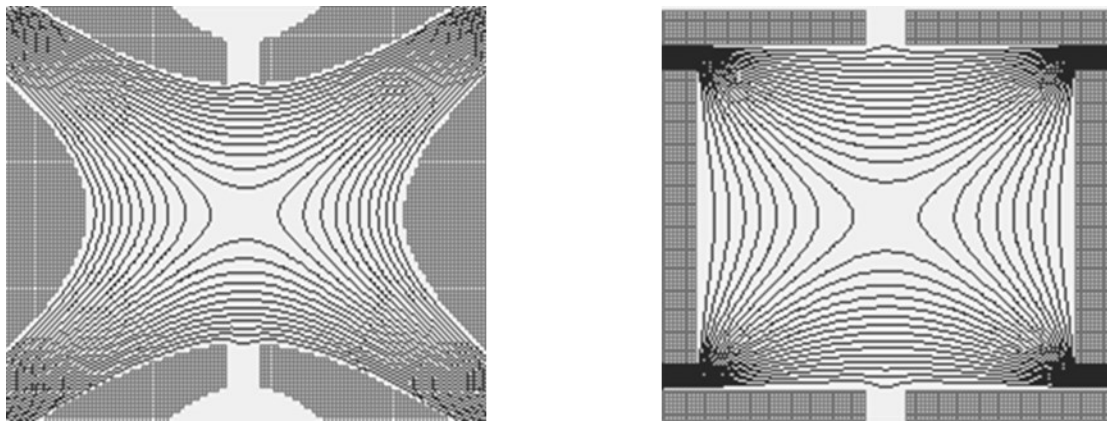
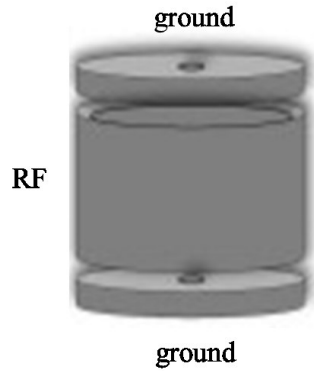


Figure 2-9: (top) A cylindrical ion trap. (bottom) The similarity of electric field profiles between the Paul trap, on the left, and the CIT, on the right.

2.3.4 Toroidal Traps

Toroidal ion traps were created with the goal of increasing ion storage capacity of the Paul trap [30-33]. This trap achieves greater ion storage capacity by altering the shape of the ion storage region. This greater storage capacity was found to be necessary to limit the deleterious effects of ion-ion interaction within a trap (i.e. space charge) [34]. The Paul trap electrode cross-section geometry is rotated about an axis in order to create a toroidal region to store ions. This is illustrated in Figure 2-10. The extent of the ion storage capacity is dictated by the volume of the toroid. However, due to the curved nature of the ion storage region, there can be significant deviations in trap behavior predicted from the standard solutions of the Mathieu equations.

Mathematical solutions for toroidal ion traps are more complex and create a trap that can be more difficult with which to work.

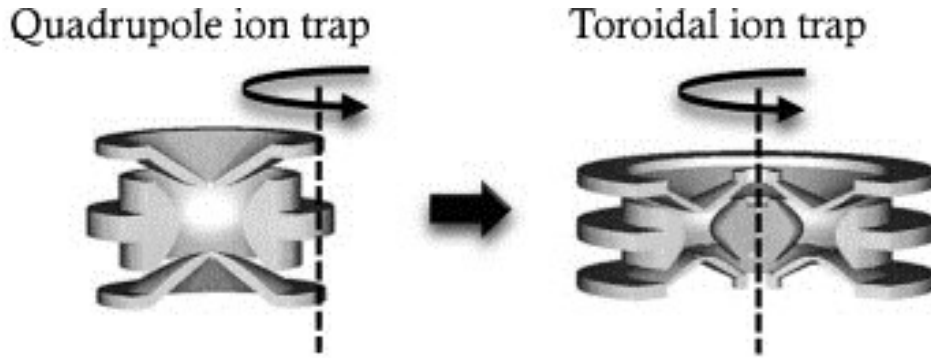


Figure 2-10: The arrangement of electrodes in a toroidal ion trap and their relationship to the Paul trap arrangement. Figure adapted from “Design, optimization and initial performance of a toroidal rf ion trap mass spectrometer,” *Int. J. Mass Spectrom.*, 212, pp. 25-40, 2001.

The electric potential function [35] in an ion trap can be expressed in spherical coordinates (ρ, θ, φ) as

$$\phi(\rho, \theta, t) = \phi_0(t) \sum_{l=0}^{\infty} A_l \left(\frac{\rho}{r_N}\right)^l P_l(\cos\theta), \quad (2.28)$$

where ϕ_0 is the RF potential applied to the ring electrodes and the endcap electrodes are grounded, r_N is the inner radius of the ring electrode, A_l is the expansion coefficient of the order l , and $P_l(\cos\theta)$ is the Legendre polynomial of order l . As in Equation 2.26, the Paul trap equivalent of Equation 2.28, the A term refers to the orders of pole (i.e. monopole, dipole, quadrupole, hexapole, octopole, etc.).

It is useful to express the potential function in cylindrical coordinates, and can be expressed in a more specific form for quadrupole devices. For a quadrupolar device, or a device

whose potential function is dominated by the A_2 term, the potential function can be expressed [31] as

$$\phi(r, z) = \lambda(r - R)^2 + \mu z^2, \quad (2.29)$$

where R is the radius of the toroidal axis formed by the electrodes, and λ and μ are arbitrary constants. The Laplace equation in cylindrical form solves as

$$\nabla^2 \phi(r, z) = 2\lambda \left(2 - \frac{R}{R+s} \right) + 2\mu = 0, \quad (2.30)$$

where s is defined as $s = r - R$. If $R = 0$, then $\lambda = 1$ and $\mu = -2$, resulting in a Paul trap device. If $R \rightarrow \infty$, then $\lambda = -\mu = 1$, resulting in a 2D linear ion trap. This condition shows that a purely quadrupolar field is impossible to achieve. While many approximations from conventional ion trap theory can be applied to the toroidal device, there are still deviations in behavior from this model that create the increased complexity of working with toroidal ion traps.

2.3.5 Linear Traps

The linear ion trap (LIT) has a potential function that is a two dimensional version of that described by the Paul trap. It is designed to have the relative mathematical simplicity of the Paul trap, but with an increased ion storage capacity [36,37]. The LIT consists of 12 total electrode surfaces, arranged into three groups of four. Each electrode surface is hyperbolic in two dimensions, but linear in the third, creating a hyperbolic shaped rod. All three groups of electrode rods are arranged in a manner similar to the mass filter shown in Figure 2-8. The three groups are then arranged next to each other along the long axis of the rods. The first and third group have a DC potential applied, while the middle group is given the RF trapping potential in a manner similar to the Paul trap configuration shown in Figure 2-1. Figure 2-11 illustrates this

arrangement. This trap increases the volume of the trapping region, much like the toroidal ion trap. The volume of the trapping region in the LIT is a cylindrical region that extends down the long axis of the middle group of electrodes. Because the LIT does not curve the trapping region, it avoids the increased mathematical complexity involved with the toroidal ion trap. One tradeoff, however, is that the LIT requires more physical volume than the toroidal trap in order to achieve the same ion storage capacity.

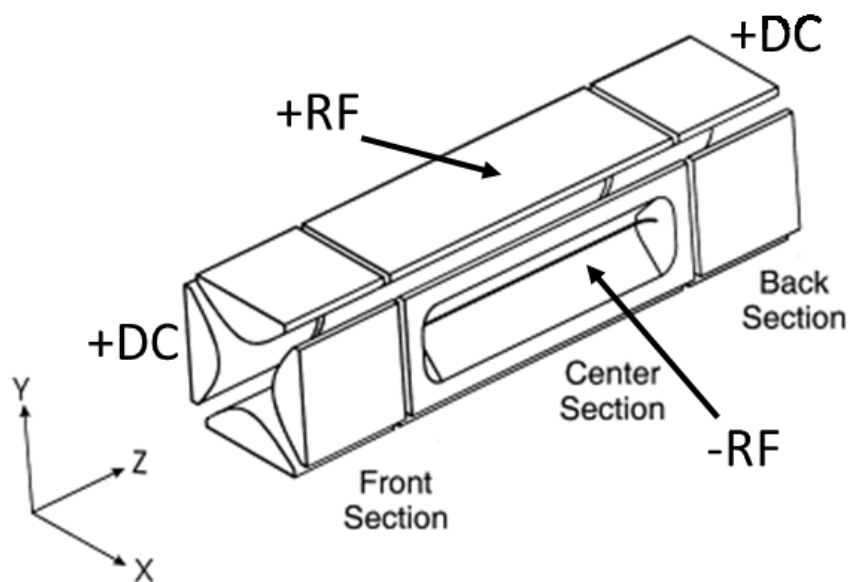


Figure 2-11: A standard linear ion trap. Figure adapted from “A two-dimensional quadrupole ion trap mass spectrometer,” *J. Amer. Soc. Mass Spec.*, 13, pp. 659-669, 2002.

Rectilinear ion traps (RIT) are an attempt to create a device with the advantages of the LIT, but with a simplified electrode geometry [38], much like the CIT but with even greater storage capacity. A further advantage of the RIT and the LIT is that they are able to trap externally injected ions more efficiently than 3D traps [39]. The RIT has found use in applications in areas of ion/molecule reactions [40, 41], analysis of proteins [42], and monitoring

of environments for toxic substances [43]. The RIT is formed by using planar electrodes in the electrode geometry. Figure 2-12, illustrates this arrangement.

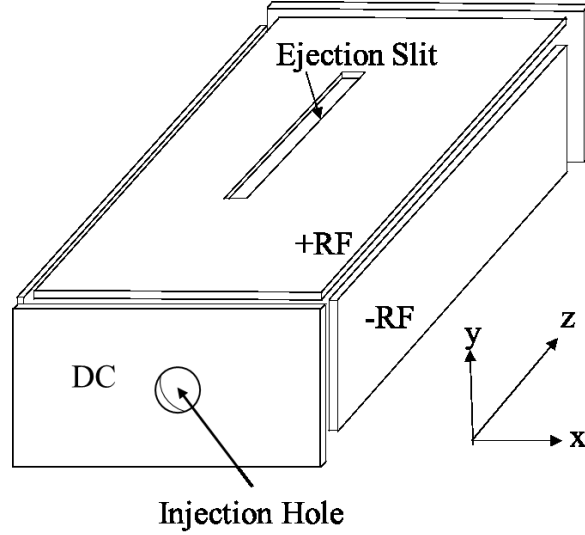


Figure 2-12: The rectilinear ion trap electrode arrangement.

2.4 Linear Ion Trap Specific Theory

The general form of the 2D potential function of the LIT can be expressed [44] as

$$\phi(x, y, t) = \phi_0 \sin(\Omega t) \sum_{N=0}^{\infty} A_N \phi_N, \quad (2.31)$$

where ϕ_0 and Ω are the amplitude and angular frequency of the applied RF respectively, and A_N is the amplitude of the individual multipole component ϕ_N , and ϕ_N is described by 2D Legendre equations. The full potential function can also be expressed as

$$\phi_{x,y} = \phi_0 \left[A_0 + A_1 y + A_2 \left(\frac{x^2 - y^2}{r_0^2} \right) + A_3 \left(\frac{x^3 - 3xy^2}{r_0^3} \right) + A_4 \left(\frac{x^4 - 6x^2y^2 + y^4}{r_0^4} \right) \dots \right] \quad (2.32)$$

where y is the axis of ion ejection, and r_0 is the radius of the trapping field.

The secular frequency for the LIT is described by the same expression as that for the Paul trap and is given by Equation 2.21. When the approximation of Equation 2.22 holds true, the potential ϕ_0 becomes the effective potential on ions in the trap and is given by

$$V_{eff}(r) = D_{x,y} \left(\frac{r}{r_0}\right)^2, \quad (2.33)$$

where the potential well depth $D_{x,y}$ is given by

$$D_{x,y} = \frac{qV_{RF}}{4}. \quad (2.34)$$

Like the Paul trap, for larger values of q , the higher components of secular frequency become more important and Equation 2.33 becomes less useful.

In a pure quadrupole field, ion motion in the x and y directions can be considered separately. The ion trapping parameters a and q closely relate to those of the Paul trap and take the form

$$a_x = -a_y = \frac{8eU}{mr_0^2\Omega^2}, \quad (2.35)$$

$$q_x = -q_y = \frac{4eV}{mr_0^2\Omega^2}. \quad (2.36)$$

The stability diagram for the quadrupole LIT is a similar shape as that for the Paul trap. For higher order multipoles, x and y motion are strongly coupled. Ion secular frequencies and ion stability depend on initial conditions of trapped ions, so when trying to create a stability diagram for higher order multipoles, the result is a stability diagram with diffuse boundaries with no sharp mass cutoff. For low values of applied trapping potential, the ion motion within a trapping field is approximated by an effective mechanical potential [45] as

$$U_{eff}(r) = \frac{N^2 (ze)^2 V^2}{4 m\Omega^2 r_0^2} \left(\frac{r}{r_0}\right)^{2N-2}, \quad (2.37)$$

where N is the order of the multipole and U_{eff} relates to V_{eff} by $U_{eff} = zeV_{eff}(r)$. There are two important conclusions to be drawn from Equation 2.37. First is that the effective potential from a multipole on an ion increases the further the ion is from the center of the trap, corresponding to large values of r . The second is that the higher the order of multipole N , the higher the effective potential seen by the ion. Figure 2-13 illustrates this relationship. This shows that for larger ion motion, or larger values of q on the stability diagram, larger values of multipole increasingly play a role on ion motion.

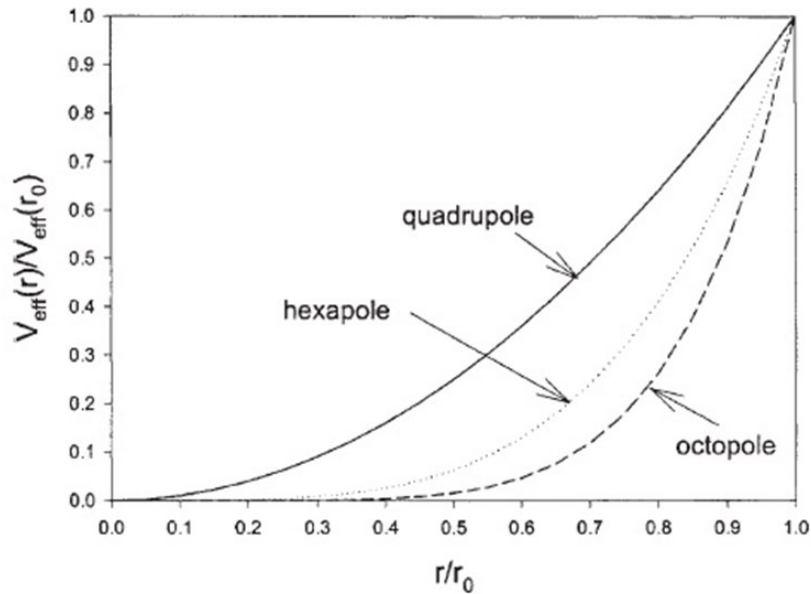


Figure 2-13: Relationship of effective potentials for multipole components of LIT trapping field. Figure from “Linear ion traps in mass spectrometry,” *Mass Spectrom. Rev.*, 24, pp. 1-29, 2005.

References

- [1] C. Henry, "Building a better trap," *Anal. Chem.*, vol. 70, pp. 533A-536A, 1998.
- [2] Z. Ziegler, "Ion Traps come of age - Software control helps these versatile mass spectrometers mature," *Anal. Chem.*, vol. 74, pp. 489a-492a, 2002.
- [3] E. Mathieu, *J. Math. Pure Appl. (J. Liouville)*, vol. 13, pp. 137-203, 1868.
- [4] R. E. March, "An Introduction to Quadrupole Ion Trap Mass Spectrometry," *J. Mass Spec.*, vol. 32, pp. 351-369, 1997.
- [5] J. Williams, K. A. Cos, R. G. Cooks, S. A. McLuckey, K. J. Hart and D. E. Goeringer, "Resonance Ejection Ion Trap Mass Spectrometry and Nonlinear Field Contributions - The Effect of Scan Direction on Mass Resolution," *Anal. Chem.*, vol. 66, pp. 725-729, 1994.
- [6] W. Paul and H. Steinwedel, "A new mass spectrometer without a magnetic field," *Z. Naturforsch. Sect. A*, vol. 8, pp. 448-450, 1953.
- [7] M. Benyazzar, C. S. Creaser and J. W. Stygall, in *Proceedings of the 46th ASMS Conference on Mass Spectrometry and Allied Topics*, Orlando, FL, 1998.
- [8] R. F. Bonner, G. Lawson and J. F. J. Todd, "Ion-molecule reaction studies with a quadrupole ion storage trap," *Int. J. Mass Spectrom. Ion Phys.*, vol. 10, no. 2, pp. 197-203, 1972.
- [9] G. Lawson, R. F. Bonner, R. E. Mather, J. F. J. Todd and R. E. March, "Quadrupole Ion Store (Quistor). Part 1. - Ion-molecule reactions on methane, water, and ammonia," *J. Chem. Soc. Faraday Trans. 1*, vol. 72, no. 0, pp. 545-557, 1976.
- [10] R. F. Bonner, G. Lawson, J. F. J. Todd and R. E. March, *Advances in Mass Spectrometry*, Vol. 6, London: A. R. West ed.; Applied Science, 1974.
- [11] R. F. Bonner, G. Lawson and J. F. J. Todd, "A low-pressure chemical ionisation source: an application of a novel type of ion storage mass spectrometer," *J. Chem. Soc. Chem. Commun.*, pp. 1179-1180, 1972.
- [12] R. E. Mather, G. Lawson, J. F. J. Todd and J. M. B. Bakker, "Quadrupole Ion Storage Trap (Quistor) as a Low-Pressure Chemical Ionization Source for a Magnetic-Sector Mass-Spectrometer," *Int. J. Mass Spectrom.*, vol. 28, pp. 347-364, 1978.
- [13] G. Lawson and J. F. J. Todd, "Weak Peak Enhancement by Selective Ion Trapping in a Quadrupole Ion Storage Source," *Anal. Chem.*, vol. 49, pp. 1619-1622, 1977.
- [14] S. E. Buttrill Jr., B. Shaffer, J. Karnicky and J. T. Arnold, in *Proceedings of the 40th ASMS Conference on Mass Spectrometry and Allied Topics*, Washington DC, May/June 1992.

- [15] J. F. J. Todd and R. E. March, "A retrospective review of the development and application of the quadrupole ion trap prior to the appearance of commercial instruments," *Int. J. Mass Spectrom.*, vol. 191, pp. 9-35, 1999.
- [16] J. E. Fulford, D. N. Hoa, R. J. Hughes, R. E. March, R. F. Bonner and G. J. Wong, "Radio-Frequency Mass Selective Excitation and Resonant Ejection of Ions in a 3-Dimensional Quadrupole Ion Trap," *J. Vac. Sci. Technol.*, vol. 17, pp. 829-835, 1980.
- [17] G. C. Stafford, P. Kelley, J. E. P. Syka, W. E. Reynolds and J. F. J. Todd, "Recent Improvements in and Analytical Applications of Advanced Ion Trap Technology," *Int. J. Mass Spectrom.*, vol. 60, pp. 85-98, 1984.
- [18] J. N. Louris, R. G. Cooks, J. E. P. Syka, P. E. Kelley, G. C. Stafford and J. F. J. Todd, "Instrumentation, Applications, and Energy Deposition in Quadrupole Ion-Trap Tandem Mass Spectrometry," *Anal. Chem.*, vol. 59, pp. 1677-1685, 1987.
- [19] T. L. Grebner and H. J. Neusser, "Laser-Produced Ions Stored in a Cylindrical Ion-Trap and Detected in a Reflectron Time-of-Flight Mass Spectrometer," *Int. J. Mass Spectrom.*, vol. 137, pp. L1-L6, 1994.
- [20] N. Mikami, Y. Miyata, S. S. and T. Sasaki, "Ion Trap Method Combined with 2-Color Laser Spectroscopy of Supersonic Molecular-Beams - Photodissociation of Trapped C₆H₅Cl⁺," *Chem. Phys. Lett.*, vol. 166, pp. 470-474, 1990.
- [21] J. E. Fulford, R. E. March, R. E. Mather, J. F. J. Todd and R. M. Waldren, "The Cylindrical Ion Trap - a Theoretical and Experimental-Study," *Can. J. Spectrosc.*, vol. 25, pp. 85-97, 1980.
- [22] J. M. Wells, E. R. Badman and R. G. Cooks, "A quadrupole ion trap with cylindrical geometry operated in the mass selective instability mode," *Anal. Chem.*, vol. 70, pp. 438-444, 1998.
- [23] M. G. Blain, L. S. Riter, D. Cruz, D. E. Austin, G. X. Wu, W. R. Plass and R. G. Cooks, "Toward the hand-held mass spectrometer: design considerations, simulation, and fabrication of micrometer-scaled cylindrical ion traps," *Int. J. Mass Spectrom.*, vol. 236, pp. 92-104, 2004.
- [24] S. Pau, C. S. Pai, Y. L. Low, J. Moxom, P. T. A. Reilly, W. B. Whitten and J. M. Ramsey, "Microfabricated quadrupole ion trap for mass spectrometer applications," *Phys. Rev. Lett.*, vol. 96, p. 120901, 2006.
- [25] A. Chaudhary, F. H. W. van Amerom, R. T. Short and S. Bhinsali, "Fabrication and testing of miniature cylindrical ion trap mass spectrometer constructed from low temperature co-fired ceramics," *Int. J. Mass Spectrom.*, vol. 251, pp. 32-39, 2006.
- [26] Z. Ouyang, E. R. Badman and R. G. Cooks, "Characterization of a serial array of miniature cylindrical ion trap mass analyzers," *Rapid Commun. Mass Spectrom.*, vol. 13, pp. 2444-2449, 1999.

- [27] E. R. Badman, R. C. Johnson, W. R. Plass and R. G. Cooks, "A miniature cylindrical quadrupole ion trap: Simulation and experiment," *Anal. Chem.*, vol. 70, pp. 4896-4901, 1998.
- [28] O. Kornienko, P. T. A. Reilly, W. B. Whitten and J. M. Ramsey, "Micro ion trap mass spectrometry," *Rapid Commun. Mass Spectrom.*, vol. 13, pp. 50-53, 1999.
- [29] F. H. W. Van Amerom, A. Chaudhary, M. Cardenas, J. Bumgarner and R. T. Short, "Microfabrication of cylindrical ion trap mass spectrometer arrays for handheld chemical analyzers," *Chem. Eng. Commun.*, vol. 195, pp. 98-114, 2008.
- [30] M. E. Bier and J. E. P. Syka, "U.S. Patent No. 5," 1995.
- [31] S. A. Lammert, W. R. Plass, C. V. Thompson and M. B. Wise, "Design, optimization and initial performance of a toroidal rf ion trap mass spectrometer," *Int. J. Mass Spectrom.*, vol. 212, no. 1, pp. 25-40, 2001.
- [32] S. A. Lammert, A. A. Rockwood, M. Wang, M. Lee, E. D. Lee, S. E. Tolley, J. R. Oliphant, J. L. Jones and R. W. Waite, "Miniature toroidal radio frequency ion trap mass analyzer," *J. Am. Soc. Mass Spectrom.*, vol. 17, pp. 916-922, 2007.
- [33] J. A. Contreras, J. A. Murray, S. E. O. J. L. Tolley, H. Tolley, S. A. Lammert, E. Lee, D. Later and M. Lee, "Hand-Portable Gas Chromatograph-Toroidal Ion Trap Mass Spectrometer (GC-TIMS) for Detection of Hazardous Compounds," *J. Am. Soc. Mass Spectrom.*, vol. 19, pp. 1425-14234, 2008.
- [34] J. C. Schwartz, "Do space charge effects limit LC quadrupole ion trap performance?," in *9th Sanibel Conf. Mass Spectrom., Quadrupole Ion Traps*, Sanibel Island, FL, 1997.
- [35] R. E. March and J. F. J. Todd, "Practical Aspects of Ion Trap Mass Spectrometry," in *Vol. I*, Boca Raton, FL, CRC Press, 1995, Chap. 3.
- [36] J. Hager, "A new linear ion trap mass spectrometer," *Rapid Commun. Mass Spectrom.*, vol. 16, pp. 512-526, 2002.
- [37] J. Schwartz, M. Senko and J. Syka, "A two-dimensional quadrupole ion trap mass spectrometer," *J. Am. Soc. Mass Spectrom.*, vol. 13, pp. 659-669, 2002.
- [38] Z. Ouyang, G. Wu, Y. Wong, H. Li, W. Plass and R. Cooks, "Rectilinear ion trap: Concepts, calculations, and analytical performance of a new mass analyzer," *Anal. Chem.*, vol. 76, pp. 4595-4605, 2004.
- [39] S. Quarmby and R. Yost, "Fundamental studies of ion injection and trapping of electrosprayed ions on a quadrupole ion trap," *Int. J. Mass Spectrom.*, vol. 191, pp. 81-102, 1999.
- [40] H. Chen, R. Xu, H. Chen, R. G. Cooks and Z. Ouyang, "Ion/molecule Reactions in a Miniature RIT Mass Spectrometer," *J. Mass Spectrom.*, vol. 40, pp. 1403-1411, 2005.

- [41] C. Zhang, H. Chen, A. J. Guymon, G. Wu, R. G. Cooks and Z. Ouyang, "Instrumentation and Methods for Ion and Reaction Monitoring Using a Non-scanning Rectilinear Ion Trap," *Int. J. Mass Spectrom.*, vol. 255, pp. 1-10, 2006.
- [42] C. Janfelt, N. Talaty, C. Mulligan, A. Keil, Z. Ouyang and R. G. Cooks, "Mass Spectra of Proteins and Other Biomarkers Recorded Using a Handheld Instrument," *Int. J. Mass Spectrom.*, vol. 278, pp. 166-169, 2008.
- [43] A. Keil, H. Hernandez-Soto, R. J. Noll, M. Fico, L. Gao, Z. Ouyang and R. G. Cooks, *Anal. Chem.*, vol. 80, pp. 734-741, 2008.
- [44] D. J. Douglas, A. J. Frank and D. Mao, "Linear ion traps in mass spectrometry," *Mass Spectrom. Rev.*, vol. 24, no. 1, pp. 1-29, 2005.
- [45] D. Gerlich, "Inhomogenous RF fields; A versatile tool for the study of processes with slow ions," in *Advances in chemical physics LXXXII*, New York, John Wiley and Sons, 1992, pp. 1-176.

3 MINIATURIZATION EFFORTS IN ION TRAPS

3.1 Motivations for Miniaturization

A major thrust of mass spectrometer development is not towards peak performance, but rather in the portability of the instrument while still preserving a useful level of performance. All forms of mass analysis involve either having to bring a sample to the mass analyzer, or bringing the analyzer to the sample. In many applications, if the mass analyzer is too large to be portable, this process is either too slow, too difficult, or outright impossible at this time.

Reducing the size of the ion trap is important to achieve portability, but for different reasons than is sometimes expected. The ion trap is a relatively small part of a larger system when acting as a mass analyzer. This system includes power supplies, various signal and pulse generators, vacuum chambers, vacuum pumps, sample and helium injection, ionization sources, and signal output of the trap to some type of user-interface. Since the ion trap itself makes up a relatively small percentage of the overall system size, greater strides in portability are achieved when the various control and support components can be reduced in weight and size. However, the relatively small reductions in size from the trap itself leads to theoretical and practical reasons for being able to achieve greater reduction in real estate in other system components. The end result is a more portable mass analyzer.

3.2 Effects of Trap Miniaturization on System Size and Design

A miniaturized ion trap benefits the overall size of a mass analyzer system. However, there are tradeoffs, additional complexities in both design and fabrication, and practical limitations to miniaturized ion trap performance and in what is feasible to build. We will first discuss the system benefits, and then the challenges of miniaturization.

3.2.1 Benefits of Miniaturization

From Chapter 2, the ion stability diagram is shown in Figure 2-5. The value for q along the ejection axis is the most relevant parameter for determining mass stability within the trap. In 3D traps, this axis is usually the z axis, while in 2D traps, it is usually the y axis. The q parameter in the Paul trap is given by

$$q_u = \frac{e4V}{mr_0^2\Omega^2}. \quad (3.1)$$

The masses of respective ions are expressed in terms of the ratio m/e , or more commonly m/z . V is the amplitude of the RF potential in the trap, r_o is the radius of the trapping region, Ω is the angular frequency of the RF potential. When examining how changing the size of the trapping region affects the trap, it is useful to express Equation 3.1 as a proportion

$$r_0^2 \propto \frac{V}{q_z\Omega^2}. \quad (3.2)$$

Assume that a miniaturized trap is meant to analyze the same mass range as its larger counterpart, or q_u is to be kept relatively constant depending on the m/z value of an ion. Equation 2 demonstrates that the required value of V , or required power varies with the square of the radius of the trapping region. This large decrease in required RF power allows for a reduction in the size and weight of power supplies and batteries. Those two components can

account for as much as half of the overall weight of a mass analyzer system, so any reduction in weight from those components is significant [1].

Another significant factor in mass analyzer system size and weight is from the vacuum pumps. The pump can be one of the heaviest and most power-hungry components within the entire system. By designing a system that allows for relaxing the vacuum requirements, significant progress can be made towards portability [2-6]. For example, while mass analyzers often operate in as high as the low mTorr range, operation in the tens of mTorr range would allow the use of drag pumps instead of turbo pumps [7]. Miniaturizing the volume of the trapping region increases the mean-free path that ions travel without collisions while inside the trap. An increase in the mean-free path increases the possible operating pressure of the trap [6, 8-10]. Another way of increasing the operating pressure of the trap is by increasing the frequency of the RF power supply [11, 12]. The increased frequency allows a higher operating pressure because the RF potential frequency must be high compared to the ion collision frequency to create a longer mean-free path.

3.2.2 Challenges of Miniaturization

As ion traps are miniaturized, there are several complications that arise in instrument behavior. One factor that must be considered is the overall ion storage capacity of an ion trap. As miniaturized ion traps have a smaller trapping volume, they are capable of storing fewer ions. This decrease is due to the effects of space charge effects caused by ion-ion interactions in the reduced trapping volume.

One effort to ameliorate the issues of decreased ion storage volume of miniaturized analyzers utilizes an array of traps to recover the lost capacity. This technique is not without drawbacks. One drawback is in variation in fabrication of the individual traps in the array.

Because of these variations, ion ejection conditions may slightly vary between different traps in the array. Additionally, the path ions travel to the detector during ion ejection can vary between traps, adding to the variation in performance seen across an ion trap array. Ion trap arrays also have increased capacitive reactance, particularly at higher operating frequencies of trapping RF.

Another factor on microfabricated electrodes comes from high-field effects. As electrode patterns are shrunk, there is the possibility of high-field electron emission between electrodes. This effect has been studied and may present problems with microscopic mass analyzers [13].

Gas breakdown is another potential issue with trying to operate mass analyzers at higher pressures. Paschen's Law [14] states that the maximum voltage which can exist between two parallel plates without voltage arcing is approximated by the equation

$$V = \frac{abp}{\ln(pd)+b}, \quad (3.3)$$

where a and b depend on the gas, p is the pressure, and d is the distance between electrodes. Breakdown voltage is high when both pressure and distance is small or when both are large. Intermediate values, which can be seen in the ranges of operation of many miniaturized mass analyzers, will lead to lower breakdown voltages.

Another drawback of miniaturized ion traps is in the fabrication process. In the traditional Paul trap, three hyperbolic electrodes of precise dimensions must also have an extremely precise alignment with respect to each other in order to create the desired electric field. Any small variations in shape or in alignment will add unanticipated higher order multipole components to the trapping field. Electrode designs such as the cylindrical ion trap (CIT) or the rectilinear ion trap (RIT) are designed to compensate for this complexity. However,

as traps get increasingly small, even microscopic imperfections or surface roughness on electrodes become increasingly influential on the potential function [15, 16]. Furthermore, even as microfabrication processes are used to great precision in two dimensions, electrode arrangement is a three dimensional process. There are various techniques being used to address this issue and allow the utilization of microfabrication processes.

3.3 Miniaturization Techniques

The drawbacks and obstacles of miniaturized quadrupole ion trap designs are generally addressed down two paths. The first of these two considerations involve altering the electrode geometry from the traditional Paul trap in such a way to lend itself better to miniaturization while maintaining a similar trapping field profile [17]. The second driving objective in miniaturized designs involves expanding the ion storage capacity that is reduced as trapping dimensions decrease, thus conserving the sensitivity of the instrument. While some approaches to increasing ion storage has involved the use of trap arrays, other approaches have involved altering the electrode geometry to increase the volume of the effective ion storage region [18-20]. Figure 3-1 demonstrates these two branches of development.

3.3.1 Conventionally Machined Devices

The first efforts to shrink trap size were simply scaled down versions of the original Paul trap. This miniaturized Paul trap was constructed using conventional machining techniques. The earlier reported mass analyzers were reported in the 1980's. However, this effort was not focused on portability, but on overall mass range [21, 22]. In these efforts, improvements were eventually limited by the required machining precision in creating the hyperbolically shaped electrodes. At this time, further miniaturization efforts utilized simplified geometries. One of the first variations from the Paul trap design was the CIT [23-27]. Not only has the CIT

provided a simpler electrode pattern to machine and align, but it has also provided an avenue for using microfabrication techniques in the push for portable ion trap systems [28-30]. The linear ion trap (LIT) and the RIT have also been studied in efforts to miniaturize ion trap systems [4, 31-40]. These studies have been conducted both theoretically and experimentally.

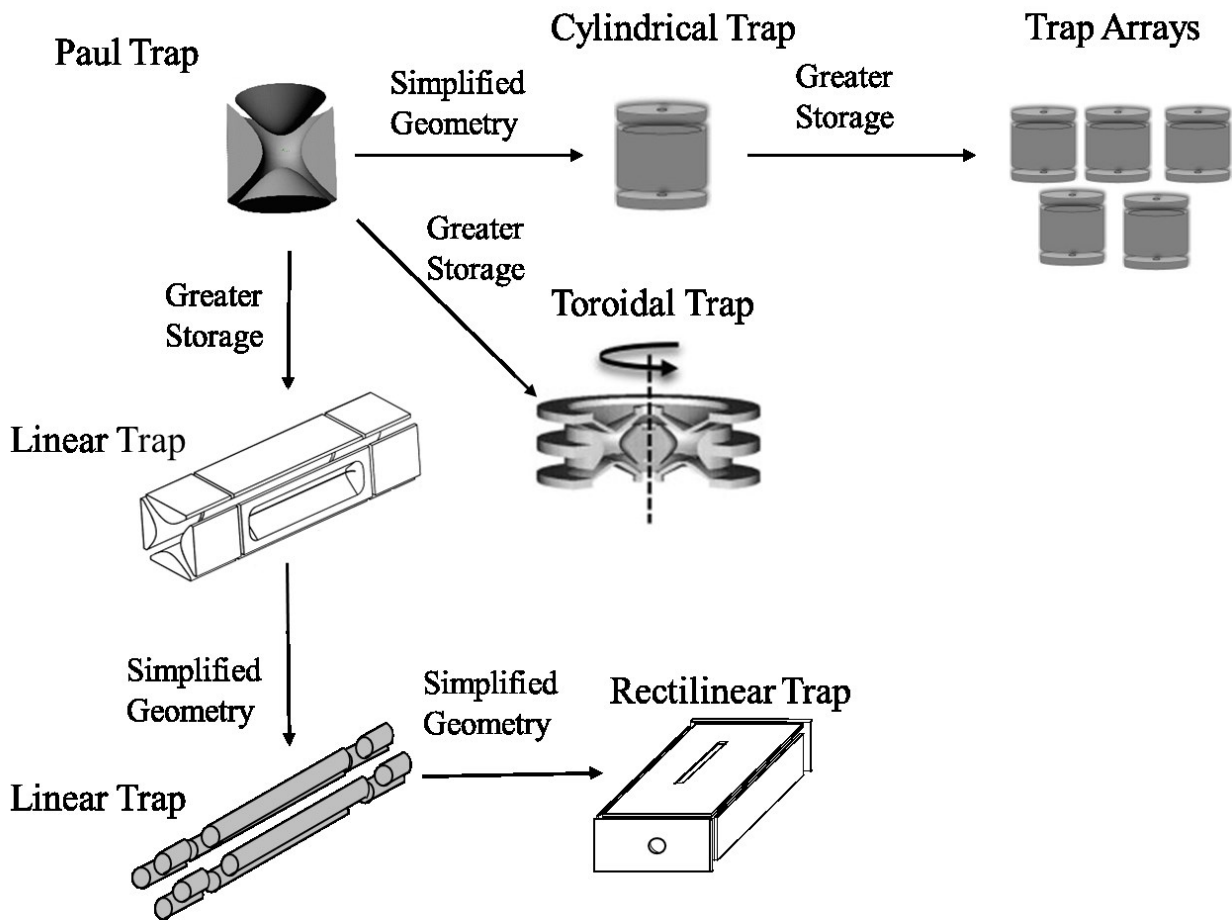


Figure 3-1: Development paths from the original Paul trap that allow for miniaturized traps.

One example of an approach of machined electrode traps is shown below in Figure 3-2, along with the accompanying electrode contour plots of an array of created trapping regions.

This electrode configuration is an array of four side-by-side RITs [41]. This electrode configuration creates multiple traps using shared planar electrode surfaces.

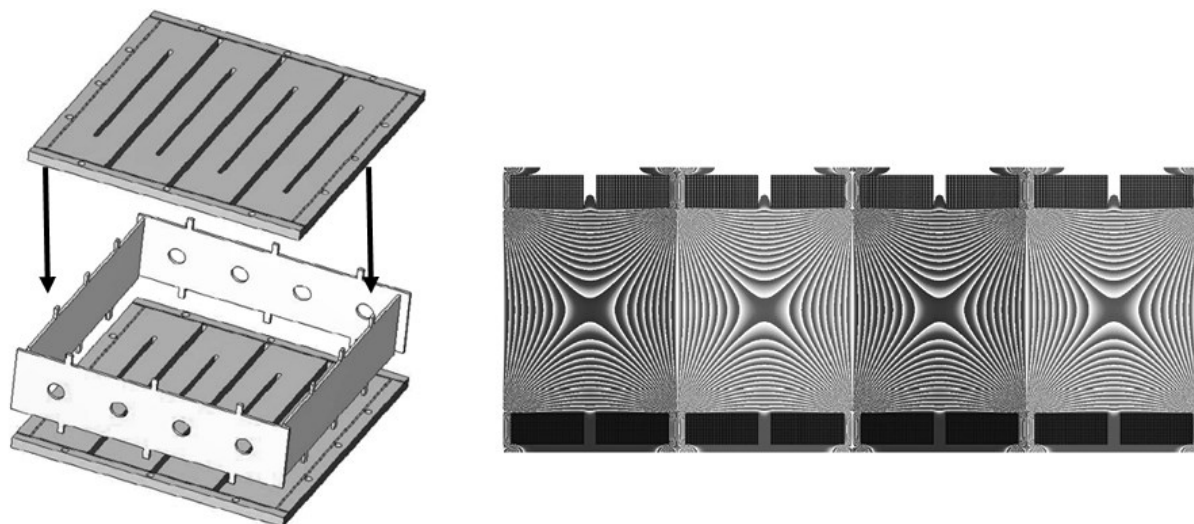


Figure 3-2: (left) An arrayed RIT structure. (right) Electrical field created by the four trapping regions, where each slit in the surface either helps create the electric field profile and provide a path for ion ejection or separates the different trapping regions. Figure from “Ion Trap Array Mass Analyzer: Structure and Performance,” *Anal. Chem.*, 81, pp. 4840-4846, 2009.

3.3.2 Microfabrication Techniques with Quadrupolar Devices

Microfabrication techniques such as etching and photolithography have provided a path in miniaturized trap design that eliminates the need for precision in machining. Microfabrication processes are inherently capable of high precision in their patterning, alignment, and smoothness of features.

3.3.2.1 Mass Filters

MEMS based devices have played a role in the further development of microfabrication techniques to create quadrupolar devices. Some of these efforts were developed around mass filters, a device with similar operating principles and electrode arrangements to that of the LIT. One explored technique has been to use anisotropically-etched grooves in silicon substrates [42-

50]. These grooves provided precise alignment of four machined circular rods, as well as some additional spacer rods. An illustration of this device is shown in Figure 3-3.

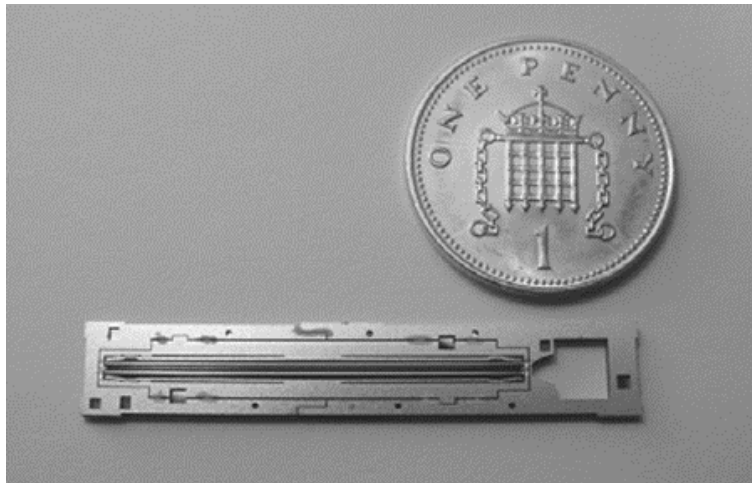
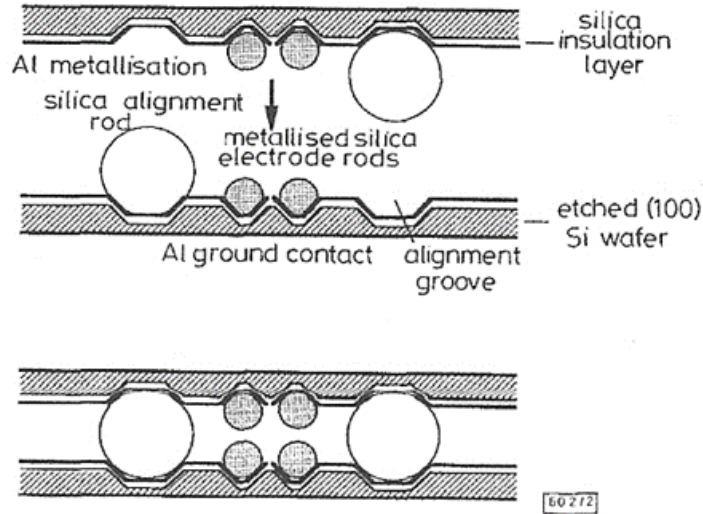


Figure 3-3: A MEMS based approach to a quadrupole device. Figure from “Fabrication of a Microengineered Quadrupole Electrostatic Lens,” *Electron. Lett.*, 32, pp. 2094-2095, 1996.

An alternative to this in-plane placement of rods in the fabrication process is one that has been explored using out-of-plane processes [51,52]. This process involves the placement of standing rods on a substrate. The placement of rods in this process is done using etching techniques similar to the in-plane process. This approach is shown in Figure 3-4.

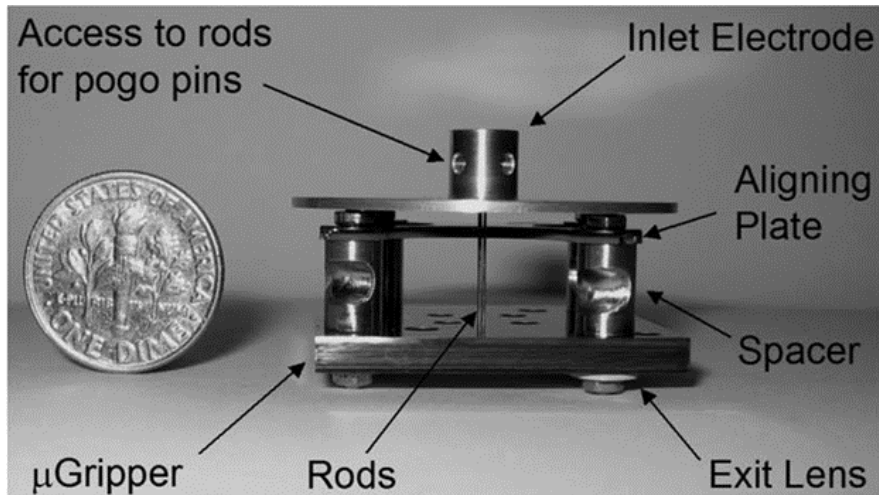


Figure 3-4: The out-of-plane approach to microfabricating a quadrupole mass filter. Figure from “An Application of 3-D MEMS Packaging: Out-of-Plane Quadrupole Mass Filters,” *J. Microelectromechanical Sys.*, 17, pp. 1430-1438, 2008.

3.3.2.2 MEMS Based Traps

The development of the CIT was used in some of the first efforts to develop mass analyzers that took advantage of the benefits of microfabrication. Many early successful results with the goal of reducing the size of a single trap were produced starting in the late 90’s [53-66]. Initial results towards the development of hand-held mass spectrometers have been realized using a version of the CIT [2].

Throughout the development of miniaturized traps, it was noted experimentally that reducing the size of traps also reduced the ion storage capacity of a mass analyzer. In an effort to restore this capacity, arrays of cylindrical ion traps were developed [67-71]. Some arrays of microscopic traps consisted of as many as 1 million separate traps using tungsten layers to form electrodes deposited on silicon [72]. Figure 3-5 is an SEM picture of an array of cylindrical ion traps. The individual traps had a trapping volume of $r_0 = 1 \mu\text{m}$.

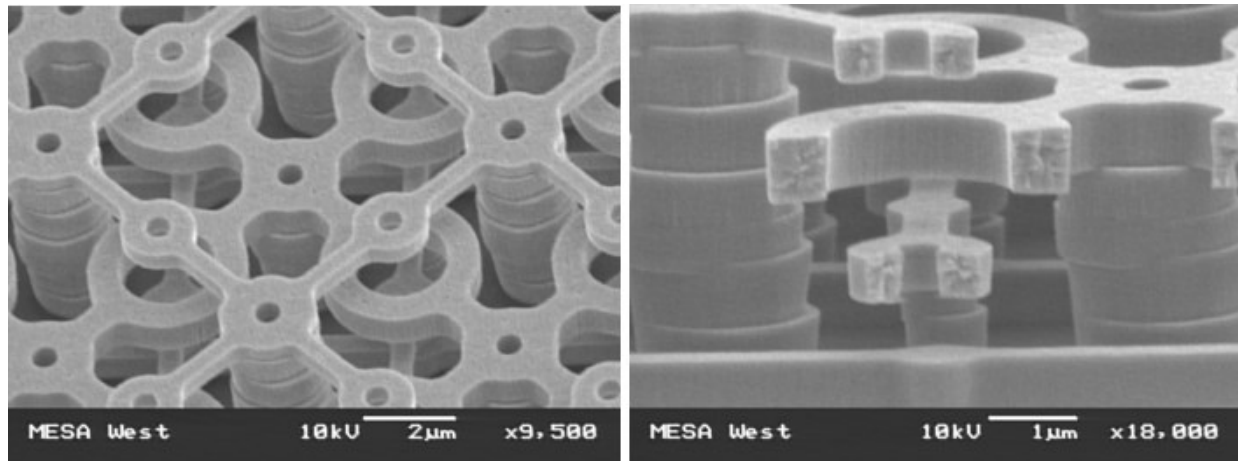


Figure 3-5: (left) A microfabricated CIT array. (right) Cross-sectional view. (unpublished photos)

There were a number of issues that appeared during experiments with microscopic CIT arrays. These issues included high capacitance produced by the array of electrodes, difficulty of wire bonding electrical connections to the traps, noise on the detector, electron field emissions within the traps, and overall mechanical strength of the features. After additional study was performed, it was also determined that the ion storage capacity of each trap was possibly limited to a single ion [73]. Additionally, on average, ions would leak out of the trap faster than they could be created. As a result, experiments were done with traps that were larger by as much as an order of magnitude [74]. This work demonstrated a fundamental limit in miniaturized ion trap storage capacity, demonstrating the need for traps to utilize alternative electrode arrangements with larger ion trap volumes.

Another example of microfabricated traps that has shown promising results is a coaxial ring ion trap [75]. Electrode features of this trap were created using deep reactive-ion etching of n-doped silicon-on-insulator. Figure 3-6 shows the completed electrode pattern of the coaxial ring ion trap.

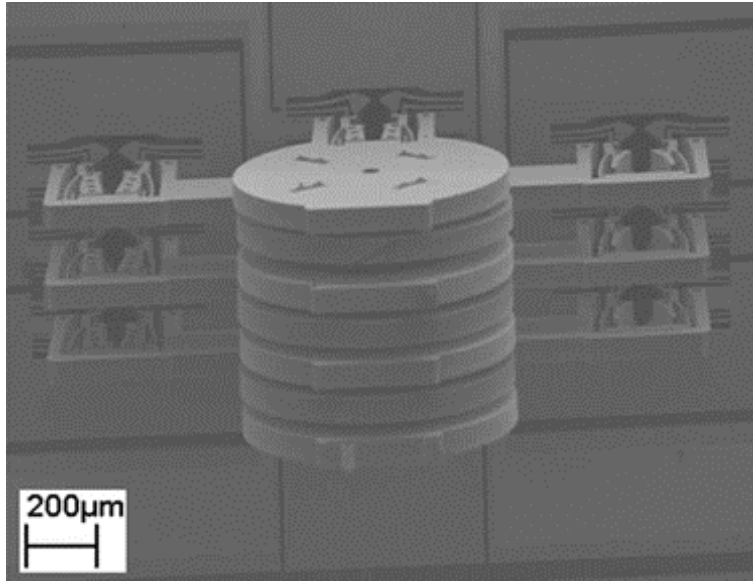


Figure 3-6: The coaxial ring ion trap. Figure from “Microelectromechanical System Assembled Ion Optics: An Advance to Miniaturization and Assembly of Electron and Ion Optics,” *Rev. Sci. Instrum.*, 80, p. 093302, 2009.

The RIT is a type of electrode arrangement that can possibly address the fundamental limits of miniaturized trap storage capacity by expanding the length of the ion storage region, but by conserving a miniaturized trapping volume along the axis of ion ejection. Additionally, the flat electrode composition of the RIT electrode geometry allows for precise fabrication. One example of work in arrays of miniaturized RIT arrays uses stereolithography [76, 77]. In this process, polymers are patterned into the shape of RIT electrodes and then undergo metal deposition. Figure 3-7 demonstrates a circular array of RITs fabricated by this process [1]. The circular array is important as it creates a uniform distance between all traps and the detector.

3.3.2.3 Single Planar Electrode Ion Traps

One of the complications of ion trap miniaturization is in maintaining the precision in the shape, smoothness, and alignment of electrodes as surface dimensions become increasingly small. Microfabrication techniques and simplified electrode geometry have been successful as

part of the process in creating CIT and RIT traps and mass filters. However, these methods have largely been used to help shape electrode structures in ways closely related to the Paul trap or one of the derivatives in Figure 3-1.

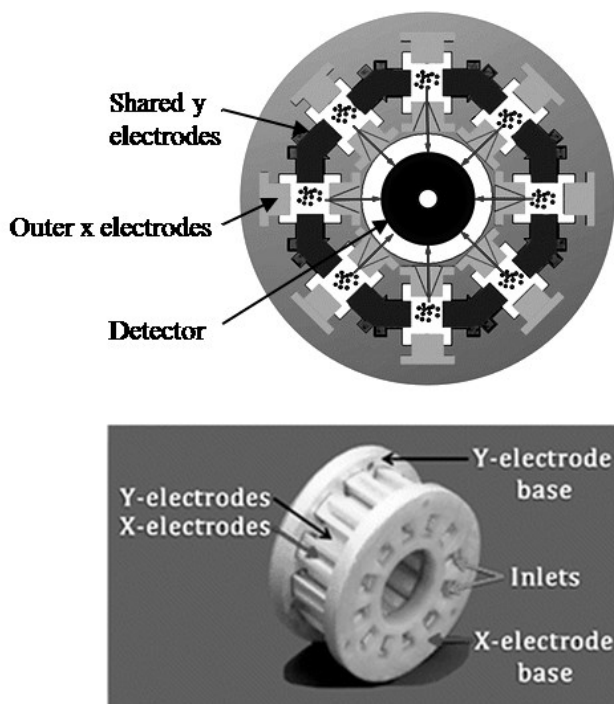


Figure 3-7: A circular array of polymer based miniaturized RITs. (top) Schematic view of the electrode arrangement. (bottom) Trap array assembly. Figure from “Circular arrays of polymer-based miniature rectilinear ion traps,” *Analyst*, 134, pp. 1338-1347, 2009.

An alternate method has focused on using patterns of discrete planar electrodes to create trapping fields. In this technique, patterns of concentric metal rings have been patterned onto an insulator. When appropriate RF potentials are applied to the metal patterns, trapping fields can be created.

One interesting example of a discrete patterned planar electrode device is shown in Figure 3-8 [78]. This example uses patterned rings on a single planar substrate to trap ions above the surface of the electrodes. This method has been demonstrated using between one and three

rings, with the corresponding electric field profile of the different numbers of rings also being demonstrated in the figure. The interaction of the electric field generated by each ring creates the total trapping potential above the surface of the substrate.

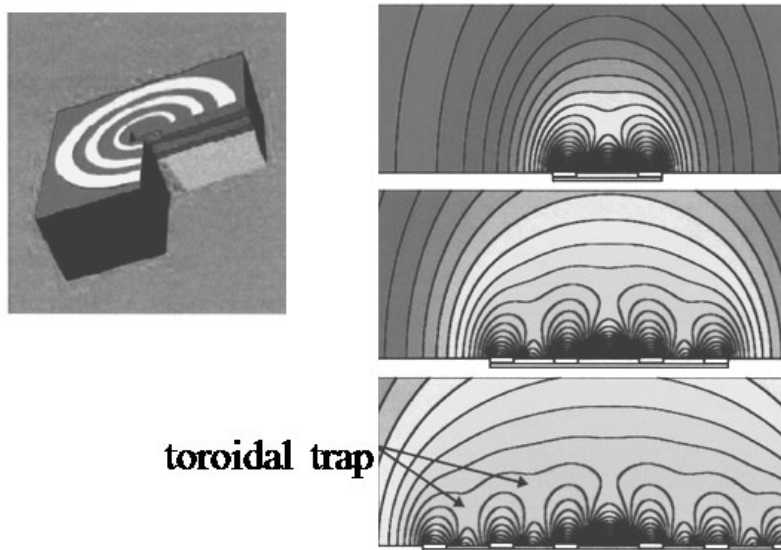


Figure 3-8: Single plate ion trap. (left) Schematic view of the trapping surface. (right) A cross-sectional view of the electric field profile using one, two, and three rings. Figure from “Planar Geometry for Trapping and Separating Ions and Charged Particles,” *Anal. Chem.*, 79, pp. 6857-6861, 2007.

3.4 Discrete Patterned Planar Electrode Traps

The focus of this work is on electrode surfaces with the patterning of metal electrodes onto a ceramic substrate. This method has been effective in allowing the flexibility to develop different classes of ion traps with only subtle changes in design, and with allowing the use of similar microfabrication processes. This technique utilizes a number of concentric metal rings or parallel metal lines on a substrate. The concentric metal rings are used when creating a planar Paul trap or a toroidal trap type of electric trapping field. The parallel lines are used when creating a linear or rectilinear type of ion trap. An example of an electrode surface capable of creating either a planar Paul trap or toroidal trap is shown in Figure 3-9. A type of electrode pattern used to create an RIT type trap is also shown in the figure.

In the planar Paul trap ring pattern, 24 concentric rings are patterned onto alumina. To create the trapping field, two of these patterned substrates are aligned to each other with the patterned sides shown in the figure facing each other. Designed magnitudes of RF potential are placed on each ring to create a specific trapping function.

In the RIT design, specific RF potentials are placed on each line that runs the length of the plate. A DC potential is applied on the two bars on either edge of the plate for the purpose of confining ions along the length of the trap. These types of trapped will be discussed in more detail later in this work.

A key element of this design is how it allows both a study and a tuning of higher order multipole components in the potential trapping function. In typical designs of traps, these components are designed by selecting the spacing and dimensions of the electrode surfaces. This means that whenever there may be a desire to alter the trapping potential function, the entire electrode assembly must be redesigned and rebuilt. This can be an expensive and time-consuming process. The ability to continuously make both subtle and large adjustments to the potential function is particularly relevant in the area of research and development, where all of the pertinent theory may not be fully developed.

This technique is also useful in the study of miniaturization effects of ion traps. When studying miniaturization and the gap between the two plates is narrowed, the voltage distribution on the electrode surfaces can be adjusted so that the potential trapping function can be preserved with respect to the relative weight of the higher order multipole components. This does not mean, however, that the design is immune to changes in the ion storage capacity of the miniaturized trapping region.

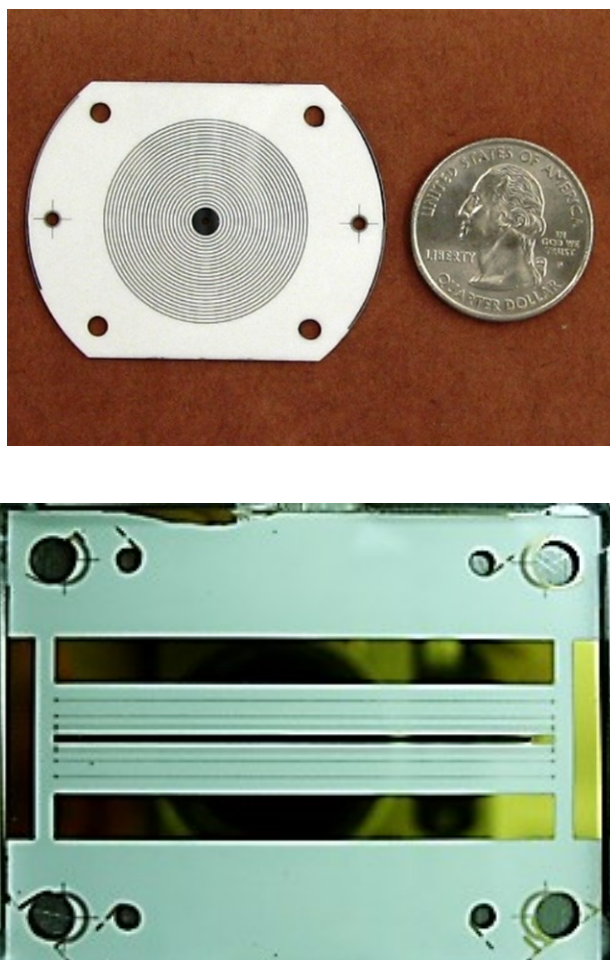


Figure 3-9: (top) A planar electrode pattern for creating a planar Paul trap. (bottom) A planar electrode pattern for creating an LIT type trap.

In conclusion, the goal towards miniaturized ion traps is progressing along varied pathways of development. The main obstacles to miniaturization include decreased ion storage capacity, the exact alignment of electrodes surfaces to each other, and the fabrication precision of electrodes. Processes that address these issues are capable of making great progress in creating miniaturized ion traps which, in turn, lead to more portable and less power-hungry mass analyzer systems. The development of the types of electrode surfaces in Figure 3-9 present a path capable of addressing all of these issues.

References

- [1] D. E. Austin and S. A. Lammert, "Mass Analyzer Miniaturization," in *The Encyclopedia of Mass Spectrometry, Volume 7, Mass Analysis and Associated Instrumentation*, Amsterdam, Netherlands, Elsevier Science, 2008.
- [2] M. Yang, T. -Y. Kim, S. -K. Y. H. -C. Hwang and D. -H. Kim, "Development of a Palm Portable Mass Spectrometer," *J. Am. Soc. Mass Spectrom.*, vol. 19, pp. 1442-148, 2008.
- [3] G. E. Patterson and B. A. Knecht, "Griffin Analytical Technologies: U.S. patent, 7161142," 2007.
- [4] L. Gao, A. Sugiarto, J. D. Harper, R. Cooks and Z. Ouyang, "Design and Characterization of a Multisource Hand-Held Tandem Mass Spectrometer," *Anal. Chem.*, vol. 80, pp. 7199-7205, 2008.
- [5] J. A. Contreras, J. A. Murray, S. E. O. J. L. Tolley, H. Tolley, S. A. Lammert, E. Lee, D. Later and M. Lee, "Hand-Portable Gas Chromatograph-Toroidal Ion Trap Mass Spectrometer (GC-TIMS) for Detection of Hazardous Compounds," *J. Am. Soc. Mass Spectrom.*, vol. 19, pp. 1425-14234, 2008.
- [6] C. M. Lock and E. W. Dyer, "Simulation of ion trajectories through a high pressure radio frequency only quadrupole collision cell by SIMION 6.0," *Rapid Commun. Mass Spectrom.*, vol. 13, pp. 422-431, 1999.
- [7] W. Xu, Q. Song, S. A. Smith, W. J. Chappell and Z. Ouyang, "Ion Trap Mass Analysis at High Pressure: A Theoretical View," *J. Am. Soc. Mass Spectrom.*, vol. 20, pp. 2144-2153, 2009.
- [8] F. A. Londry, R. L. Alfred and R. E. March, "Computer simulation of single-ion trajectories in Paul-type ion traps," *J. Am. Soc. Mass Spectrom.*, vol. 4, pp. 687-705, 1993.
- [9] W. B. Whitten, P. T. A. Reilly and J. M. Ramsey, "High-pressure ion trap mass spectrometry," *Rapid Commun. Mass Spectrom.*, vol. 18, pp. 1749-1752, 2004.
- [10] D. H. Holkeboer, T. L. Karandy, F. C. Currier, L. C. Frees and R. E. Ellefson, "Miniature Quadrupole Residual Gas Analyzer for Process Monitoring at Milli Torr Pressures," *J. Vac. Sci. Tech. A*, vol. 16, pp. 1157-1162, 1998.
- [11] J. M. Ramsey, P. T. A. Reilly, G. F. Verbeck and W. B. Whitten, "Micro Ion Trap Mass Spectrometry," in *52nd ASMS Conference on Mass Spectrometry and Allied Topics*, Nashville, TN, 2004.
- [12] E. R. Badman and R. G. Cooks, "Miniature Mass Analyzers," *J. Mass Spectrom.*, vol. 35, pp. 659-671, 2000.

- [13] D. Cruz, J. P. Chang and M. G. Blain, "Field Emission Characteristics of a Tungsten Microelectromechanical System Device," *Appl. Phys. Lett.*, vol. 86, p. 153502, 2005.
- [14] T. Ono, D. Y. Sim and M. Esashi, "Micro-discharge and Electric Breakdown in a Micro-gap," *J. Micromech. Microengin.*, vol. 10, pp. 445-451, 2000.
- [15] W. Xu, W. J. Chappell and R. G. Cooks, "Characterization of Electrode Surface Roughness and Its Impact on Ion Trap Mass Analysis," *J. Mass Spectrom.*, vol. 44, pp. 353-360, 2009.
- [16] Z. Ouyang and R. G. Cooks, "Miniature Mass Spectrometers," *Ann. Rev. Anal. Chem.*, vol. 2, pp. 187-214, 2009.
- [17] Z. Ouyang, L. Gao, M. Fico, W. J. Chappell, R. J. Noll and R. G. Cooks, "Quadrupole Ion Traps and Trap Arrays: Geometry, Material, Scale, Performance," *Eur. J. Mass Spectrom.*, vol. 13, pp. 13-18, 2007.
- [18] M. E. Bier and J. E. P. Syka, "U.S. Patent No. 5, 420,425," 1995.
- [19] J. Dress and W. Paul, "Beschleunigung von Elektronen in einem Plasmabetatron," *Z. Phys.*, vol. 180, pp. 340-361, 1964.
- [20] D. A. Church, "Storage-Ring Ion Trap Derived from the Linear Quadrupole Radio-Frequency Mass Filter," *J. Appl. Phys.*, vol. 40, pp. 3127-3134, 1969.
- [21] R. E. Kaiser Jr., J. N. Louris, J. W. Amy, R. G. Cooks and D. F. Hunt, "Extending the Mass Range of the Quadrupole Ion Trap Using Axial Modulation," *Rapid Commun. Mass Spectrom.*, vol. 30, pp. 225-229, 1989.
- [22] R. E. Kaiser, R. G. Cooks, G. C. Stafford, J. E. P. Syka and P. H. Hemberger, "Operation Ion Trap Mass-Spectrometer to Achieve High Mass Charge Ratios," *Int. J. Mass Spectrom.*, vol. 106, pp. 79-115, 1991.
- [23] J. E. Fulford, R. E. March, R. E. Mather, J. F. J. Todd and R. M. Waldren, "The Cylindrical Ion Trap - A Theoretical and Experiment Study," *Can. J. Spectroscopy*, vol. 25, pp. 85-97, 1980.
- [24] D. B. Langmuir, R. V. Langmuir, H. Shelton and R. F. Wuerker, "US Patent #3,065,640," 1962.
- [25] R. F. Bonner, J. E. Fulford and R. E. March, "The Cylindrical Ion Trap. Part 1. General Introduction," *Int. J. Mass Spectrom. Ion Phys.*, vol. 24, pp. 255-269, 1977.
- [26] H. G. Dehmelt, "Radiofrequency Spectroscopy of Stored Ions I. Storage," *Adv. At. Mol. Phys.*, vol. 3, pp. 53-72, 1967.
- [27] H. G. Dehmelt, "Radiofrequency Spectroscopy of Stored Ions II. Spectroscopy," *Adv. At. Mol. Phys.*, vol. 3, pp. 53-72, 1967.

- [28] W. M. Davis, M. B. Wise, J. S. Furey and C. V. Thompson, "Rapid Detection of Volatile Organic Compounds in Groundwater by in situ Purge and Direct-sampling Ion-trap Mass Spectrometry," *Field Anal. Chem. Tech.*, vol. 2, pp. 89-96, 1998.
- [29] J. Costanza and W. M. Davis, "Rapid Detection of Volatile Organic Compounds in the Subsurface by Membrane Introduction into a Direct Sampling Ion-Trap Mass Spectrometer," *Field Anal. Chem. Tech.*, vol. 4, pp. 246-254, 2000.
- [30] J. M. Wells, E. R. Badman and R. G. Cooks, "A quadrupole ion trap with cylindrical geometry operated in the mass selective instability mode," *Anal. Chem.*, vol. 70, pp. 438-444, 1998.
- [31] Z. Ouyang and R. G. Cooks, "Rectilinear Ion Trap and Mass Analyzer System and Method. U.S. Patent #6,838,666," 2005.
- [32] Z. Ouyang, G. Wu, Y. Wong, H. Li, W. Plass and R. Cooks, "Rectilinear ion trap: Concepts, calculations, and analytical performance of a new mass analyzer," *Anal. Chem.*, vol. 76, pp. 4595-4605, 2004.
- [33] R. Song, G. Wu, Q. Song, R. G. Cooks, Z. Ouyang and W. R. Plass, "Novel Linear Ion Trap Mass Analyzer Composed of Four Planar Electrodes," *J. Am. Soc. Mass Spectrom.*, vol. 17, pp. 631-639, 2006.
- [34] A. M. Tabert, M. P. Goodwin and R. G. Cooks, "Co-occurrence of Boundary and Resonance Ejection in a Multiplexed Rectilinear Ion Trap Mass Spectrometer," *J. Am. Soc. Mass Spectrom.*, vol. 17, pp. 56-59, 2006.
- [35] G. Wu, R. G. Cooks, Z. Ouyang, M. Yu, W. J. Chappell and W. R. Plass, "Ion Trajectory Simulation for Electrode Configurations with Arbitrary Geometries," *J. Am. Soc. Mass Spectrom.*, vol. 17, pp. 1216-1228, 2006.
- [36] A. M. Tabert, M. P. Goodwin, J. S. Duncan, C. D. Fico and R. G. Cooks, "Multiplexed Rectilinear Ion Trap Mass Spectrometer for High-Throughput Analysis," *Anal. Chem.*, vol. 78, pp. 4830-4838, 2006.
- [37] S. Kothari, Q. Song, Y. Xia, M. Fico, D. Taylor, J. W. Amy, G. Stafford and R. G. Cooks, "Multiplexed Four-Channel Rectilinear Ion Trap Mass Spectrometer," *Anal. Chem.*, vol. 81, pp. 1570-1579, 2009.
- [38] Q. Song, S. Kothari, M. A. Senko, J. C. Schwartz, J. W. Amy, G. C. Stafford, R. G. Cooks and Z. Ouyang, "Rectilinear Ion Trap Mass Spectrometer with Atmospheric Pressure Interface and Electrospray Ionization Source," *Anal. Chem.*, vol. 78, pp. 718-725, 2006.
- [39] A. Keil, N. Talaty, C. Janfelt, R. J. Noll, L. I Gao, Z. Ouyang and R. G. Cooks, "Ambient Mass Spectrometry with a Handheld Mass Spectrometer at High Pressure," *Anal. Chem.*, vol. 79, pp. 7734-7739, 2007.

- [40] L. Gao, Q. Song, G. E. Patterson, R. G. Cooks and Z. Ouyang, "Handheld Rectilinear Ion Trap Mass Spectrometer," *Anal. Chem.*, vol. 78, pp. 5994-6002, 2006.
- [41] X. Li, G. Jiang, C. Luo, F. Xu, Y. Wang, L. Ding and C. F. Ding, "Ion Trap Array Mass Analyzer: Structure and Performance," *Anal. Chem.*, vol. 81, pp. 4840-4846, 2009.
- [42] R. R. A. Syms, T. J. Tate, M. M. Ahmad and S. Taylor, "Fabrication of a Microengineered Quadrupole Electrostatic Lens," *Electron. Lett.*, vol. 32, pp. 2094-2095, 1996.
- [43] S. Taylor, J. J. Tunstall, R. R. A. Syms, T. Tate and M. M. Ahmad, "Initial Results for a Quadrupole Mass Spectrometer with a Silicon Micromachined Mass Filter," *Electron. Lett.*, vol. 34, pp. 546-547, 1998.
- [44] R. R. A. Syms, T. J. Tate, M. M. Ahmad and S. Taylor, "Design of a Microengineered Electrostatic Quadrupole Lens," *IEEE Trans. Electron Dev.*, vol. 45, pp. 2304-2311, 1998.
- [45] S. Taylor, R. F. Tindall and R. R. A. Syms, "Silicon Based Quadrupole Mass Spectrometry Using Microelectromechanical Systems," *J. Vac. Sci. Tech. B*, vol. 19, pp. 557-562, 2001.
- [46] J. R. Gibson and S. Taylor, "Prediction of Quadrupole Mass Filter Performance for Hyperbolic and Circular Cross Section Electrodes," *Rapid Commun. Mass Spectrom.*, vol. 14, pp. 1669-1673, 2000.
- [47] J. R. Gibson and S. Taylor, "Numerical Investigation of the Effect of Electrode Size on the Behaviour of Quadrupole Mass Filters," *Rapid Commun. Mass Spectrom.*, vol. 15, pp. 1960-1964, 2001.
- [48] S. Wright, R. R. A. Syms, S. O'Prey, G. Hong and A. S. Holmes, "Comparison of Ion Coupling Strategies for a Microengineered Quadrupole Mass Filter," *J. Am. Soc. Mass Spectrom.*, vol. 20, pp. 146-156, 2009.
- [49] R. R. A. Syms, "Monolithic Micro-engineered Mass Spectrometer, U. S. Patent #7,208,729 B2," 2007.
- [50] M. Gear, R. R. A. Syms, S. Wright and A. S. Holmes, "Monolithic MEMS Quadrupole Mass Spectrometers by Deep Silicon Etching," *J. Microelectromechanical Sys.*, vol. 14, pp. 1156-1166, 2005.
- [51] L. F. Velasquez-Garcia, K. Cheung and A. I. Akinwande, "An Application of 3-D MEMS Packagin: Out-of-Plane Quadrupole Mass Filters," *J. Microelectromechanical. Sys.*, vol. 17, pp. 1430-1438, 2008.
- [52] L. F. Velasquez-Garcia and A. I. Akinwande, "An Out-of-Plane MEMS Quadrupole for a Portable Mass Spectrometer," in *Proceedings of the Solid State Sensors, Actuators and Microsystems Conference*, 2215-2320, 2008.
- [53] O. Kornienko, P. T. A. Reilly, W. B. Whitten and J. M. Ramsey, "Micro ion trap mass spectrometry," *Rapid Commun. Mass Spectrom.*, vol. 13, pp. 50-53, 1999.

- [54] O. Kornienko, P. T. A. Reilly, W. B. Whitten and J. M. Ramsey, "Electron Impact Ionization in a Microion Trap Mass Spectrometer," *Rev. Sci. Instr.* 1999, vol. 70, pp. 3907-3909, 1999.
- [55] O. Kornienko, P. T. A. Reilly, W. B. Whitten and J. M. Ramsey, "Field-Emission Cold-Cathode EI Source for a Microscale Ion Trap Mass Spectrometer," *Anal. Chem.*, vol. 72, pp. 559-562, 2000.
- [56] J. Moxom, P. T. A. Reilly, W. B. Whitten and J. M. Ramsey, "Sample Pressure Effects in a Micro Ion Trap Mass Spectrometer," *Rapid Commun. Mass Spectrom.*, vol. 18, pp. 721-723, 2004.
- [57] J. Moxom, P. T. A. Reilly, W. B. Whitten and J. M. Ramsey, "Double Resonance Ejection in a Micro Ion Trap Mass Spectrometer," *Rapid Commun. Mass Spectrom.*, vol. 16, pp. 755-760, 2002.
- [58] J. Moxom, P. T. A. Reilly, W. B. Whitten and J. M. Ramsey, "Analysis of Volatile Organic Compounds in Air with a Micro Ion Trap Mass Analyzer," *Anal. Chem.*, vol. 75, pp. 3739-3743, 2003.
- [59] E. R. Badman, R. C. Johnson, W. R. Plass and R. G. Cooks, "A miniature cylindrical quadrupole ion trap: Simulation and experiment," *Anal. Chem.*, vol. 70, pp. 4896-4901, 1998.
- [60] G. E. Patterson, A. J. Guymon, L. S. Riter, M. Everly, J. Griep-Raming, B. Laughlin, Z. Ouyang and R. G. Cooks, "Miniature Cylindrical Ion Trap Mass Spectrometer," *Anal. Chem.*, vol. 74, pp. 6145-6153, 2002.
- [61] L. S. Riter, Y. Peng, R. J. Noll, G. E. Patterson, T. Aggerholm and R. G. Cooks, "Analytical Performance of a Miniature Cylindrical Ion Trap Mass Spectrometer," *Anal. Chem.*, vol. 74, pp. 6154-6162, 2002.
- [62] W. G., R. G. Cooks and Z. Ouyang, "Geometry Optimization for the Cylindrical Ion Trap: Field Calculations, Simulations and Experiments," *Int. J. Mass Spectrom.*, vol. 241, pp. 119-132, 2005.
- [63] L. S. Riter, E. C. Meurer, E. S. Handberg, B. C. Laughlin, H. Chen, G. E. Patterson, M. N. Eberlin and R. G. Cooks, "Ion/molecule Reactions Performed in a Miniature Cylindrical Ion Trap Mass Spectrometer," *Analyst*, vol. 128, pp. 1112-1118, 2003.
- [64] B. C. Laughlin, C. C. Mulligan and R. G. Cooks, "Atmospheric Pressure Ionization in a Miniature Mass Spectrometer," *Anal. Chem.*, vol. 77, pp. 2928-2939, 2005.
- [65] L. S. Riter, E. C. Meurer, I. Cotte-Rodrigues, M. N. Eberlin and R. G. Cooks, "Solid Phase Micro-extraction in a Miniature Ion Trap Mass Spectrometer," *Analyst*, vol. 128, pp. 1119-1122, 2003.

- [66] L. S. Riter, B. C. Laughlin, E. Nikolaev and R. G. Cooks, "Direct Analysis of Volatile Organic Compounds in Human Breath Using a Miniaturized Cylindrical Ion Trap Mass Spectrometer with a Membrane Inlet," *Rapid Commun. Mass Spectrom.*, vol. 16, pp. 2370-2373, 2002.
- [67] P. T. A. Reilly, O. Kornienko, W. B. Whitten and J. M. Ramsey, "Microscale Ion Traps: 2-Dimensional Arrays," in *48th Conference on Mass Spectrometry and Allied Topics*, Long Beach, CA, 2000.
- [68] Z. Ouyang, E. R. Badman and R. G. Cooks, "Characterization of a serial array of miniature cylindrical ion trap mass analyzers," *Rapid Commun. Mass Spectrom.*, vol. 13, pp. 2444-2449, 1999.
- [69] E. R. Badman and R. G. Cooks, "A Parallel Miniature Cylindrical Ion Trap Array," *Anal. Chem.*, vol. 72, pp. 3291-3297, 2000.
- [70] A. M. Tabert, J. Griep-Raming, A. J. Guymon and R. G. Cooks, "High-throughput Miniature Cylindrical Ion Trap Array Mass Spectrometer," *Anal. Chem.*, vol. 75, pp. 5656-5664, 2003.
- [71] A. M. Tabert, A. S. Misharin and R. G. Cooks, "Performance of a Multiplexed Chemical Ionization Miniature Cylindrical Ion Trap Array Mass Spectrometer," *Analyst*, vol. 129, pp. 323-330, 2004.
- [72] M. G. Blain, L. S. Riter, D. Cruz, D. E. Austin, G. X. Wu, W. R. Plass and R. G. Cooks, "Toward the hand-held mass spectrometer: design considerations, simulation, and fabrication of micrometer-scaled cylindrical ion traps," *Int. J. Mass Spectrom.*, vol. 236, pp. 92-104, 2004.
- [73] D. E. Austin, D. Cruz and M. G. Blain, "Simulations of Ion Trapping in a Micrometer-Sized Cylindrical Ion Trap," *J. Am. Soc. Mass Spectrom.*, vol. 17, pp. 430-441, 2006.
- [74] D. Cruz, J. P. Chang, M. Fico, A. J. Guymon, D. E. Austin and M. G. Blain, "Design, Microfabrication, and Analysis of Micrometer-sized Cylindrical Ion Trap Arrays," *Rev. Sci. Instr.*, vol. 78, p. 015107 (9 pages), 2007.
- [75] J. Fox, R. Saini, K. Tsui and G. Verbeck, "Microelectromechanical System Assembled Ion Optics: An Advance to Miniaturization and Assembly of Electron and Ion Optics," *Rev. Sci. Instr.*, vol. 80, p. 093302 (6 pages), 2009.
- [76] M. Yu, M. Fico, S. Kothari, Z. Ouyang and W. J. Chappell, "Polymer-based Ion Trap Chemical Sensor," *IEEE Sensors J.*, vol. 6, pp. 1429-1434, 2006.
- [77] M. Fico, J. D. Maas, S. A. Smith, A. B. Costa, Z. Ouyang, W. J. Chappell and R. G. Cooks, "Circular Arrays of Polymer-based Miniature Rectilinear Ion Traps," *Analyst*, vol. 134, pp. 1338-1347, 2009.
- [78] S. Pau, W. B. Whitten and J. M. Ramsey, "Planar Geometry for Trapping and Separating Ions and Charged Particles," *Anal. Chem.*, vol. 79, pp. 6857-6861, 2007.

4 ION TRAP FABRICATION

4.1 Development History

The development of the ion traps in this work has been the result of collaboration between the BYU Electrical and Computer Engineering (ECEN) department, the BYU Chemistry and Biochemistry (CHEM) department, and Torion Technologies. The goal of this collaboration has been to create planar ion trap designs.

The ECEN department has contributed all microfabrication processing and design with its Integrated Microfabrication Laboratory (IML) facility. The CHEM department has led in efforts to conceptually design various ion trap configurations and has overseen the various mass spectrometry experiments that tested those designs. Torion has provided consultation, support, and various electronics components throughout this process.

All ion trap designs had to take into account the equipment specifications of the IML. As the IML produces components for a great variety of projects, this has often meant tailoring designs and process recipes to take advantage of the strengths and minimize the drawbacks of existing IML processing equipment. One consequence of this requirement is the development of customized microfabrication techniques. Another consequence was seen in the designs of the trap themselves as successive designs of devices were tweaked to more closely align with reproducible fabrication recipes. The end result of this development process is that each generation of trap was designed with two objectives:

1. Improve ion trap performance.
2. Increase the process yield rate.

At times, these goals presented conflicting solutions where initially one avenue would need to be chosen at some cost to the other.

The first generation of ion trap was realized using a 4" silicon wafer, the standard processing substrate type and size in the IML. This trap consisted of an array of holes chemically etched through the wafer with the edges of the holes being subsequently covered in metal. To conduct mass analyzer experiments, this design would stack two of these substrates on top of each other with a small gap separating them. An RF trapping potential would then be applied to the metal coating the edges of the etched holes. Each square would create a trapping field, resulting in an ion trap array with ions stored between the etched squares. This design is demonstrated in Figure 4-1.

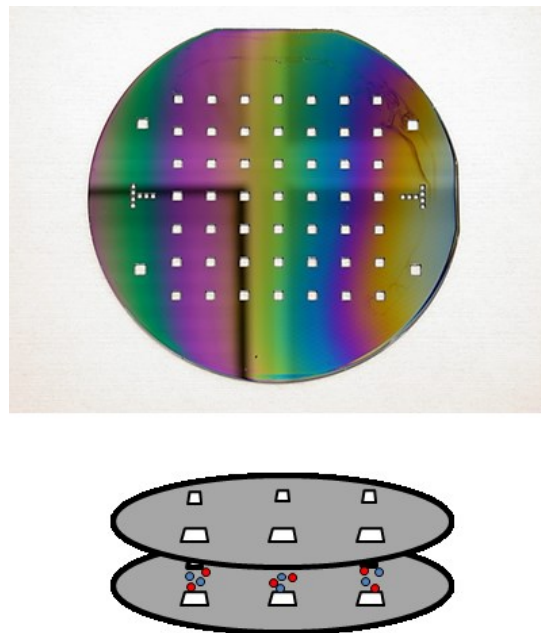


Figure 4-1: The ion trap array on silicon. (top) Completed wafer substrate. (bottom) Electrode arrangement and ion storage areas are shown.

The holes in the silicon were etched using standard IML processes and materials. This process used a potassium hydroxide (KOH) solution as an etchant. The etchant mask had to be a material that would etch at a much slower rate than the silicon. As KOH etches polymer based photoresists, a 300 nm thick layer of LPCVD (low pressure chemical vapor deposition) grown silicon-nitride coated with a 2.0 micron PECVD (plasma enhanced chemical vapor deposition) grown silicon-dioxide was coated over the wafer and then patterned into an etching mask using CF₄ based plasma etching. Silicon nitride and silicon dioxide have long been used as masks for KOH etching [1]. KOH etching was done in a solution heated to approximately 70° C, using a specially designed wafer holder made from Teflon. The holder incorporated a silicone ring that sealed to the top edge of the wafers, thus preventing KOH from contacting and etching the edges and backside of the wafer. The square holes shown in Figure 4-1 have sides of length 2.0 mm at the bottom of the etched hole. The space between each trap was 9.0 mm.

One drawback of this design was in the high capacitance formed from the array of electrodes. The substrate itself is the source of this high capacitance, as the silicon wafer acts as a single conductive surface. To address this problem, a new design was created using a geometrically smaller array of traps that also consisted of smaller holes. In this design, the array consisted of squares with a side length of 0.57 mm at the bottom of the etched hole. The space between traps in this design was 3.0 mm. This wafer design is shown in Figure 4-2. Capacitance in this design was dropped to less than 10% of the original design.

In the end, these traps proved unsuccessful in producing any useful mass analyzer signal. One reason for this was determined to be the inability to create and trap ions faster than ions would leak out of the trap, just as happened in other ion trap arrays discussed in this work [2]. However, an additional factor in the poor trapping efficiency was due likely to the electrode

geometry, rather than to an overly small trapping volume. For example, as this electrode arrangement is more suited to a Paul type trap, a circular hole would provide a more ideal geometry. KOH etching of silicon is unable to achieve this geometry.

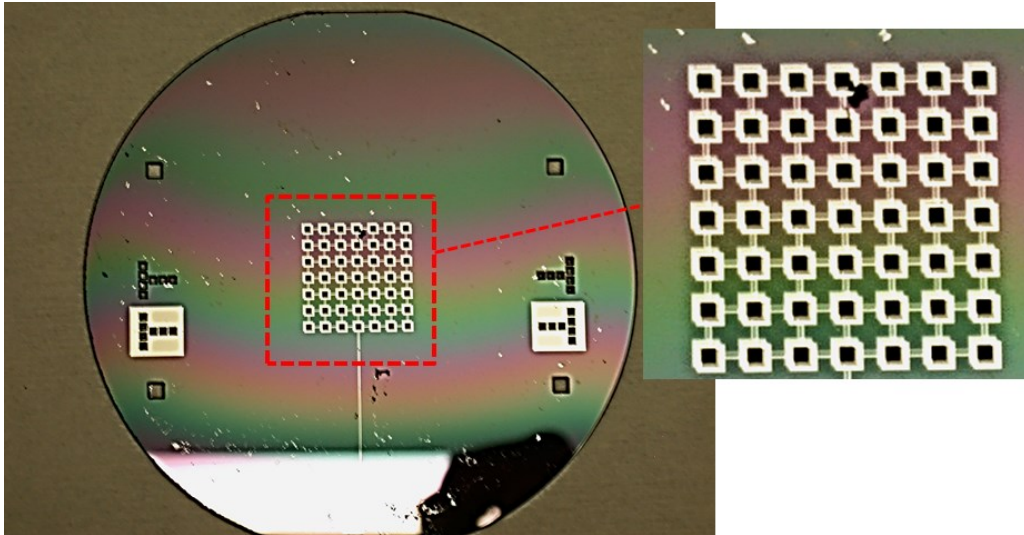


Figure 4-2: The second generation of the silicon-etched trap array.

The most pronounced characteristic of KOH etching with silicon is the anisotropic etching profile. Silicon etches quickly in KOH along the $\langle 100 \rangle$ and $\langle 110 \rangle$ planes of the crystal, but much slower along the $\langle 111 \rangle$ plane. This profile creates a 54.75° angle between the $\langle 110 \rangle$ and $\langle 111 \rangle$ directions of the silicon lattice. Due to this behavior, the shape of etched holes is constrained to be rectangular. When used for ion traps, this resulted in electrodes with sharp points within critical points of the ion trapping volume. The sharp points deform the trapping field in undesirable ways. This fabrication constraint contributed to the poor performance of this early design.

An additional issue to consider is that this angled etching profile creates a hole that is wider at the top of the wafer than at the bottom of the hole. This lack of uniformity is an

additional processing constraint that affects this design's ability to create quality trapping fields. Figure 4-3 helps show the extent of this effect.

Due to the constraints on electrode geometry, it was determined that the KOH etching method was not capable of meeting the design requirements for planar ion traps. Furthermore, because the trapping efficiency of the electrode design was so poor, it was determined that an alternative approach to the layout would be needed to create a viable mass analyzer.

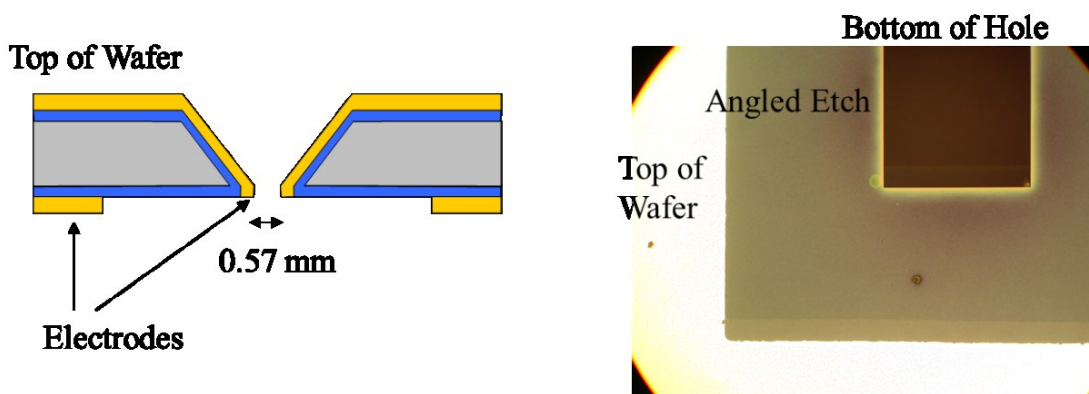


Figure 4-3: (left) A cross-sectional view of an individual trapping electrode geometry. (right) A microscope picture taken of the etched hole.

The concept of an arrayed trap was abandoned in favor of pursuing a single larger trap. It was determined that a focused approach on single large traps would provide a quicker path to understanding the intricacies of planar trap operation.

The next design began the use of concentric metal rings as the electrode pattern. The set of electrodes are all used together to compose a single ion trap. With the concentric ring design, the potential trapping function was dictated by the relative magnitudes of RF potential applied to the different rings. In this way, the effective shape of the electrode structure could be altered to create a more ideal trapping function.

In the first generation of this layout, 15 metal rings were patterned over the top of a 4” silicon wafer. Circular alignment holes and a hole for ion ejection were cut into the wafer by laser-cutting methods, which replaced the process of creating holes with chemical etching. The central hole had a diameter of 4.8 cm. The finished substrate is shown in Figure 4-4.

This arrangement of electrodes is best suited for a toroidal type of ion trap due to the large hole cut into the center of the wafer. A large toroidal trap, with its increased ion storage capacity, was selected to guarantee a much larger trapping efficiency than was previously seen in the arrayed design. Figure 4-5 demonstrates the arrangement of the electrode surfaces and the location of the trapping region. As ions are ejected, they travel to the center hole and then out to the detector. The full description of the operation of a toroidal trap is discussed later in Chapter 5 of this work.

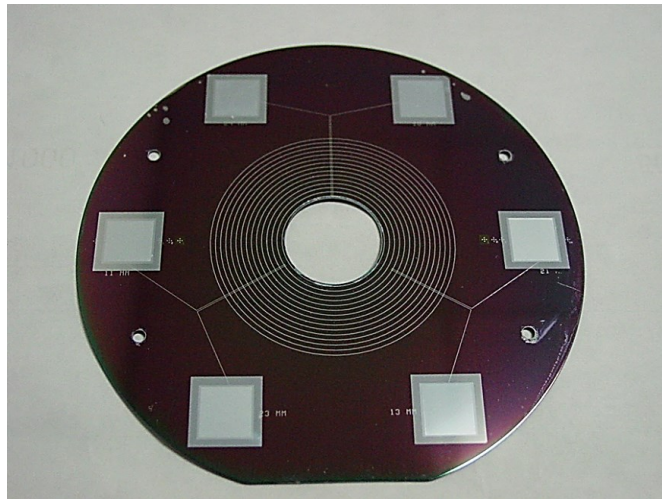


Figure 4-4: The metal on silicon ring design.

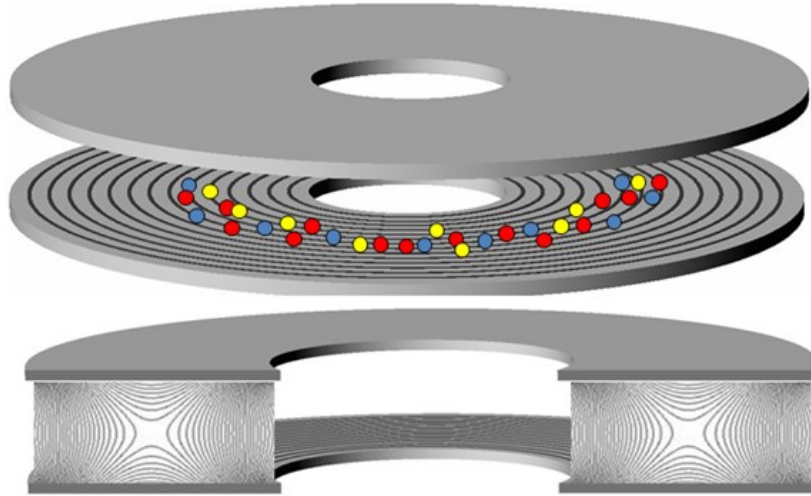


Figure 4-5: (top) Arrangement of the metal on silicon toroidal trap. (bottom) A cross-sectional view of the contour plot of the trapping field.

Various RF potentials were attached to the edges of the wafer, and then metal leads that spanned the ring area connected specific rings to the desired electric potential. The fabrication of this structure required various layers to make the necessary electrical connections. The steps are diagrammed with a cross-sectional view in Figure 4-6. Oxide was initially grown (using PECVD) as an insulating layer on silicon. Then metal was deposited and patterned into the traces that would span the rings. Another insulating oxide layer was then grown over the features. Small vias were then etched into the oxide to open up a path for connecting the rings to the RF potentials. Metal rings were then patterned that ran over the top of these vias, electrically connecting them to the metallized contact squares on the edge of the wafer. These squares were used for packaging purposes to apply the specific RF potentials. Finally, a resistive layer was grown over the rings. The resistive layer helped to smooth the potential function over the electrode surface and helped to limit space charge effects.

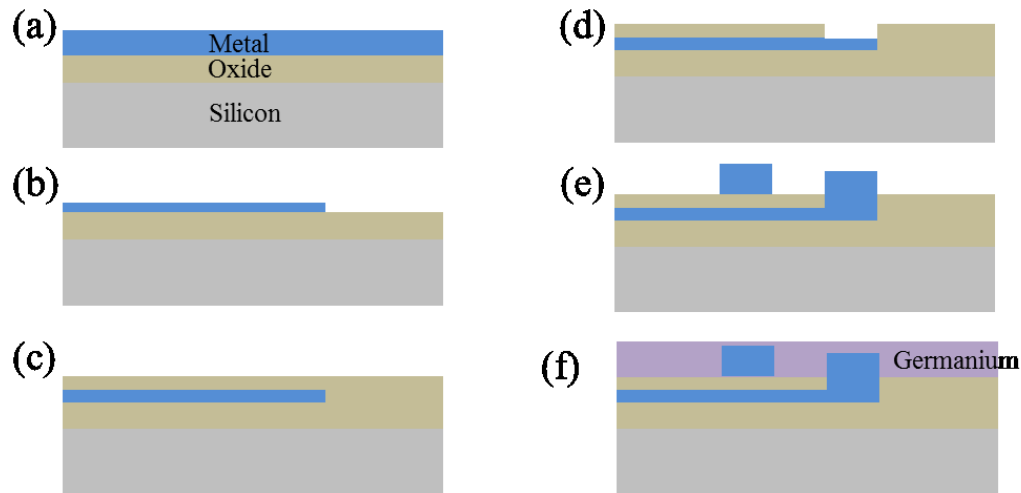


Figure 4-6: A cross-sectional view of the fabrication process for the metal on silicon trap. (a) Metal deposited on silicon with an oxide layer, (b) metal patterned into RF leads, (c) oxide grown as an insulative layer, (d) vias etched into the oxide, (e) rings patterned onto the substrate, (f) resistive germanium layer deposited over the rings.

Due to the silicon substrate acting as a large conducting plane, this design had a high trap capacitance, causing excessive dissipation of RF energy. The only way to lower the capacitance with a silicon substrate was to change the initial oxide thickness. Changing the oxide thickness, however, can only make marginal improvements in the capacitance between the substrate and the patterned electrodes. The patterned electrodes could also be made smaller, but there are practical limits using this method.

The next generation of ion trap involved a change in base substrate material. It was important to limit the capacitance of the trap. An insulating substrate dropped the capacitance from the pads and the rings to zero. Various insulating substrates were explored, including glass, lead-glass, and ceramic. Eventually a type of ceramic was selected due to its common use and availability. An aluminum oxide ceramic (Hybrid-Tek, Clarksburg, NJ) was selected as an appropriate material to reduce substrate capacitance.

Patterning on ceramic requires extra steps in the microfabrication process. First, when dealing with ceramic, extra cleaning steps are required to improve metal adhesion to the substrate. To properly clean the substrate requires the use of acids, bases, detergents, solvents, and plasmas. Second, the metal that was selected for the patterning was gold. However, gold adheres poorly to ceramic. A thin layer of chrome was initially deposited as a sticking layer for the gold [3]. Finally, after the patterning of the rings, germanium was deposited over the surface of the substrate. The germanium serves two purposes. The primary purpose is to prevent space charge build up on the substrate. The secondary purpose is to smooth the potential distribution across the area of the rings. The germanium overcoat created a uniform logarithmic field profile over the entire electrode area.

Initially, ion trap designs using the same electrode layout as Figure 4-4 were attempted with ceramic. One problem with the electrode layout of Figure 4-4 is from the leads that span the rings. While these leads are narrow, there will still be a contribution from these leads to the potential function of the trap. Due to the asymmetry and location of these leads, it is impossible to compensate for this contribution. It is desirable to apply the RF potentials to the rings in such a way as to not interfere with the electric field within the trap.

A major breakthrough involved using the backside of the substrate to make electrical contact between the rings and the RF potentials. By placing the RF leads out of the trapping area, trapping fields would achieve much better symmetry in the trapping volume and would align more closely with ideal quadrupole fields. These designs were the first ones to begin to produce quality levels of mass analysis data. All future designs would utilize the back side of the substrates in their packaging.

The first design to incorporate backside packaging is shown in Figure 4-7. In this design, the ceramic substrate had small holes laser cut within the ring pathways to form a conduit for electrical connections to the back side of the substrate. In this initial effort at backside packaging, these connections were made by feeding wires through the vias and then using epoxy to secure the connection. This fabrication process is shown in Figure 4-8.

This design represented several significant breakthroughs in the development process of the discrete patterned electrode ion traps. This was the first design that began to achieve significant levels of ion signal. Packaging with this design also was easier than trying to run all electronic signals along only one side of the substrate. Moreover, this plate allowed for progress towards the goal of miniaturization. The central hole was shrunk down to a size of 2.4 cm. Furthermore, since the need to fit all electrical connections on one side of the substrate was eliminated, the substrate itself could be made smaller to the point to where very little space was needed beyond the area covered by the rings.

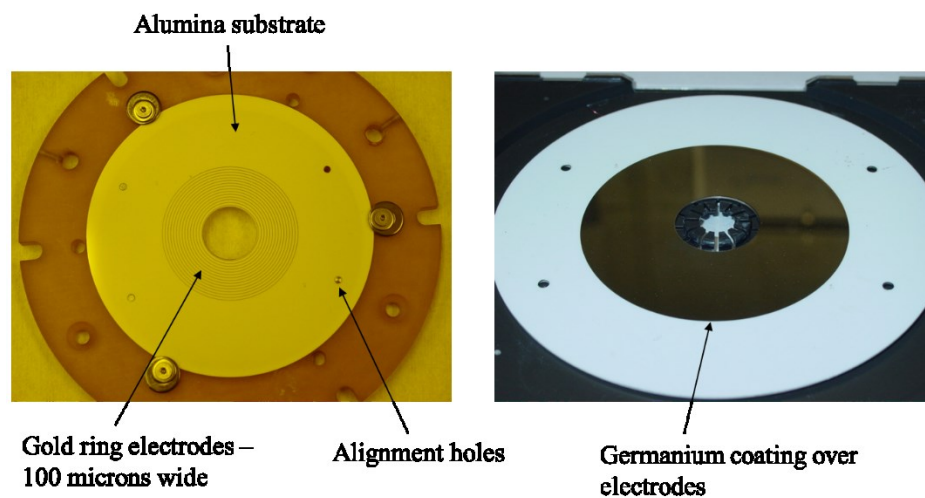


Figure 4-7: (left) Patterning of rings on ceramic substrate. (right) Finished substrate after depositing germanium over rings.

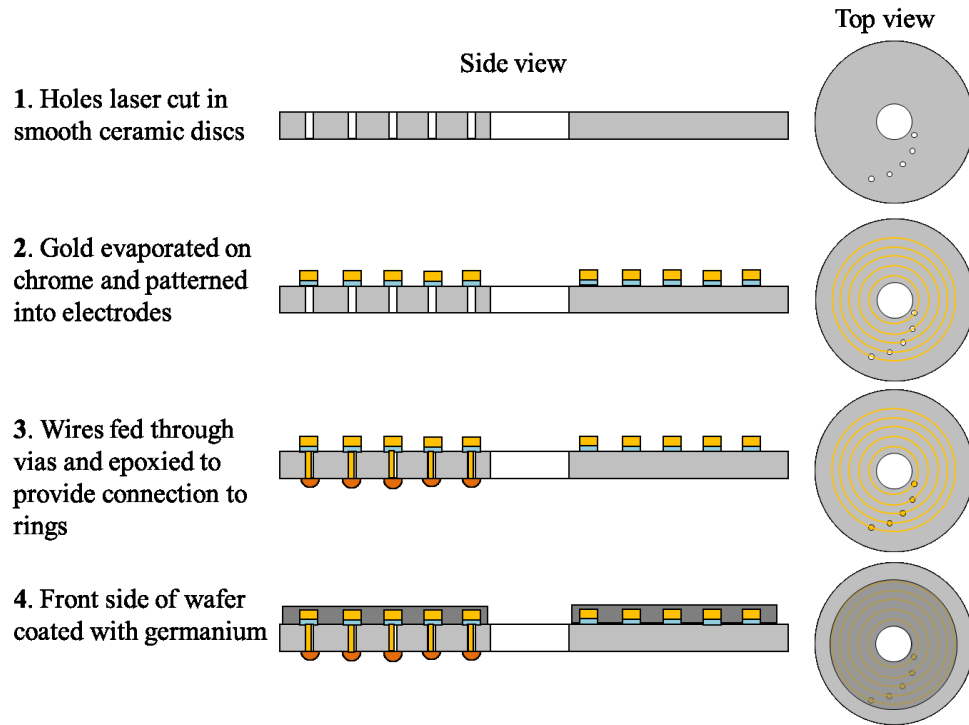


Figure 4-8: Fabrication process for the first design to incorporate back-side packaging.

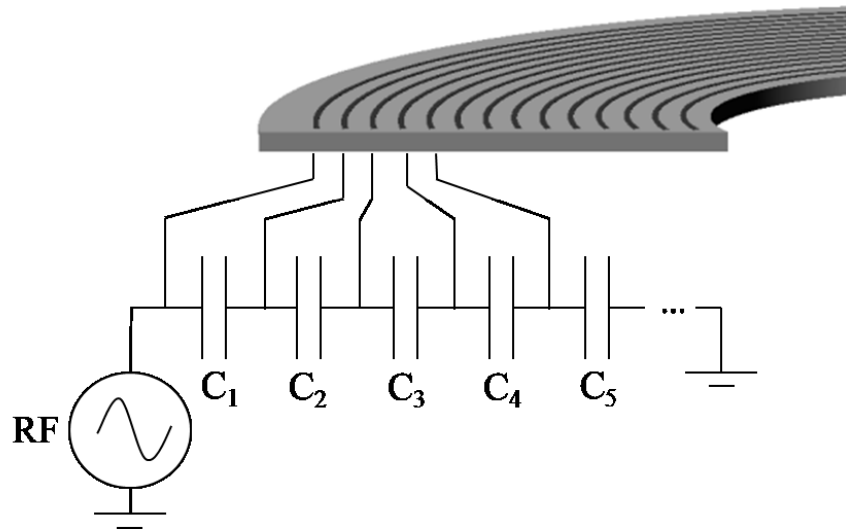


Figure 4-9: The circuit representation for the back-side packaging design.

While the first attempt at back-side packaging was a significant improvement over previous designs, it was not without its drawbacks. The threading of wires through small vias still presented an intense and weighty amount of manual processing. The off-substrate packaging was also unwieldy and awkward. The electrode rings required various magnitudes of RF potential. In order to create the different magnitudes, the RF power supply was connected to a capacitive voltage-divider circuit. The rings were then attached to different nodes of the voltage divider circuit, as shown in Figure 4-9.

The ensuing design was made to simplify the packaging, leading to a more efficient and consistent process. In original designs, the capacitive voltage-divider circuit was set up independent of the ceramic substrate. In the next step of ion trap design, this circuit was soldered directly to metal patterned onto the backside of the substrate. In order to eliminate the need to feed wires by hand, the vias that connected the rings to the non-trapping side were filled by the vendor with a gold-tungsten alloy during the fabrication of the plate substrate itself. However, the yield of this process was unacceptable. Solder would not stick easily to the back side of the substrate, it would alloy with metal traces, and it was difficult to remove capacitors if voltage levels needed to be changed. When capacitors needed to be removed, they would often remove large chunks of metal with them. Furthermore, when attempting to clean off plates in order to recycle them by re-patterning all the metal, the solder would sometimes leave a lasting residue on the ceramic that frustrated efforts to cleanly perform lithographic processes. This design was the final stepping stone to current ion trap designs. Future iterations would go back to using the voltage-divider circuit off-substrate, but with customized circuit boards designed to fit closely to and work with metal patterning on the back side of the ceramic.

4.2 Current Designs

The current ion trap design utilizes metal electrodes patterned onto a ceramic substrate. The trapping electrodes electrically connect to the back side of the ceramic by way of metal-filled vias. The back side of the substrate is patterned with contact points for a printed circuit board (PCB) upon which is a capacitive voltage-divider circuit. The PCB is shaped to fit closely to the ceramic to minimize packaging size. The PCB design includes gold-coated spring-loaded pogo pins. The pogo pins electrically connect to the nodes of the capacitive voltage-divider circuit, and then are compressed into the back side of the ceramic pattern to make the electrical connections to the rings. A schematic view of the PCB/plate assembly is shown in Figure 4-10. The PCB/plate assembly is shown in Figure 4-11.

Each of the two plates currently requires its own separate PCB, although future packaging designs may also address this issue. As a result of the two separate PCBs, capacitors must be hand-selected to ensure a very close matching of potentials between the two plates. Individual capacitors were measured with an HP 4280A (Hewlett Packard, Palo Alto, CA). A practical and achievable standard with this method for corresponding values of capacitance between the two PCBs has been to keep the percent difference between the two values under 0.5%. The equation for calculating this percent difference is

$$\left(\frac{|C_{n,PCB1} - C_{n,PCB2}|}{\frac{1}{2}(C_{n,PCB1} + C_{n,PCB2})} \right) * 100, \quad (4.1)$$

where n refers to a specific capacitor value within the voltage-divider circuit. A schematic view of the entire ion trap assembly with the two plates, two PCBs, detector, plate spacer, and a filament and lens assembly for creating ions is shown in Figure 4-12.

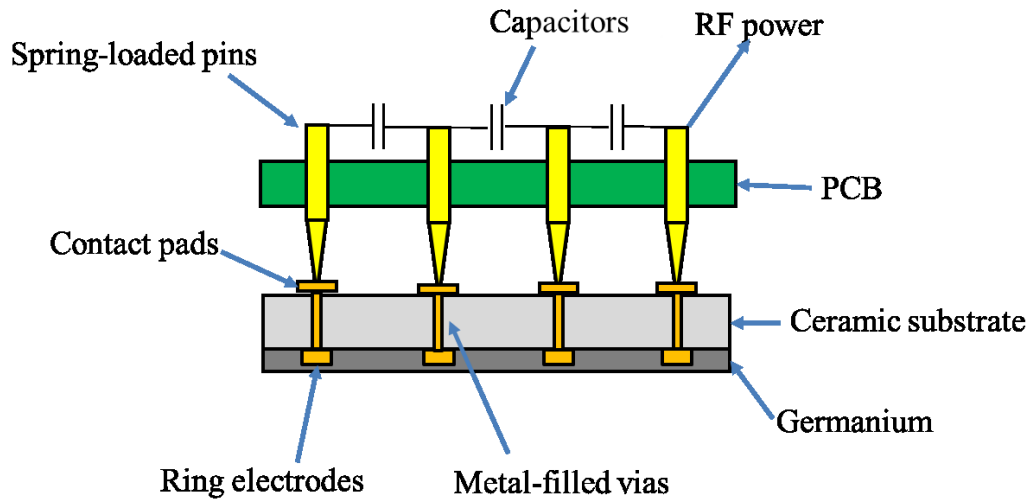


Figure 4-10: Schematic diagram illustrating the PCB/Plate Assembly

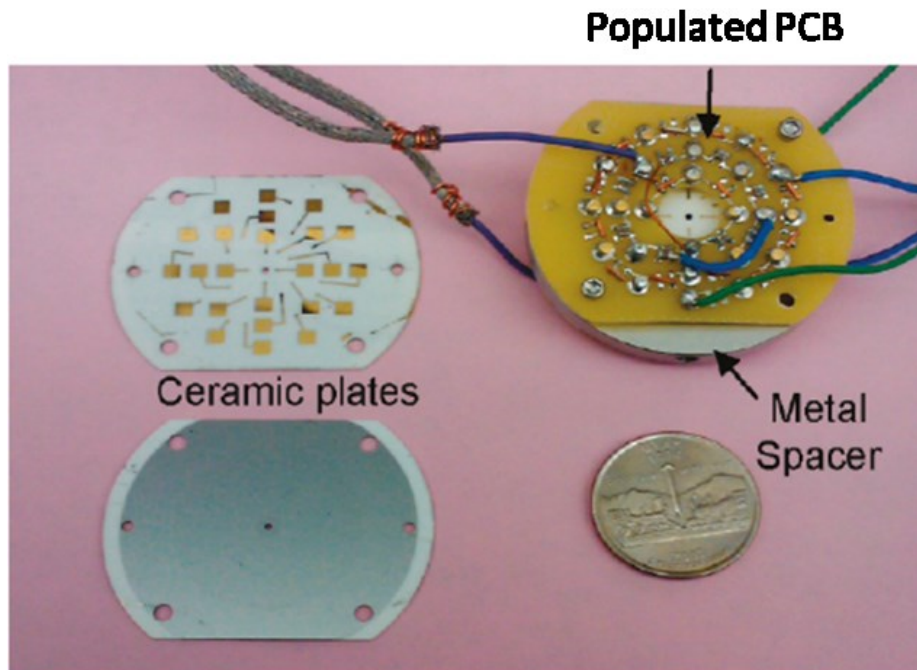


Figure 4-11: Back side metal patterning on ceramic, germanium covering the trapping side, and a populated PCB forming the plate/PCB assembly.

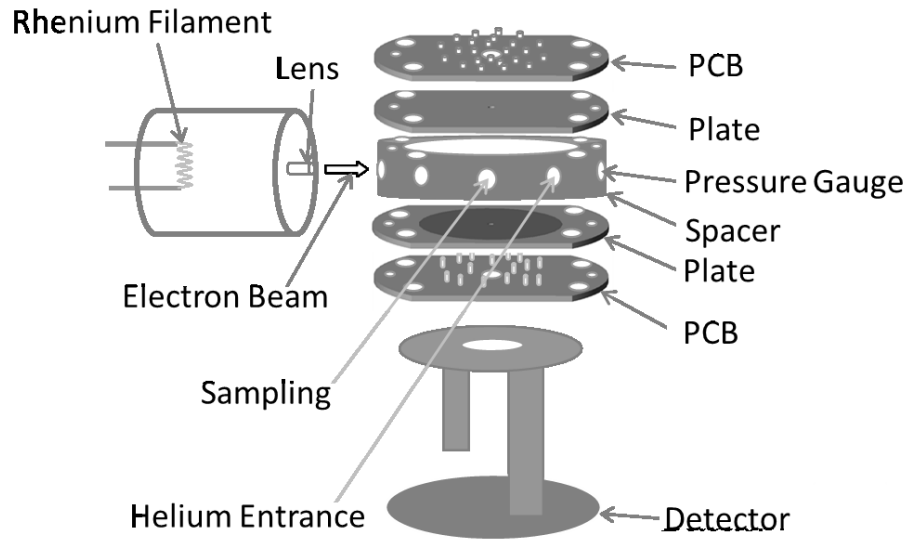


Figure 4-12: Schematic view of the entire trap assembly.

4.3 Multiple Trap Designs

One major benefit of the trap design shown in Figure 4-12 is the relative ease in reconfiguring and fabricating traps of various types and geometries. In some cases, an entirely different type of trap can be created with the same substrate by simply changing the values of the capacitors to place a different potential function over the span of the rings. These specific types of traps and their operation will be discussed in more detail later, but they are presented here in order to provide a point of reference for discussing the current microfabrication processing of the different designs. The newest designs of each trap type are all shown in Figure 4-13. Also shown in the figure is the patterned back side circuit pathways, where the large squares indicate the contact point for the PCB pogo pins, and each individual trace leads to vias for specific electrodes.

An additional plate design uses a Paul type electric field, where ions are stored over the center hole of the substrate. This substrate has 24 rings and a much smaller central hole. This

trap design has also been used to make a hybrid toroidal-Paul trap, known as the coaxial trap, which effectively creates two distinct traps with only one set of plates.

The first design developed that used rings was a toroidal trap, and all other versions of traps were derivatives from toroidal designs. The most recent toroidal design is a further advancement from the substrate shown in Figure 4-9. Originally, ions were ejected radially towards the large central hole, where afterwards they were drawn to the detector. In the latest toroidal design, ions are ejected axially towards the direction of the plates, utilizing a more efficient ion ejection direction. In place of a large central hole, slits are cut into the plate. These slits are located directly underneath the ion storage volume, simplifying and improving the ion ejection rate. This design included a second via for most rings as a redundant connection to improve process yield.

The final design is based on the RIT, a planar linear ion trap (PLIT). With this design, in place of rings, a series of parallel lines are patterned on either side of a slit that extends along the length of the plate. The slit provides the path for ion ejection. The lines are symmetric along the axis of the slit, and each symmetric line pair is electrically shorted together through the accompanying PCB design. The PLIT also incorporates a second via for each line to improve process yield. The two solid bars on either end of the plate are given a constant DC potential for axial confinement of ions with the trapping volume.

4.4 Microfabrication Technique

The general processing steps and challenges for all the designs of Figure 4-13 are similar, but variations in the recipe are required to produce an acceptable yield of the design. Appendix

B covers the detailed steps of these processes. The principles of the challenges and solutions are discussed here.

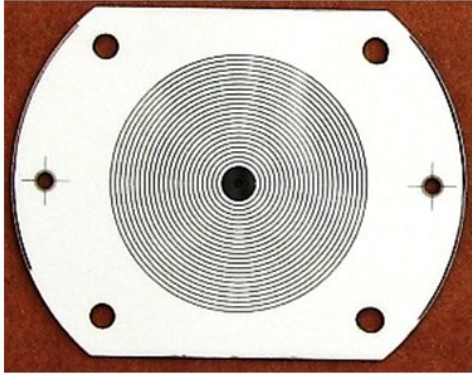
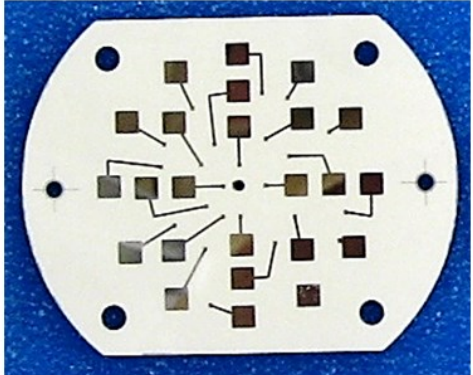
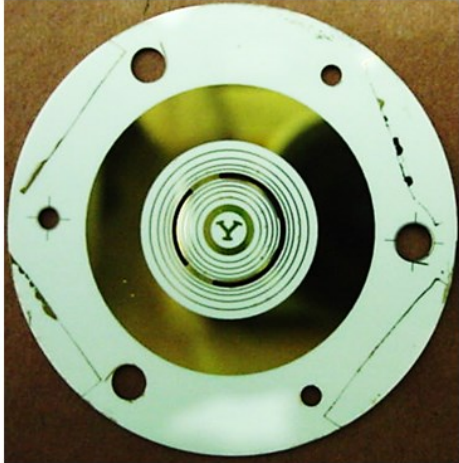
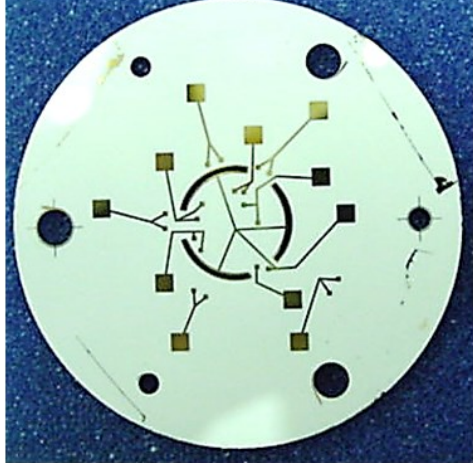
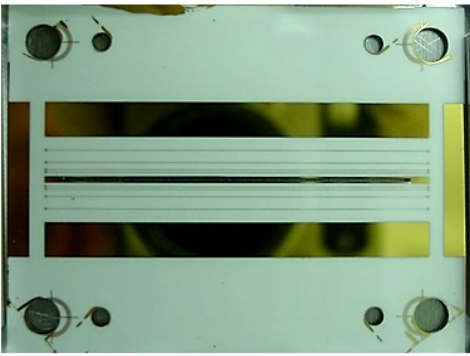
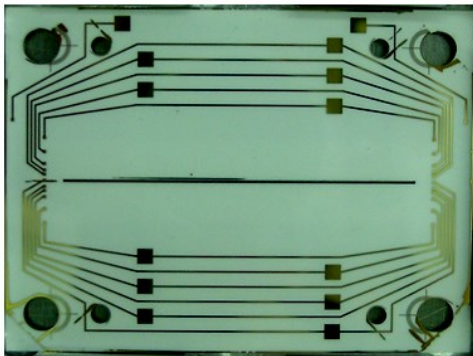
Trap type	Trap side	Back side
Paul/Coaxial	 <p>A photograph of the trap side of a Paul/Coaxial trap. It shows a circular electrode structure with concentric rings and four small circular features at the corners.</p>	 <p>A photograph of the back side of a Paul/Coaxial trap. It shows a complex network of thin lines and small square pads arranged in a circular pattern.</p>
Toroidal	 <p>A photograph of the trap side of a Toroidal trap. It features a central circular region with concentric rings and a small 'Y' shaped feature in the center, surrounded by four circular features at the corners.</p>	 <p>A photograph of the back side of a Toroidal trap. It shows a complex network of thin lines and small square pads arranged in a circular pattern, similar to the Paul/Coaxial design but with a central circular feature.</p>
Rectilinear	 <p>A photograph of the trap side of a Rectilinear trap. It shows a rectangular electrode structure with four circular features at the corners.</p>	 <p>A photograph of the back side of a Rectilinear trap. It shows a complex network of thin lines and small square pads arranged in a rectangular pattern.</p>

Figure 4-13: Most recent electrode layouts for four trap designs.

4.4.1 Prominent Challenges

Ceramic substrate can provide challenges to developing a consistent processing recipe. One of the primary challenges of working with ceramic is in the reduced adhesion of polished metals. Achieving high adhesion during photolithography steps on ceramic is not a trivial process [4]. This prevents the use of certain metals as part of a high-yield process, however, reasonable yield rates have been achieved in this work using careful process design.

Throughout much of the development of this process, gold on top of chrome was the metal of choice for the patterned electrodes. However, this selection of metal was never successful in producing a high success rate in the process. At best, batches achieved approximately a 50% success rate without metal flaking off the substrate. Often, this rate would be even lower. While gold is still occasionally used, the metal of choice now is aluminum, which has been shown to adhere much better to alumina [5, 6]. With aluminum, adhesion success is nearly 100%. Aluminum also provides a significantly cheaper material cost alternative to gold.

There have been no conclusive performance differences when comparing plates made with gold versus aluminum electrodes. The improved adhesion generally increases the lifetime of plates used in mass analyzers. The increased lifetime is due to both the metal patterning withstanding stress from handling and performing mass analyzer experiments and from the extended ability to recycle used plates. Used plates are recycled by etching away the metal pattern from the ceramic substrates and redoing the microfabrication process. The increase in recyclability is due to the vias being filled with a gold-based alloy. By foregoing gold-etchant acids and instead using aluminum etchants in the lithography process, the amount of etching of the vias with each processing step is decreased. An example of a via that has been over etched is

shown in Figure 4-14. When vias on a plate hit this over-etched point, the plate becomes useless for future patterning. Over-etched vias present problems in photoresist spinning, which will be explained after first discussing the fabrication process of the vias and how complications in that process can also produce overly deep vias.

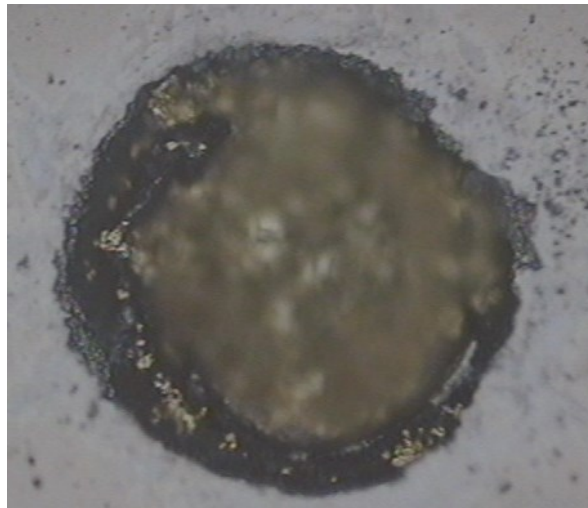


Figure 4-14: An over etched via, with the height being demonstrated by the difference in the depth of focus in the microscope.

The polishing processes for semiconductor substrates are well developed and produce extremely flat and smooth substrates. As of this writing, some companies are producing circuits with patterned feature sizes of 14-22 nm, requiring surface roughness better than 1 nm. This same degree of precision is not as easily available with ceramic substrates. The smoothness of the substrates used in this work is ± 25 nm. The polishing process, if overdone, can also cause the metal in the via connections to be too deep to allow patterning.

Due to the depth of the vias, even when not over polished, a very thick layer of metal is required. The metal layer must be thicker than 1 μm . If a thick layer of metal is not used, photoresist patterning and metal etching will not match the exposure mask. A deep via will

cause some photoresist shadowing and tearing within the inner edges of the via wall. This effect is depicted in Figure 4-15.

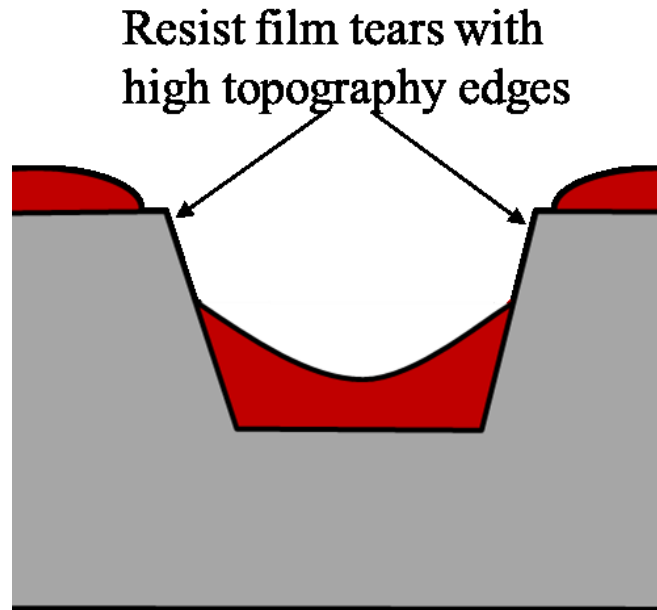


Figure 4-15: Photoresist application when spinning resist over a deep via. Figure adapted from “Lithographic Challenges and Solutions for 3D Interconnect,” in *Proc. IWLPAC*, 2008.

Furthermore, due to the roughness of the via, a thick layer of metal is required to provide a relatively smooth via bottom. Without a thick layer of metal, not only will resist tear along the edges of the via, but there also exists the possibility that resist at the bottom of the via will entirely fail to adhere to the metal. Examples of patterning processes that have suffered the effects of insufficient metal are shown in Figure 4-16.

Another significant challenge in process engineering comes from the shape of the substrates themselves. In the IML, photoresist application is done by a spinning process. The substrates in the ion trap designs have large holes or slits that create shadowing and streaking effects during photoresist application. Examples of this shadowing and streaking on the toroidal trap with slits is shown in Figure 4-17. Figure 4-18 demonstrates this effect with the PLIT. As

is shown in the figures, with many designs, the photoresist streaks and shadows appear right in locations of critical features. These imperfections appear on electrodes that are at the point of ion ejection, meaning that those imperfections will have the maximum potential for impacting ion trap performance.

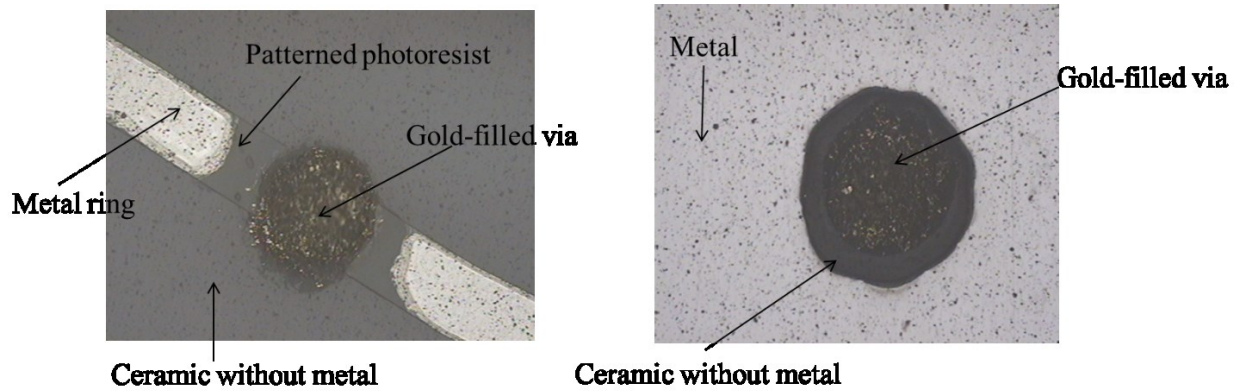


Figure 4-16: Vias that are not covered in a thick metal layer. (left) A ring electrode that was supposed to run over the via. The photoresist pattern is seen, but it has not adhered to the via bottom, allowing metal etchant to etch away the metal connection. (right) A via that should be completely covered in metal.

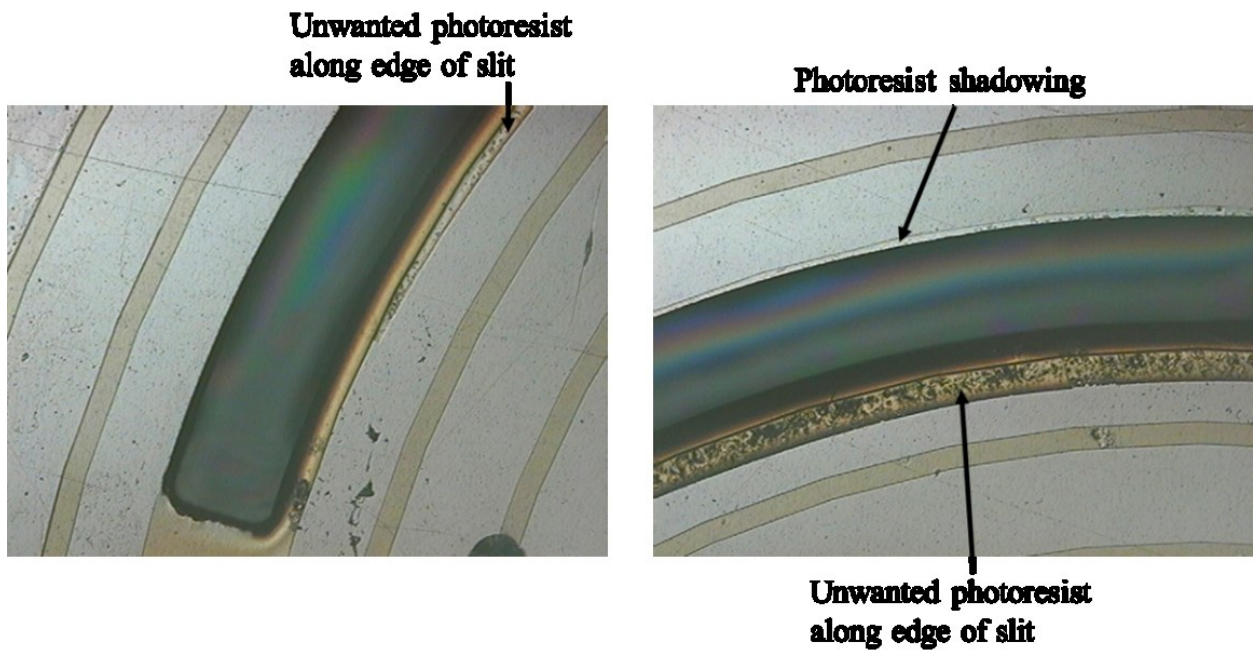


Figure 4-17: Photoresist streak and shadowing effects on the toroidal trap.

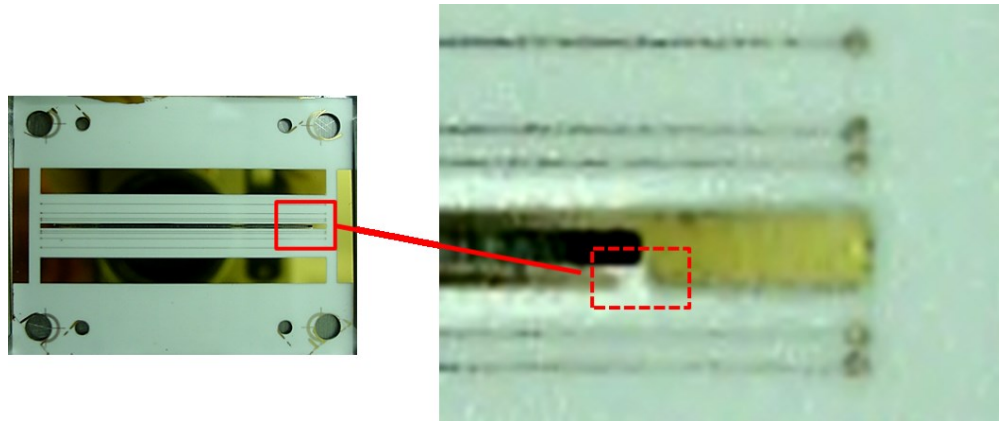


Figure 4-18: Photoresist shadowing in the PLIT. The electrode around the slit should be a solid bar.

Research has been done on applying photoresist over 3D structures [7-9], but most conclusions are that when applying photoresist to a substrate with tall features, methods other than spinning on resist are generally preferable. However, with careful feature design and proper spinning programs, reasonable spin-on photoresist application can be achieved even with unusual substrate topography [10-12]. This method is usually desirable since it allows the use of existing IML equipment. This method is feasible because feature size is quite large, with ring electrodes having a width of 100 μm and line electrodes having a width of 25 μm . This relatively large feature size both allows some steps to be taken in the electrode design process to alleviate fabrication difficulty, and also allows a realistic degree of tolerance in photoresist streaks and shadows. For example, with the PLIT, the slit extends further than is necessary to allow ion ejection. This means that imperfections at the edge of the slit in the surrounding electrode will have minimal impact. Furthermore, this electrode around the slit is made to be relatively wide to avoid a buildup of unwanted resist similar to what is seen with the toroidal trap in Figure 4-17.

Finally, these substrates involve double-sided patterning. Any process recipe must account for protecting the back side of the substrate during any lithography or etching. In

summary, every single step in the patterning of the metal electrodes must also meet the following criteria:

1. Maintain the surface cleanliness on both sides, or at least maintain the ability to nondestructively clean ceramic and metal surfaces.
2. Protect already patterned features (whether metal or photoresist only) on both sides.
3. Protect the ability to consistently pattern features on the back side.

4.4.2 Microfabrication Process

The entire fabrication process is summarized in Figure 4-19. The ceramic vendor (Hybrid-Tek, Clarksburg, NJ) shapes and polishes the substrate, and laser cuts (Questech, Garland, TX) all holes. The substrate is 0.635” thick alumina. All the vias are cut and filled with a gold-tungsten alloy by the vendor. The substrates arrive at the IML with the substrate shape, alignment holes, and filled vias as is shown in (b) of Figure 4-19.

All substrates, regardless of design, undergo an identical cleaning process upon receipt at the IML. This process involves a scrubbing with Alconox detergent, rinses in acetone and isopropanol, a dip in a hydrochloric acid and water mixture, a dip in an ammonium acetate and water mixture, and exposure to O₂ plasma to ensure removal of all organics from the surface. Before each cleaning step, the substrates are thoroughly rinsed in deionized water. At the end of the process, the plates are then placed in an oven for a dehydration bake.

In order to prepare the wafer for lithography processing in the IML, substrates are taped with Kapton tape (Kapton Tape, Torrance, CA), a tape with good adhesion that is relatively clean when removed, to a 4” silicon wafer, the standard IML processing size. Figure 4-20 shows a PLIT plate covered in gold prepared in this manner. After securing the plate onto a wafer,

photoresist is spun on. Photoresist spinning recipes vary depending on the trap design and are described in Appendix B. The planar Paul trap presents relatively few problems in uniform spinning of photoresist due to its relatively small central hole. All that is ordinarily required is to completely cover the substrate, including filling in holes, with photoresist before the spinning process. This amount of photoresist is used with all designs. Spinning resist on the toroidal and PLIT requires specialized spinning programs. These programs involve a combination of slower, gradual spins, followed by long high-speed spins.

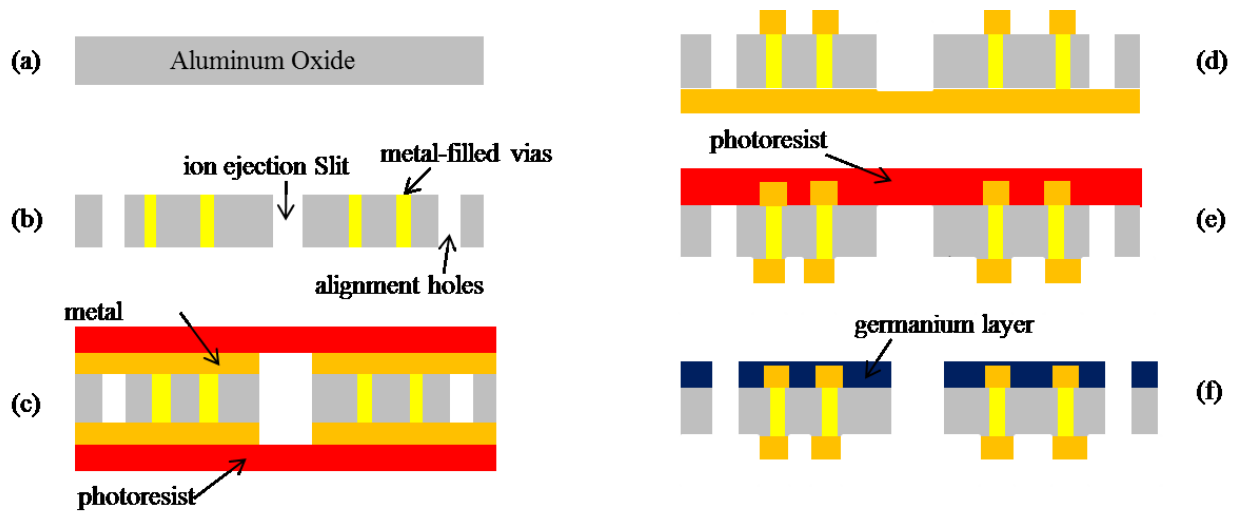


Figure 4-19: Cross-section view of the fabrication steps for planar electrode surfaces. (a) bare aluminum oxide substrate; (b) ejection slit, alignment holes, and metal-filled vias formed; (c) metal deposited on both sides of substrate, photoresist spun on top side and painted on bottom side; (d) top side patterned by photolithography and etching; (e) photoresist spun on bottom side, photoresist painted on already-patterned side, and bottom side patterned and etched; (f) germanium layer deposited over top of trapping side of substrate. Figure adapted from “A Lithographically Patterned Discrete Planar Electrode Linear Ion Trap Mass Spectrometer,” *J. Microelectromech. Sys.*, (in press).

Following application of photoresist, a soft-baked step is performed, and then resist is exposed under a chrome mask. Prior to developing the exposed resist pattern, photoresist is hand-painted to cover the back side of the ceramic and then the plate is soft-baked. This is done prior to developing the resist as resist developer is a mild aluminum etchant. Following resist development, the substrate is hard-baked, then placed in an etchant. To prepare the wafer for

patterning on the back side, the wafers are cleaned with an acetone and isopropanol rinse, and a short O₂ plasma descum. The backside patterning process follows all the same steps as patterning the front side. The substrate is completed with an electron beam deposition of 100 nm of germanium on the trapping electrode side.

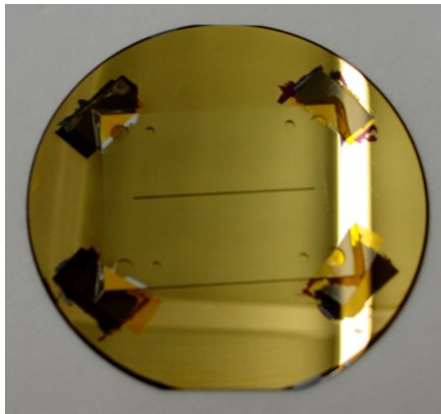


Figure 4-20: PLIT plate taped to 4" wafer for IML processing.

References

- [1] K. Bean, "Anisotropic etching of silicon," *IEEE T. on Electron Dev.*, vol. 25, no. 10, pp. 1185-1193, 1978.
- [2] D. E. Austin, D. Cruz and M. G. Blain, "Simulations of Ion Trapping in a Micrometer-Sized Cylindrical Ion Trap," *J. Am. Soc. Mass Spectrom.*, vol. 17, pp. 430-441, 2006.
- [3] B. Ealet, B. Robrieux and E. Gillet, "A surface analytical study of the formation and adhesion of chromium films on alumina," *J. of Adhes. Sci. Technol.*, vol. 6, no. 11, pp. 1221-1231, 1992.
- [4] W. H. Yoo, B. G. Chang and Y. S. Kim, "Method for forming electrode pattern of ceramic substrate, U. S. Patent 8198198," 2012.
- [5] P. Alemany, R. S. Boorse, J. M. Burlitch and R. Hoffman, "Metal-Ceramic Adhesion: Quantum Mechanical Modeling of Transition Metal-Al₂O₃ Interfaces," *J. Phys. Chem.*, vol. 97, pp. 8464-8475, 1993.

- [6] H. -T. Li, L. -F. Chen, X. Yuan, W. -W. Zhang, J. R. Smith and A. G. Evans, "Interfacial Stoichiometry and Adhesion at Metal/a-Al₂O₃ Interfaces," *J. Am. Ceram. Soc.*, vol. 94, pp. S154-S159, 2011.
- [7] K. Cooper, K. Cook, B. Whitney, D. Toennies, R. Zoberbier, K. J. Kramer, K. Weilermann and M. Jacobs, "Lithographic Challenges and Solutions for 3D Interconnect," in *Proc. IWLPC*, 2008.
- [8] K. Cooper, C. Hamel, B. Whitney, K. Weilermann, K. J. Kramer, Y. Zhao and H. Gentile, "Conformal Photoresist Coatings for High Aspect Ratio Features," in *Proc. IWLPC*, 2007.
- [9] N. P. Pham, E. Boeallaard, J. N. Burhartz and P. M. Sarro, "Photoresist Coating Methods for the Integration of Novel 3-D RF Microstructures," *J. Microelectromech. S.*, vol. 13, no. 3, pp. 491-499, 2004.
- [10] V. G. Kutchoukow, J. R. Mollinger and A. Bossche, "Novel method for spinning of photoresist on wafers with through-hole," in *Proc. Euroensors XIII*, The Hague, The Netherlands, 1999.
- [11] N. P. Pham, P. M. Sarro and J. N. Burghartz, "IC-compatible process for pattern transfer in deep wells for integration of RF components," in *Proc. SPIE*, vol. 4174, Santa Clara, CA, 2000.
- [12] M. Parodi, T. Batchelder, P. Haaland and J. McKibben, "Spin coating and alternative techniques for flat panel displays," *Semiconductor Int.*, vol. 19, no. 1, pp. 101-106, 1996.

5 THE TOROIDAL, PAUL, AND COAXIAL TRAPS

5.1 The Toroidal Trap

There have been two different types of toroidal traps. The first design ejected ions along the radial axis of the toroidal ion storage region, while the second design ejected ions along the z axis of the storage region. Both designs used the ceramic substrates and fabrication processes described in Chapter 4. All toroidal designs used two facing patterned electrode surfaces with a spacing of 5.06 mm.

5.1.1 Radial Ejection

In experiments, sample analytes were ionized directly within the trapping volume. Both sample and helium were injected into the chamber through leak valves. The ionization of the sample was done with an electron gun. The electron gun consisted of a rhenium filament with 1.7 A applied current. The gun was gated by changing the bias on the filament from -70 to +120 V. Best results were obtained when the ionization time was between 30-45 ms.

The RF trapping potential was applied using custom-built electronics. The frequency of the trapping field was 1.9 MHz, with an amplitude up to 650 V_{p-p} . Ejection was done by way of applying an additional AC signal for resonant ejection. The resonant ejection signal swept from 50 kHz to 600 kHz (33250A, Agilent Technologies, Santa Clara, CA). The time of the frequency sweep was 100 ms. Figure 5-1 illustrates the various steps of ion creation, ion storage, and ion ejection into a detector. Figure 5-2 shows the timing of the various phases of the mass

analysis experiment, the RF timing, resonant signal timing, resonant frequency, and the gate voltage. The ion trap was controlled by a program using Labview 7.1 through a BNC-2110 data acquisition board (National Instruments, Austin, TX).

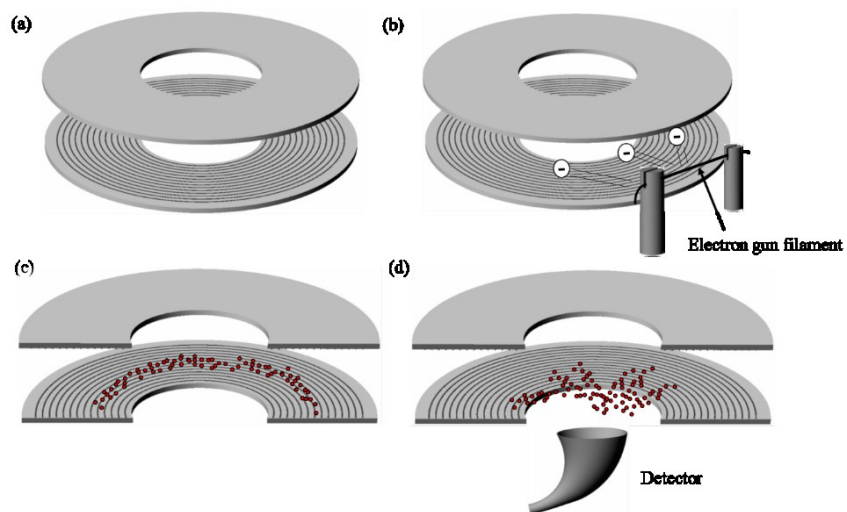


Figure 5-1: Illustrated steps of mass analysis in the toroidal trap. (a) RF applied on plates, (b) sample ionized by way of electron gun, (c) ions stored in a toroidal region, (d) ions swept into detector by application of resonant ejection AC signal. Figure adapted from “Halo Ion Trap Mass Spectrometer,” *Anal. Chem.* 79, pp. 2927-2932, 2007.

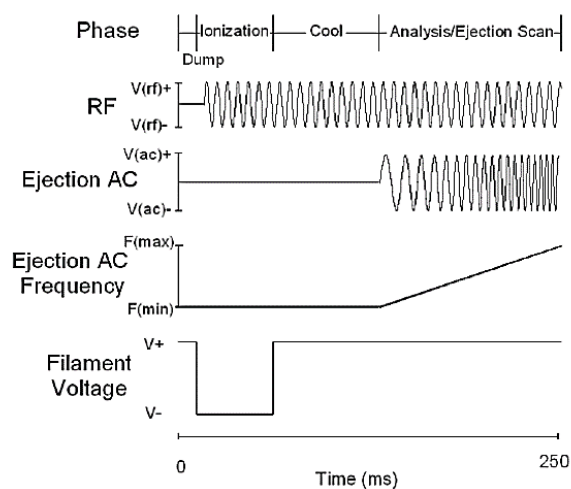


Figure 5-2: Timing of control signals in the toroidal ion trap. Figure from “Halo Ion Trap Mass Spectrometer,” *Anal. Chem.* 79, pp. 2927-2932, 2007.

Mass analysis experiments were performed in a custom-built vacuum chamber pumped by a turbo pump (Pfeiffer, model TMH 520-020, Asslar, Germany). All sample pressures were in the low 10^{-5} torr range. Helium pressure for collisional cooling was in the high 10^{-4} to the low 10^{-3} torr range.

5.1.1.1 Field Design

The profile of the electric field, when using a fixed spacing between the plates, is determined by the magnitude of RF potential applied to each individual electrode. The electrode pattern is shown in Figure 5-3. A germanium layer evaporated over the rings helps to smooth the voltage profile on the surface of the plate. This potential function was calculated using SIMION 7. The germanium layer causes voltage on the ceramic to change between adjacent rings at a rate proportional to $1/r$, where r is the radius from the center of the plate. The procedure for calculations for this trap was similar to that described in Appendix C.

Figure 5-4 illustrates the potential function for this configuration [1]. The potential is only described along the radial axis. The direction of ejection is the most relevant when determining the behavior of an ion trap. The electric field, the derivative of the potential function, is also depicted in the figure.

As already discussed in Chapter 2, a purely quadrupolar field that satisfies the Laplace equation is not possible with a toroidal trap. This limitation restrained the ability to do a complete mathematical analysis of this field and its higher order multipole components. However, this design is still useful to investigate the effects of higher order fields by subtle changes in the potentials applied to the specific rings. In this trap, the octopole term (A_4/A_2) was calculated to be 24.3%, and the dodecapole term (A_6/A_2) was 1.6%.

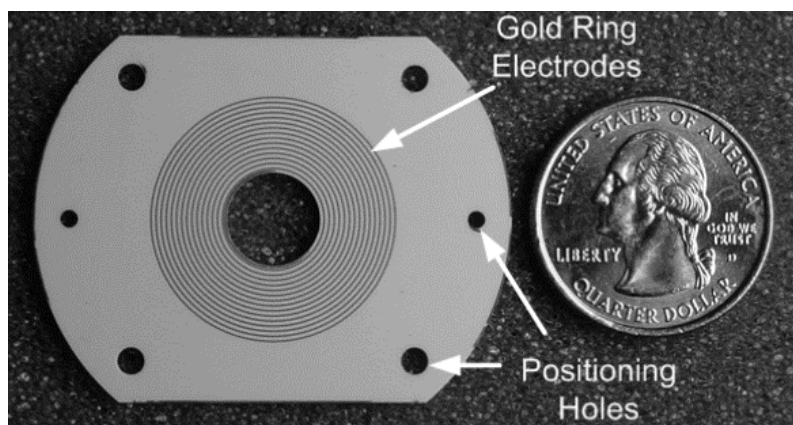


Figure 5-3: The toroidal trap for radial ion ejection. Figure from "Halo Ion Trap Mass Spectrometer," *Anal. Chem.*, 79, pp. 2927-2932, 2007.

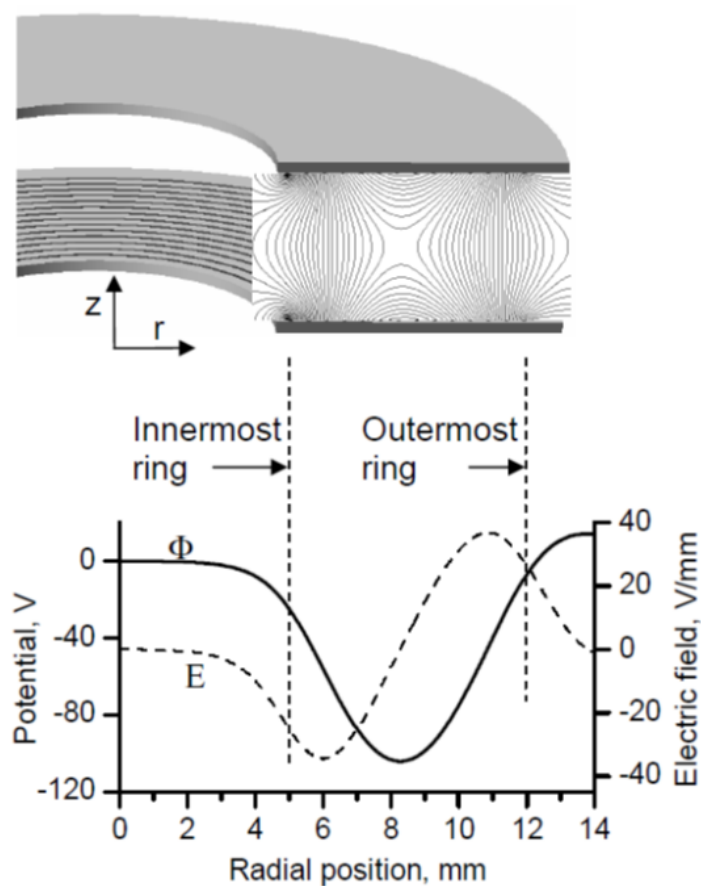


Figure 5-4: Potential function and electric field of the radial-ejection toroidal trap. Figure from "Halo Ion Trap Mass Spectrometer," *Anal. Chem.* 79, 2927-2932, 2007.

5.1.1.2 Results

Figure 5-5 illustrates spectra recorded from this design. The compounds analyzed were dichloromethane and toluene. The spectra shown is the average of four independent experiments. The expected peaks of masses in the m/z range shown on the figure are all present. With dichloromethane, the full width half maximum (FWHM) of the peak at m/z 49 is 0.64, but the heavier mass peaks shown are not clearly resolved. With toluene, peaks are seen in the expected m/z ranges. However, there should be separate peaks at m/z 91 and m/z 92, which are not resolved.

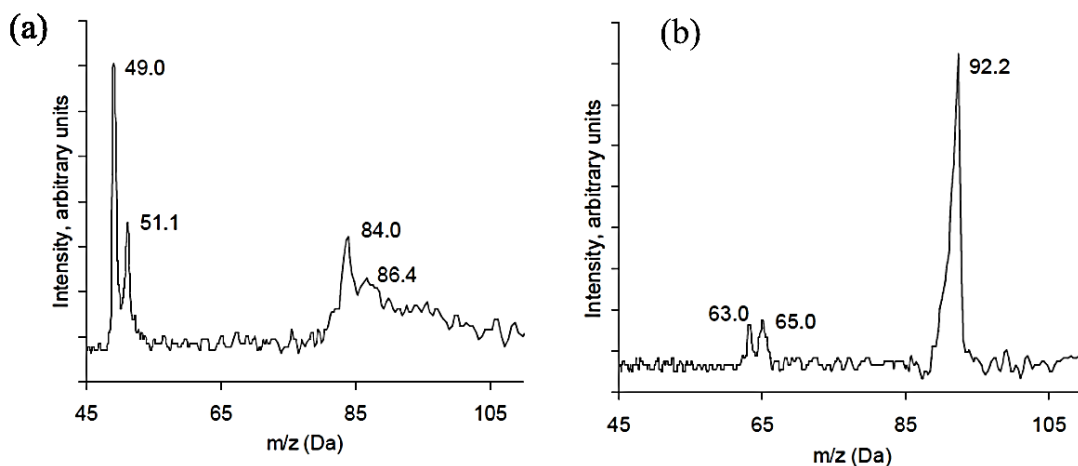


Figure 5-5: Results from the radial-ejection toroidal trap. (a) dichloromethane, (b) toluene. Figure adapted from “Halo Ion Trap Mass Spectrometer,” *Anal. Chem.*, 79, pp. 2927-2932, 2007.

Simulations done with this design showed that only a resonant frequency sweep would be effective in ejecting ions into the center hole of the plate. Attempting to eject ions by ramping the RF amplitude resulted in ions running into the plates themselves. The mass range was also limited to m/z values of less than 112. Different values of RF amplitude and frequency could be used to adjust the mass range of the system.

5.1.2. Axial Ejection

An alternative to the radial-ejection toroidal trap was the axial-ejection ion trap [2]. The electrode structure used in this experiment is shown in Figure 5-6. This design was to allow a more efficient ion ejection method than radial ejection. With radial ejection, ions had to be ejected to the center hole on the plate, but also had to curve downward towards the detector before running into the far side of the plate/PCB assembly. Using axial ejection, a direct ejection path to the detector could be used. The difference in these two methods is shown in Figure 5-7.

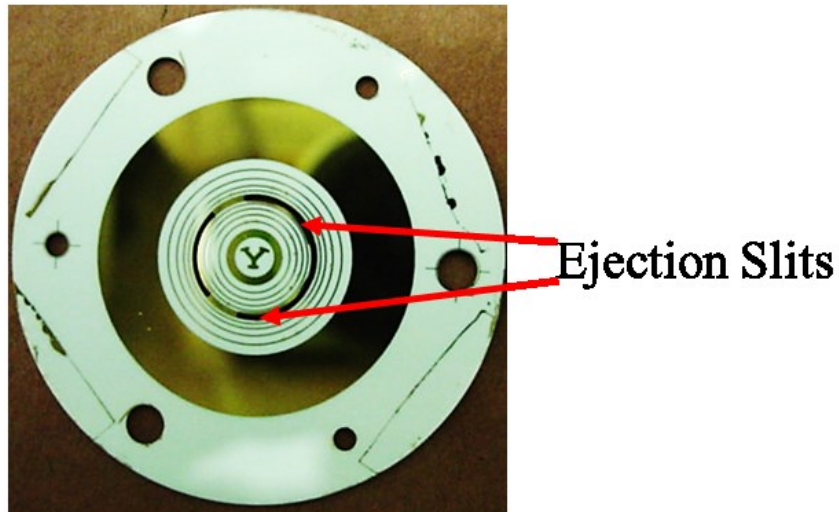


Figure 5-6: The axial-ejection toroidal trap.

The experimental setup was nearly identical between this system and the previous system. The RF power supply had an amplitude of $900 V_{p-p}$ and a frequency of 1.7 MHz. The resonant ejection signal had an amplitude of $10 V_{p-p}$. To further increase ejection efficiency, the resonant ejection signal was applied to both plates, but in opposite phase of each other. This signal was applied to the ring that lay over the top of the slits. The detector was set a -1.9 kV to collect the positive ions ejected from the trap.

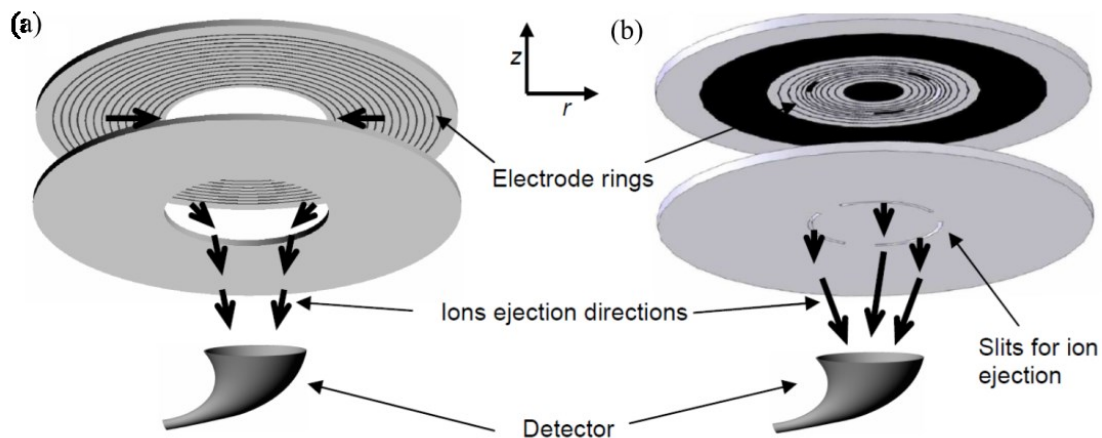


Figure 5-7: The two methods for ion ejection used in the toroidal ion trap. (a) Radial ejection, (b) axial ejection. Figure from "Performance of a Halo Ion Trap Mass Analyzer with Exit Slits for Axial Ejection," *J. Am. Soc. Mass Spectrom.* 22, pp. 369-378, 2011.

5.1.2.1 Field Design

The principles of the design of the electric field were similar to that of the radial-ejection trap. The lowest potential was set on the 6th ring, or the ring where the ejection slit is located. This potential function helps to keep ions located over the slit. The electrode layout is described in Table 5.1. The potential function was calculated moving along the z axis of the trapping region. Tests were made with varying octopole values (A_4/A_2) of 1%, 3%, 5%, and 7%, with a constant A_6/A_2 value of -50%.

Table 5.1: The electrode layout of the axial-ejection toroidal ion trap.

Ring number	Inner radius (mm)	Outer radius (mm)
1	0.0	2.8
2	3.5	3.6
3	4.2	4.3
4	4.8	4.9
5	5.3	5.4
6	5.7	6.3
7	6.6	6.7
8	7.1	7.2
9	7.8	7.9
10	8.7	8.8
11	9.8	16.0

5.1.2.2 Results

Experiments on the effect of different values of octopole percent are shown in Figure 5-8. The compound measured in this experiment was benzene. The strongest ion signal was recorded using a resonant ejection frequency sweep, the same method used in the radial-ejection trap. The spectra shown are the average of ten separate experiments.

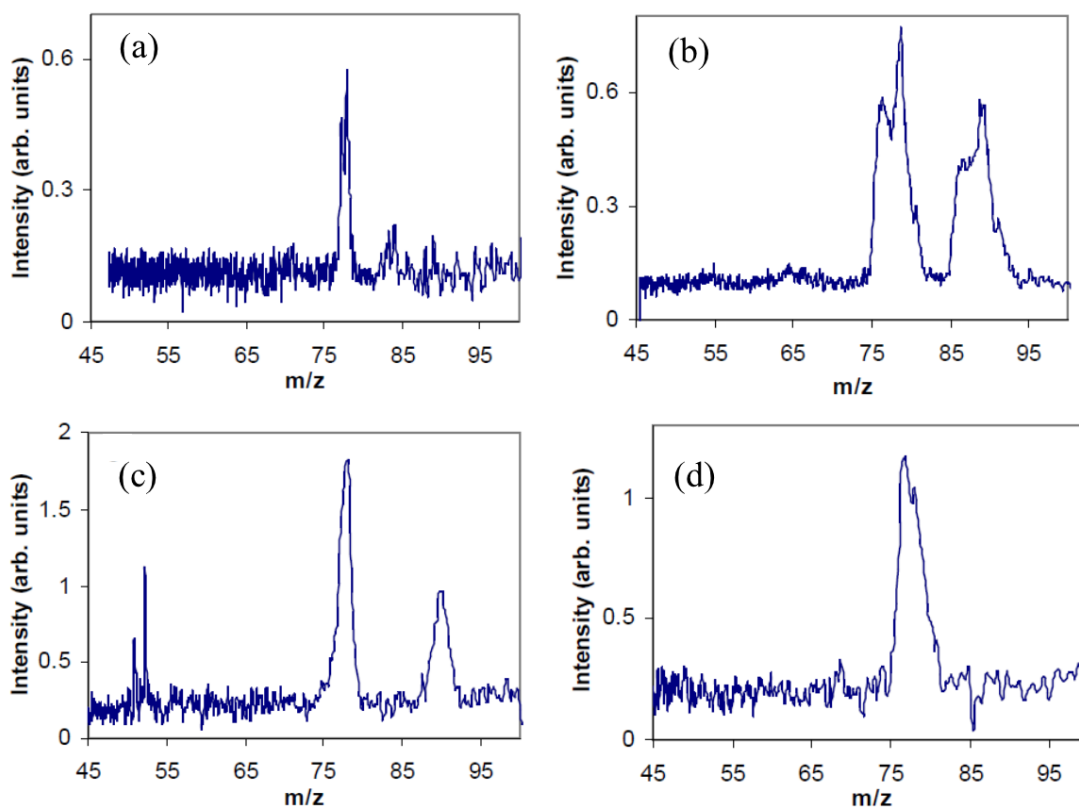


Figure 5-8: Benzene spectra using different values of octopole. (a) 1%, (b) 3%, (c) 5%, (d) 7%. Figure from "Performance of a Halo Ion Trap Mass Analyzer with Exit Slits for Axial Ejection," *J. Am. Soc. Mass Spectrom.*, 22, pp. 369-378, 2011.

For the 1% configuration, the dominant peaks in the figure at m/z 77 and 78 are a FWHM of 1.2 mass units. For the 3% configuration, all peaks were poorly resolved. An additional peak at m/z 90 appears as the result of an ion-molecule reaction. For the 5% octopole configuration,

ion fragments at m/z 51 and 52 appeared with a FWHM of 0.19. The 7% octopole configuration had the worst performance of all.

Figure 5-9 shows the spectrum for dichloromethane with a 5% octopole field. The overall performance was superior in some aspects to that of the radial-ejection toroidal trap. The FWHM of the m/z 49 was 0.18. However, resolution was poor at the higher m/z values.

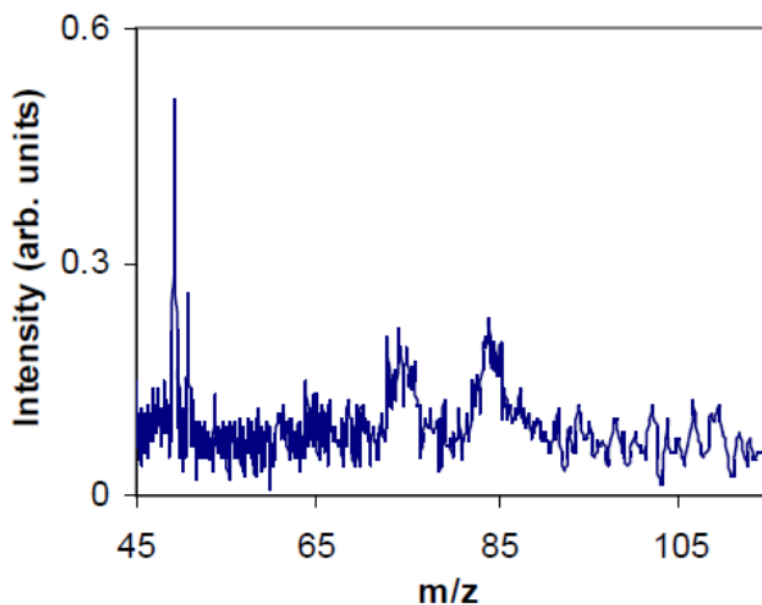


Figure 5-9: A measured dichloromethane spectrum with 5% octopole. Figure from "Performance of a Halo Ion Trap Mass Analyzer with Exit Slits for Axial Ejection," *J. Am. Soc. Mass Spectrom.*, 22, pp. 369-378, 2011.

The reason for the poor resolution at higher masses is due to the relative potential well depth for each m/z value. The heavier values are trapped in a shallower well and are more easily ejected from the resonant ejection signal. This signifies a wider range of frequencies that will eject ions at larger masses. Another potential problem was that the microfabrication process was not reproducible with respect to the ring immediately over the slit, as described in Chapter 4. Imperfections in these electrodes, along with any asymmetry in the capacitive voltage-divider

circuit on the PCB will slightly move the actual center of the trapping region, impeding the clear ejection path for ions to travel through the slits to the detector.

One significant note in performance is the relative ion intensity seen with the axial-ejection trap. The ejection area of the slit was 17.6% as large as the ejection hole of the radial-ejection trap. However, the relative ion intensity with the axial trap signal was equivalent to that of the radial-ejection trap, signifying a more efficient ion ejection mechanism.

5.2 The Planar Paul Trap

The planar Paul trap design is realized by using an electrode pattern that consists of 24 rings [3]. The central hole of this design is small compared to that of the toroidal design. Ions are stored over the center of the plate, over the central hole, which provides a path for ion ejection. Rings 2-24 are 100 μm wide. The first ring has a radius of 1.3 mm to accommodate the drilling of the central hole. The plate used for this design is shown in Figure 5-10. The plates were spaced 6.0 mm apart.

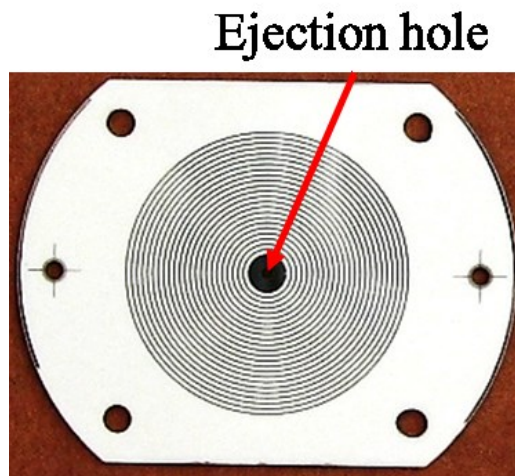


Figure 5-10: The planar Paul trap electrode pattern.

The experimental setup was similar to that of the toroidal traps. A 6-mm stainless steel spacer was mounted between the trapping plates. Holes in the spacer were used as access to the trap for the electron gun, sample vapor, helium gas, and a Teflon tube leading to a pirani gauge (Kurt J. Lesker, Clairton, CA). An RF signal with a frequency of 1.26 MHz and variable amplitude up to 738 V_{0-p} (PSRF-100, Ar dara Technologies, North Huntingdon, PA) was applied to the capacitor network on the PCB boards, and the spacer was grounded during ion ejection. For resonance ejection, a supplementary low-voltage AC signal, generated using two 30 MHz synthesized function generators (DS345, Stanford Research Systems, Sunnyvale, CA) with a 180° phase difference, and amplified to 3.5 V_{0-p} by a custom-made amplifier, was applied between the trapping plates to provide a dipole field for resonant ion ejection during the RF scan. The amplified supplementary AC signals were applied to the innermost ring on each plate, using a simple filter circuit to isolate the supplementary AC from the main RF signals. The applied frequency of the AC signal was 290 kHz. The electron gun was gated with an Einzel lens type assembly (Torion Technologies, American Fork, UT).

The timing for the control signals of this trap are shown in Figure 5-11. The phases and timing for ionization, RF trapping, and ejection are included. First, the RF voltage was turned off to clear previously trapped ions out of the trap. The RF then was turned back on, along with opening an electron gun gate, allowing sample to be ionized and trapped in the trapping volume. The electron gun gate was then closed, allowing the ionized and trapped sample to collisionally cool with background helium gas. The ejection AC was then turned on, and the RF amplitude was ramped up. As the RF amplitude was ramped, the secular frequency, or β value from the stability diagram, of the trapped ions would also change. When the secular frequency of any ion matched the applied supplementary AC frequency, that ion was resonantly ejected from the trap.

Because ejection voltage was ramped from lower to higher voltages, ions were ejected in order of increasing m/z out of the trap. After an ion was ejected through the hole in the trapping plates, it continued toward the detector. Ejected ions were detected using an ETP electron multiplier detector (SGE Analytical Science, Austin, TX), with a conversion dynode operated at -4000 V to attract and collect positively charged ions. The signal was amplified using a current amplifier (Model 427, Keithley Instruments, Cleveland, OH) and recorded using a digital oscilloscope (WaveRunner 6000A, LeCroy, Chestnut Ridge, NY).

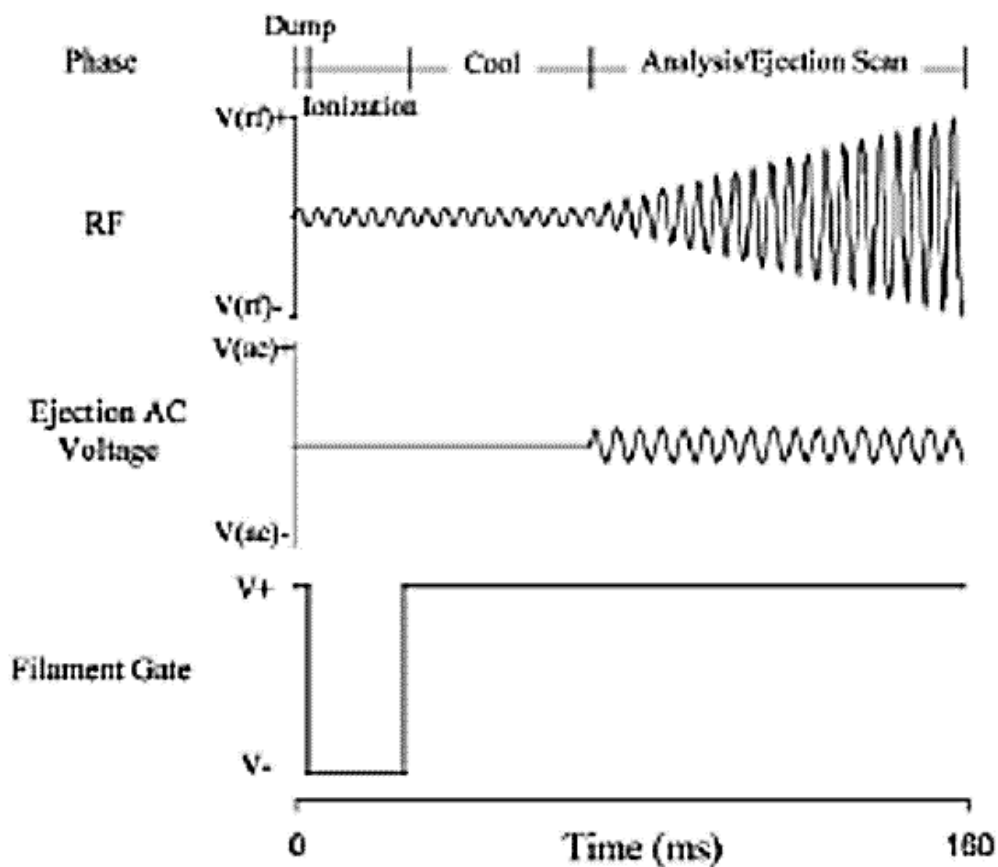


Figure 5-11: The timing of signals controlling the Paul trap. Figure from “Paul Trap Mass Analyzer Consisting of Opposing Microfabricated Electrode Plates,” *Anal. Chem.*, 81, pp. 5241-5248, 2009.

5.2.1 Field Design

The equation describing the potential function of the Paul trap, described up to the 6th order, will take the form [4]

$$\phi(r, z, t) = (U + V\cos\Omega t) \left[A_2 \frac{r^2 - 2z^2}{2r_0^2} + A_4 \frac{3r^4 - 24r^2z^2 + 8z^4}{8r_0^4} + A_6 \frac{5r^6 - 90r^4z^2 + 120r^2z^4 - 16z^6}{16r_0^6} \right]. \quad (5.1)$$

The relevant trapping volume can be approximated to $r = 0$. Furthermore, it is more useful to express this equation in terms of z_0 , which represents half the value of the plate spacing and the direction of ion ejection.

$$\phi(z, t)_{r=0} = (U + V\cos\Omega t) \left[A_2 \left(\frac{z}{z_0} \right)^2 + A_4 \left(\frac{z}{z_0} \right)^2 + A_6 \left(\frac{z}{z_0} \right)^2 + \dots \right]. \quad (5.2)$$

For convenience, the signs of some of the terms in Equation 5.2 have been switched so that the dependence of all terms on z have the same sign. This is done so that all A_n terms will have the same sign as the multipole components with respect to z .

Each electrode ring will have an independent contribution to this potential function. Because of the superposition principle, the total potential function is a linear summation of the potential contributions from each ring. This, in turn, implies that each total A_n term of the total potential function is a summation of the A_n terms from the potential functions of each individual ring. One implication of this is that rings of certain radii will strongly affect specific higher order multipole terms (i.e. octopole, dodecapole, etc.) more strongly than other rings, allowing the specific tuning of electric fields. To achieve optimized mass analyzer performance, specific values of higher order multipoles must be part of the trap potential function.

5.2.2 Results

An extensive study has been performed with the Paul trap to find the optimized multipole values. Figure 5-12 demonstrates the results of testing various combinations of multipole components. The relative amounts of resolution of the mass peaks and peak strength are shown in the figure. The compound studied is acetone, and the peaks studied had m/z values of 43 and 58. The electric fields were calculated following the procedure outlined in Appendix C.

Reported simulations have indicated that a higher dipole field (the resonant ejection signal) is required to resonantly eject ions from a trap with a small positive octopole than from a trap with a pure quadrupole field [5]. In fact, when an octopole is present, a threshold voltage exists, below which ions cannot be resonantly ejected. The peak intensity and the signal to noise ratio (SNR) depicted in Figure 5-12 is indicative of this phenomenon. As a result of the threshold ejection voltage, resolution can be improved. With a required threshold voltage, it is more difficult for ions to fall out of the trap due to random fluctuations in ion motion and direction as approximate resonant ejection conditions are satisfied. This results in a narrower set of conditions and time during a mass scan when ions of a specific m/z value are ejected from the trap, in turn leading to more resolved peaks.

Figure 5-13 is a similar study to that done in Figure 5-12. This experiment does not test the peak strength, but compares a forward mass scan with a reverse mass scan. A reverse mass scan is done by starting from a high RF amplitude and ramping down with a constant resonant ejection AC signal also applied.

In the case of a positive octopole (Figure 5-13a) both SNR and resolution drop off significantly for the lowest dipole amplitudes. A similar trend is observed, although not as strongly, for a positive dodecapole (Figure 5-13d). For the other field combinations (Figure 5-

13b, c, and e) the highest resolution is achieved using the smallest amplitude of applied dipole, and SNR does not appear to drop off significantly at the lowest dipole amplitudes. Unfortunately, the trend is not well defined from these data. Nevertheless, these results are in general agreement with reported simulations [5]. In all cases, both resolution and SNR decrease with higher dipole amplitude, although with 4% octopole the dipole amplitude must be higher than in the other cases for this trend to appear. Except at the minimum applied dipole signal, the dodecapole appears to have little effect on the resolution or SNR.

Generally, mass resolution in an ion trap increases with decreasing RF scan speed [6-9]. The effect of scan speed on the performance of the planar Paul trap was investigated within the range of 665–220 Th/s, or units of m/z per second. Figure 5-13 shows mass resolution as a function of scan speed for several octopole/dodecapole configurations. Ions used include the m/z 84 and 86 fragments of dichloromethane and the m/z 130 and 132 of trichloroethylene. Both forward and reverse scan modes were carried out for each speed and each field. Little difference was observed in forward scans between +2 and –2% octopole, holding the dodecapole constant at –4%. However, with the reverse scan, the negative octopole had a notably higher resolution than the positive octopole, and higher than the forward scan with the same field. With the octopole fixed at 0% and the dodecapole varied from –4% to +4%, no significant difference existed between forward and reverse scans, or between positive and negative dodecapole. Resolution increased slightly with reduced scan speed for all field combinations.

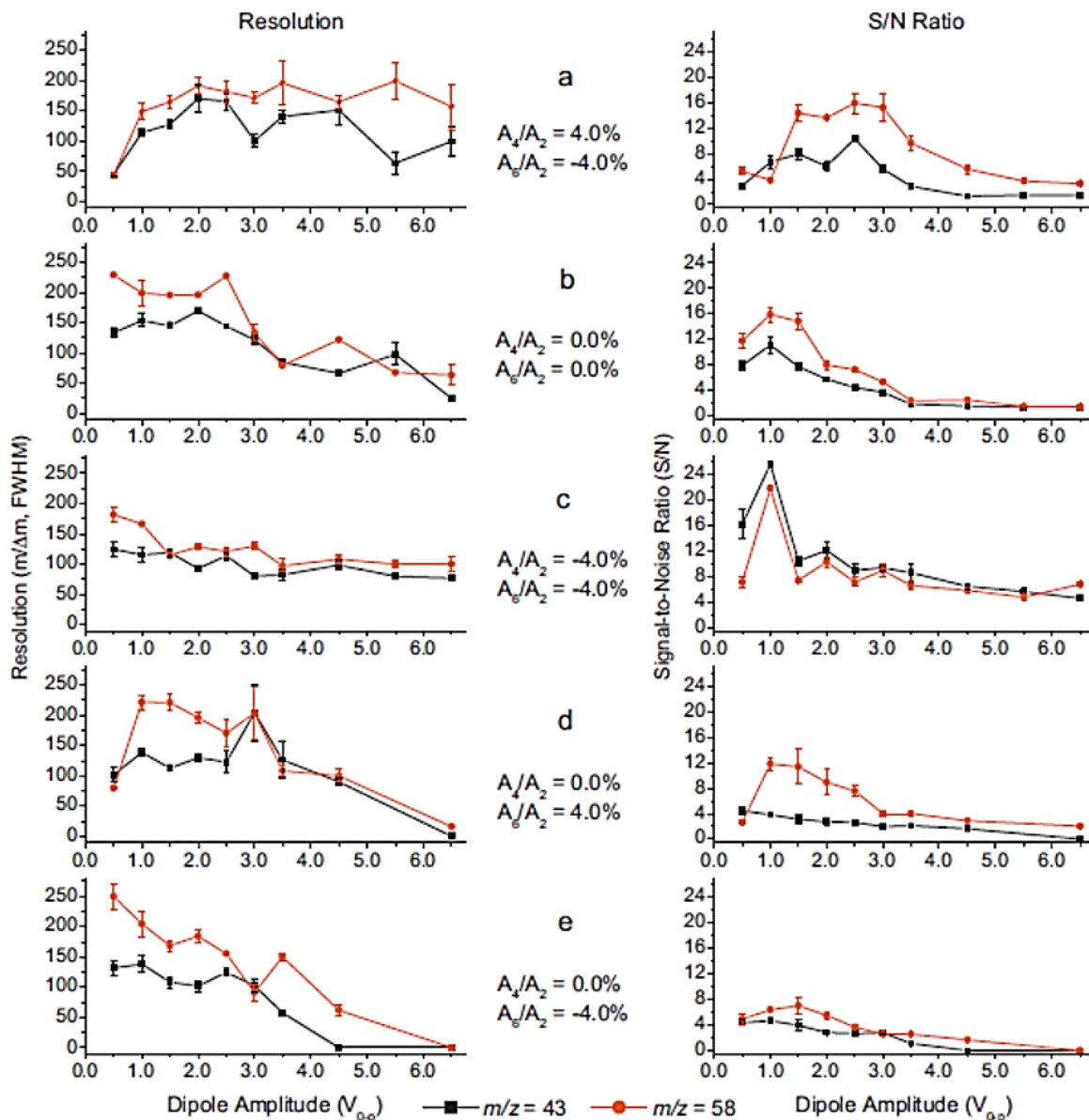


Figure 5-12: Comparison of resolution ($m/\Delta m$, FWHM) and signal-to-noise (S/N) ratio for the m/z 43 and 58 ions of acetone using electric fields with different octopole/dodecapole combinations. These values are from individual spectra. Each data point represents the average of three measurements. Sample pressure: 10⁻³ Torr; ionization time: 4.0 ms; ac frequency: 345 kHz. Figure from “Effects of higher-order multipoles on the performance of a two-plate quadrupole ion trap mass analyzer,” *Int. J. Mass Spectrom.*, 299, pp 151-157, 2011.

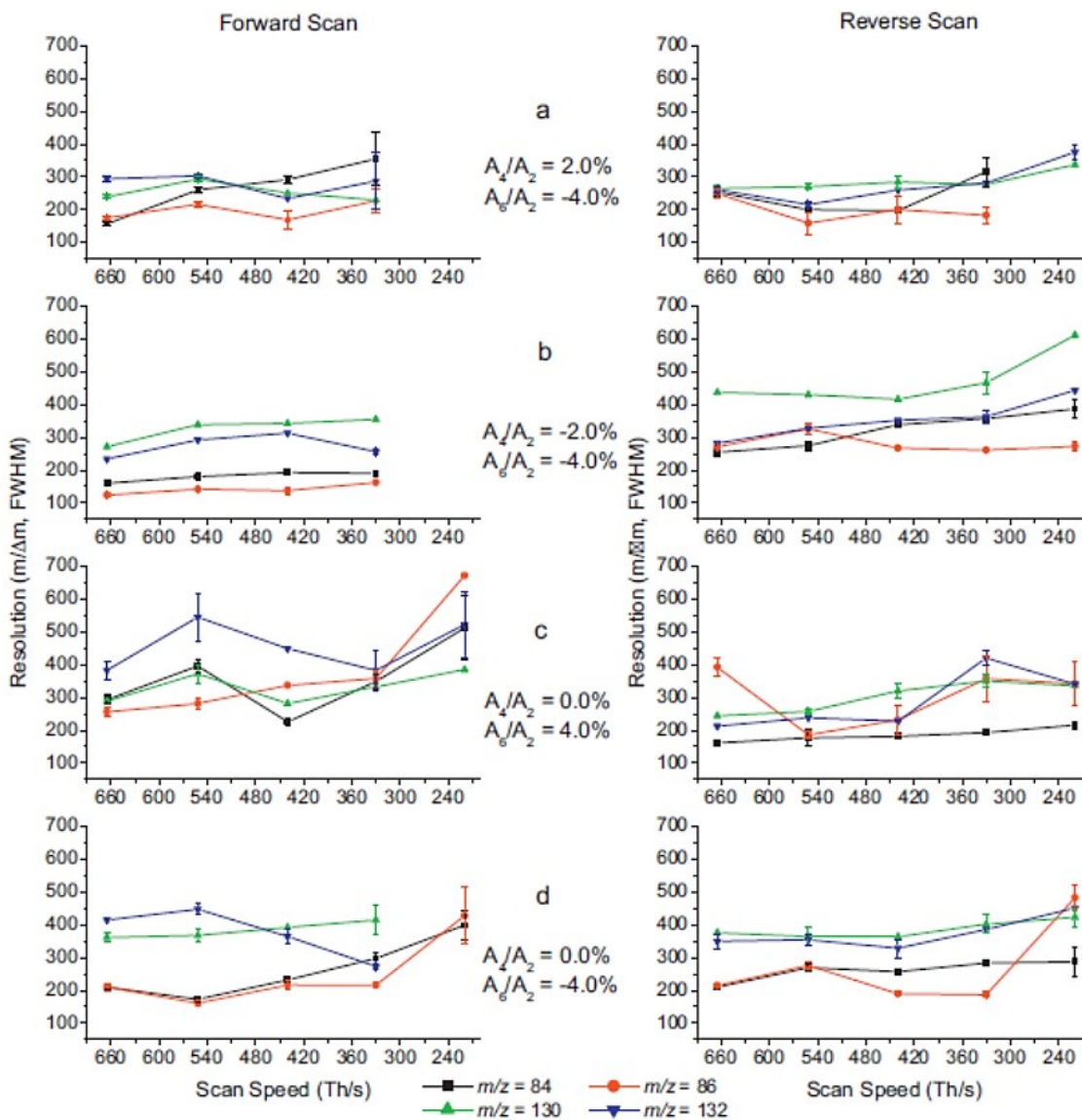


Figure 5-13: Comparison of resolution ($m/\Delta m$, FWHM) for the m/z 84 and 86 ions of dichloromethane and the m/z 130 and 132 ions of trichloroethylene under the electric fields with different octopole/dodecapole combinations by using forward and reverse scan modes. These values are from individual spectra. Each data point represents the average of three measurements. Figure from “Effects of higher-order multipoles on the performance of a two-plate quadrupole ion trap mass analyzer,” *Int. J. Mass Spectrom.*, 299, pp. 151-157, 2011.

Several previous studies have compared mass resolution between forward and reverse scans in conventional ion traps [10-14]. These investigations indicated that mass resolution obtained using the reverse scan depended on the octopole contribution in the trapping field. For

a conventional Paul trap with stretched geometry and a positive octopole component, mass resolution in a forward scan is much better than that in a reverse scan. Conversely, a compressed conventional trap geometry with a negative octopole term demonstrates better resolution in the reverse scan than that in the forward scan. This has been attributed to an effect analogous to Doppler focusing or defocusing, dependent on scan direction relative to the direction of the ion frequency shift with oscillatory amplitude. In a field with positive octopole, or when the octopole has the same sign as the quadrupole component along the axis of ion ejection, the secular frequency of ions increases with increasing amplitude of secular motion. In a field with a negative octopole component, the secular frequency of an ion decreases with the amplitude of motion. As the RF amplitude is ramped upward (forward scan), the secular frequency of a given ion increases until it nearly coincides with the frequency of the applied dipole signal. At this point the ion becomes resonantly excited, and the amplitude of its secular motion increases. A positive octopole will cause the frequency of secular motion to increase further, drawing it closer to the applied signal and causing rapid ejection. Conversely, a negative octopole will pull the secular frequency away from the applied dipole frequency, delaying ejection. During a reverse scan, the opposite occurs, and a negative octopole causes rapid ejection and better resolution. There is also an alternative explanation [15] in which the resolution in the forward and reverse scans in stretched Paul traps is attributable to the constraints on the initial conditions of ions in the trap. Coherence of ion motion in the forward scan and the absence of coherence in the reverse scan resulted in the observation of differing resolutions in the two directions. The results of Figure 5-13 show general agreement with those from the cited studies.

An additional study of the effects of scan speed on performance were studied in the Paul trap. Figure 5-14 shows the experimental results of this study. In general, faster scan speeds

give stronger signal, but slower scan speeds give more resolved signal. This could also be attributed to Doppler like effects. With faster scans, more effective energy is applied to trapped ions, causing a greater number of ions to be ejected. With slower scans, more time is allowed at specific frequencies or amplitudes to eject an ion.

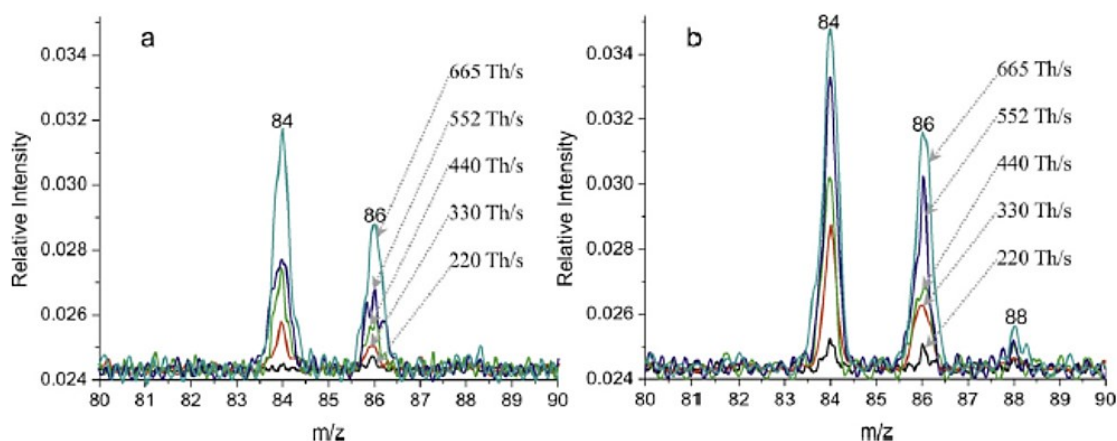


Figure 5-14: Comparison of peak intensity for the m/z 84 and 86 ions of dichloromethane using the electric field with 0.0% octopole and -4.0% dodecapole components. Both forward (a) and reverse scan modes (b) are shown. Figure from “Effects of higher-order multipoles on the performance of a two-plate quadrupole ion trap mass analyzer,” *Int. J. Mass Spectrom.*, 299, pp 151-157, 2011.

One objective of the studies done with the Paul trap was to find its prime operating conditions. The results of this effort are shown in Figure 5-15. The optimized values of higher order multipole components was 2.14% octopole and 10.49% dodecapole. The peak values of resolution are also shown in the figure.

5.3 The Coaxial Trap

The coaxial trap [16,17] utilizes the exact same substrate as that of the Paul trap design. The plates are spaced 6.0 mm from each other. Different values of potentials are applied to the 24 rings to create two independent trapping volumes: a Paul trap and a toroidal trap. This hybrid

trap is realized using only one RF power supply and two patterned ceramic plates with their respective PCBs. Figure 5-16 illustrates these trapping regions.

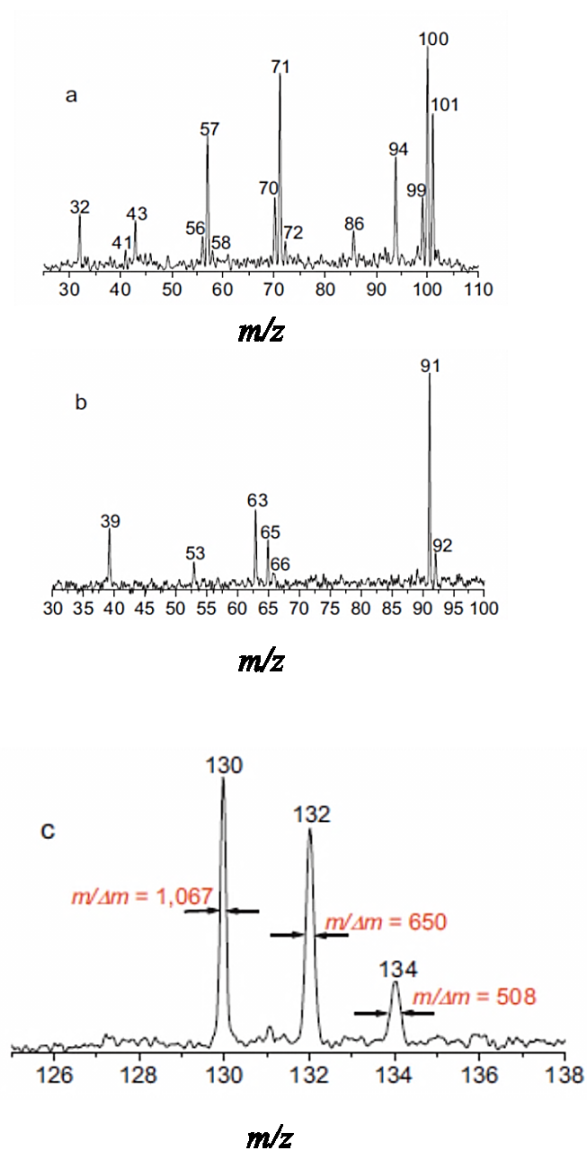


Figure 5-15: Mass spectra of (a) heptane, (b) toluene and (c) trichloroethylene using 2.14% octopole and 10.49% dodecapole components. Other conditions: (a) ionization time: 10 ms, scan speed: 330 Th/s, ac frequency: 345 kHz, scan mode: forward scan; (b) ionization time: 10 ms, scan speed: 110 Th/s, ac frequency: 340 kHz; scan mode: forward scan; and (c): ionization time: 4 ms, scan speed: 110 Th/s, ac frequency: 340 kHz, scan mode: reverse scan, and ac amplitude (1.4 V_{0-p}) is same for all cases. Figure from “Effects of higher-order multipoles on the performance of a two-plate quadrupole ion trap mass analyzer,” *Int. J. Mass Spectrom.*, 299, pp 151-157, 2011.

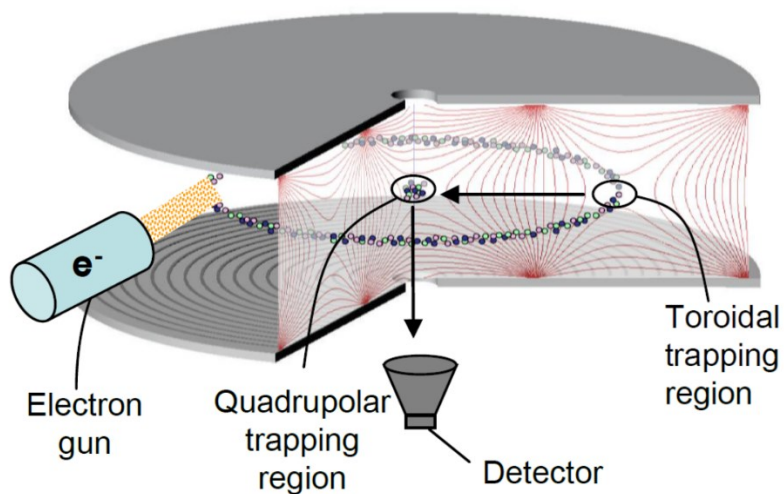


Figure 5-16: The two trapping regions of the coaxial trap. Figure from "Coaxial Ion Trap Mass Spectrometer: Concentric Toroidal and Quadrupolar Trapping Regions," *Anal. Chem.*, 83, pp. 5578-5584, 2011.

An RF power supply (PSRF-100, Ardana, North Huntingdon, PA), operated at 1.43 MHz and 500 V_{0-p}, provided the trapping RF. Supplemental signals were provided by a function generator (SRS, DS345, Sunnyvale, CA), which controlled the timing of ionization and the ejection AC signals. An AC signal used for axial resonant ejection from the quadrupole trapping region was delivered by an arbitrary waveform generator (Agilent, Model 33250A, Santa Clara, CA) and was applied at the central hole electrode. This signal was a frequency sweep. Another AC signal (used to transfer ions from the toroidal region to the quadrupole region) was provided by a function generator (SRS, DS345, Sunnyvale, CA). This signal was a constant frequency and amplitude. A custom-made electron gun and the two function generators mentioned above were triggered by two pulse generators (BNC, Models 565 and 575, San Rafael, CA). These two pulse generators and the RF power supply were synchronized by another function generator as demonstrated in Figure 5-17. Sample pressure was 2×10^{-5} torr, and helium pressure was 3×10^{-5} torr uncorrected values as measured by a pirani gauge (Kurt J. Lesker, Clairton, CA). Experiments were run in a vacuum chamber using

a 70 l/s turbo pump (Leybold, BMH70 DRY, Export, PA). A continuous-dynode electron multiplier was the detector (DeTech, Palmer, MA). The electron gun assembly with gate was identical to that of the Paul trap.

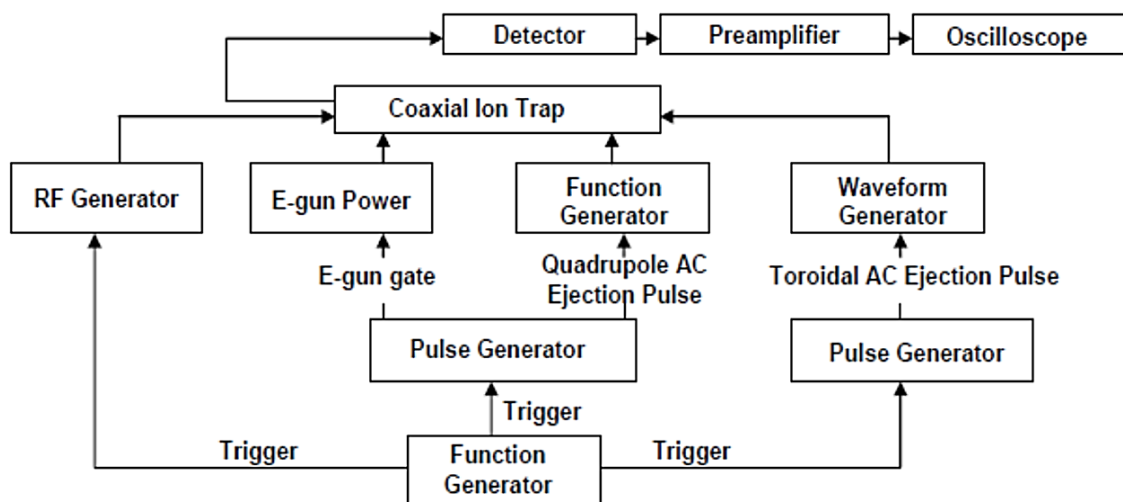


Figure 5-17: Experimental set-up for coaxial ion trap. Figure from "Coaxial Ion Trap Mass Spectrometer: Concentric Toroidal and Quadrupolar Trapping Regions," *Anal. Chem.*, 83, pp. 5578-5584, 2011.

Experiments were run in a way to incorporate both trapping regions of the coaxial trap. First, RF potential was turned off to allow the trap to empty. After RF was turned on, ionization was done with an electron gun. Next, ions were allowed to collisionally cool. Following the ions cooling down in the trap, the Paul trap region was scanned out by way of a resonant ejection frequency sweep. A second scan of the Paul region was then performed to verify that the trap was empty. Next, a 25 V_{p-p} AC signal of 1100 kHz was applied to sweep ions from the toroidal region to the Paul region. A third mass scan was then performed in the Paul region. These steps are illustrated in Figure 5-18.

The toroidal region of this trap is able to store a much larger volume of ions. One test of the extent of the toroidal volume was to repeat the transfer step from the toroidal to the Paul

region followed by an additional Paul scan for a single ionization event. The control signals and the timing for the coaxial experiments is shown in Figure 5-19.

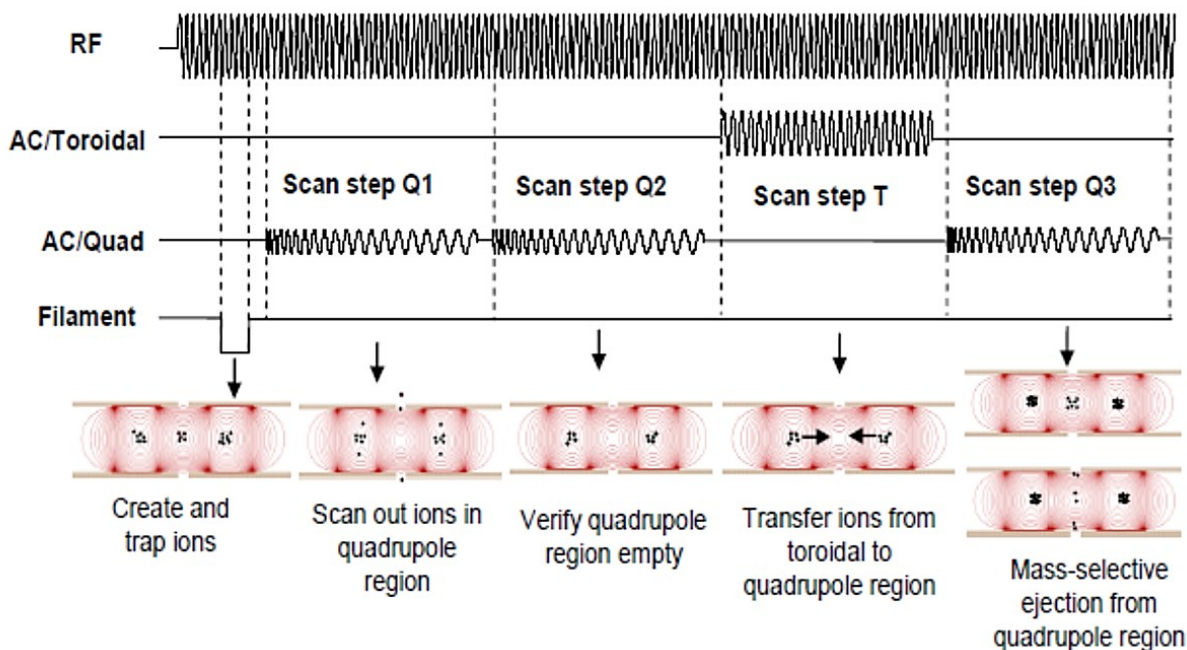


Figure 5-18: The various phases of the mass analysis performed with the coaxial trap. Figure from "Coaxial Ion Trap Mass Spectrometer: Concentric Toroidal and Quadrupolar Trapping Regions," *Anal. Chem.*, 83, pp. 5578-5584, 2011.

5.3.1 Field Design

The potentials applied to each ring are shown in Table 5.2. The choice of potential values for each ring was made by modeling the electric fields using SIMION 8.0 and the procedure outlined in Appendix C. The trapping field of the radial direction (along $z = 0$) in the coaxial ion trap was simulated to approximate the radial field in the previously developed toroidal ion trap. The trapping field in the Paul trap region was selected to be similar to the axial field in the previously described Paul trap. Figure 5-20 illustrates the potentials and electric fields within the trapping regions.

The ejection AC from the Paul trap was applied to the 3rd and 5th rings. The transfer AC from the toroidal was applied to the 23rd and 24th rings. The toroidal AC was applied to the outermost rings to provide the radial push to transfer ions in the direction from the toroidal region to the Paul region.

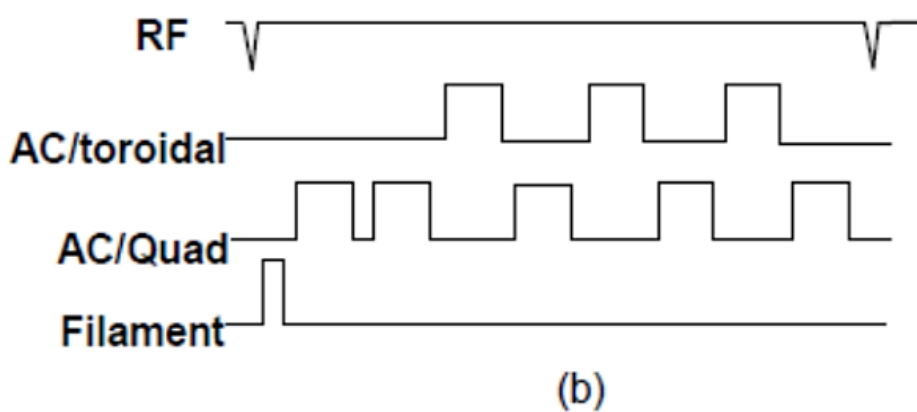
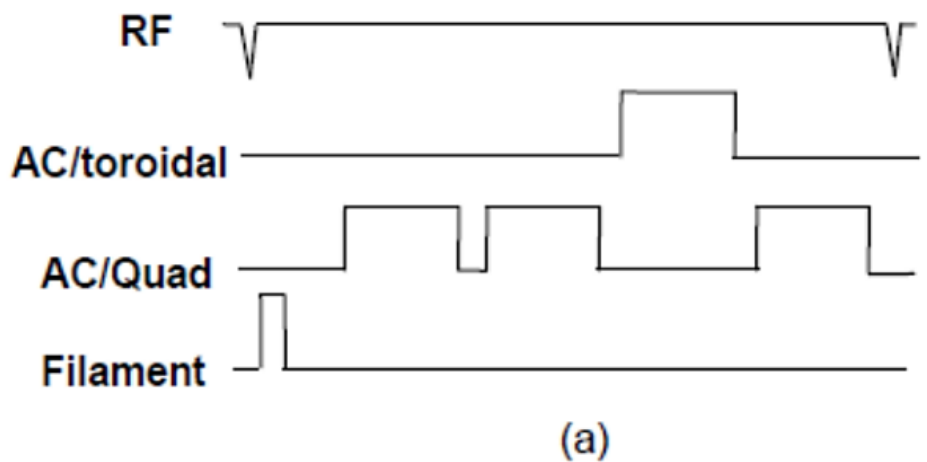


Figure 5-19: Control signal timing for (a) a single toroidal transfer experiment and (b) multiple toroidal transfer experiments. Figure from "Coaxial Ion Trap Mass Spectrometer: Concentric Toroidal and Quadrupolar Trapping Regions," *Anal. Chem.*, 83, pp. 5578-5584, 2011.

Table 5.2: RF potentials applied to the specific rings of the 24 ring ceramic to create the coaxial trap.

Ring Number	Inner-outer radius (mm)	RF Potential Vp-p
1	0.5-1.8	8
2	2.2-2.3	81
3	2.7-2.8	0
4	3.2-3.3	81
5	3.7-3.8	0
6	4.2-4.3	118
7	4.7-4.8	318
8	5.2-5.3	379
9	5.7-5.8	500
10	6.2-6.3	460
11	6.7-6.8	500
12	7.2-7.3	467
13	7.7-7.8	491
14	8.2-8.3	500
15	8.7-8.8	491
16	9.2-9.3	500
17	9.7-9.8	479
18	10.2-10.3	472
19	10.7-10.8	472
20	11.2-11.3	362
21	11.7-11.8	264
22	12.2-12.3	138
23	12.7-12.8	0
24	13.2-13.3	0

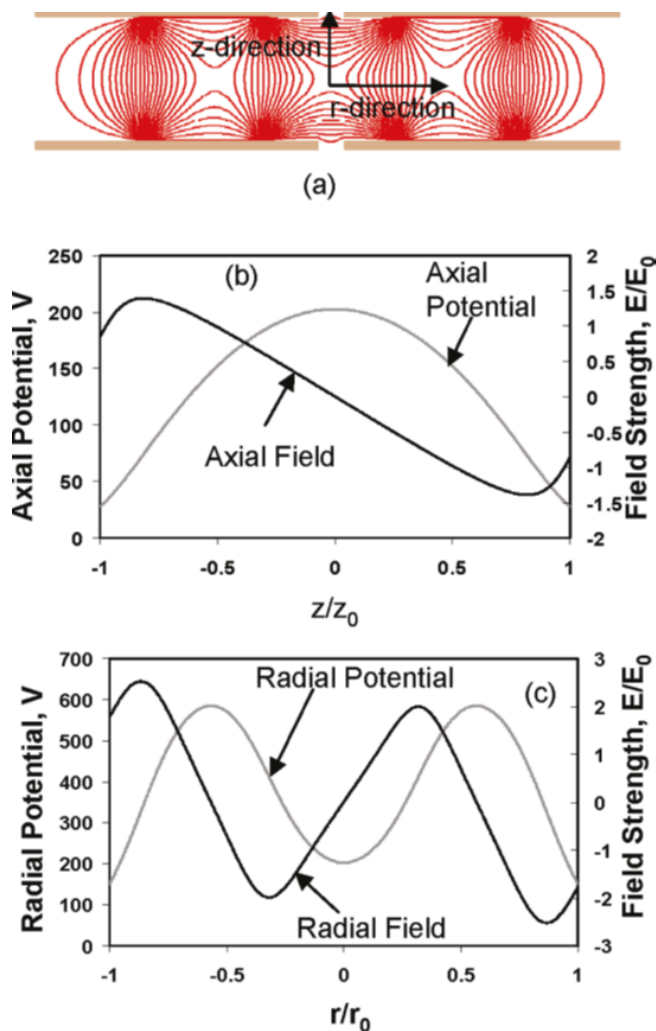


Figure 5-20: The fields and potentials of the coaxial ion trap. (a) Equipotential contour plot, (b) Axial Potential and Field, designed to approximate the Paul trap, (c) Radial Potential and Field, designed to approximate the toroidal trap. Figure from "Coaxial Ion Trap Mass Spectrometer: Concentric Toroidal and Quadrupolar Trapping Regions," *Anal. Chem.*, 83, pp. 5578-5584, 2011.

5.3.2 Results

Figure 5-21 portrays results taken from mass analysis experiments on the coaxial trap. The results of this experiment utilize repeated ion transfer from the toroidal region. At this point, mass selective transfer from the toroidal region to the Paul region has yet to be realized. The toroidal transfer process as presented here is an all-or-nothing prospect with regards to mass range. However, as is shown by the repeated transfers, large numbers of ions are stored in the

toroidal region compared to the Paul region. Experiments have been run with up to 30 consecutive transfer/scan steps with no loss in ion intensity in the Paul scan signal. Higher numbers of scans were limited by available electronics. Geometrically, the toroidal region should be 100-200 times larger than the Paul trapping volume. The compound measured in Figure 5-21 is bromopentafluorobenzene. Resolution with this configuration is modest, but it demonstrates the viability of a coaxial trap design.

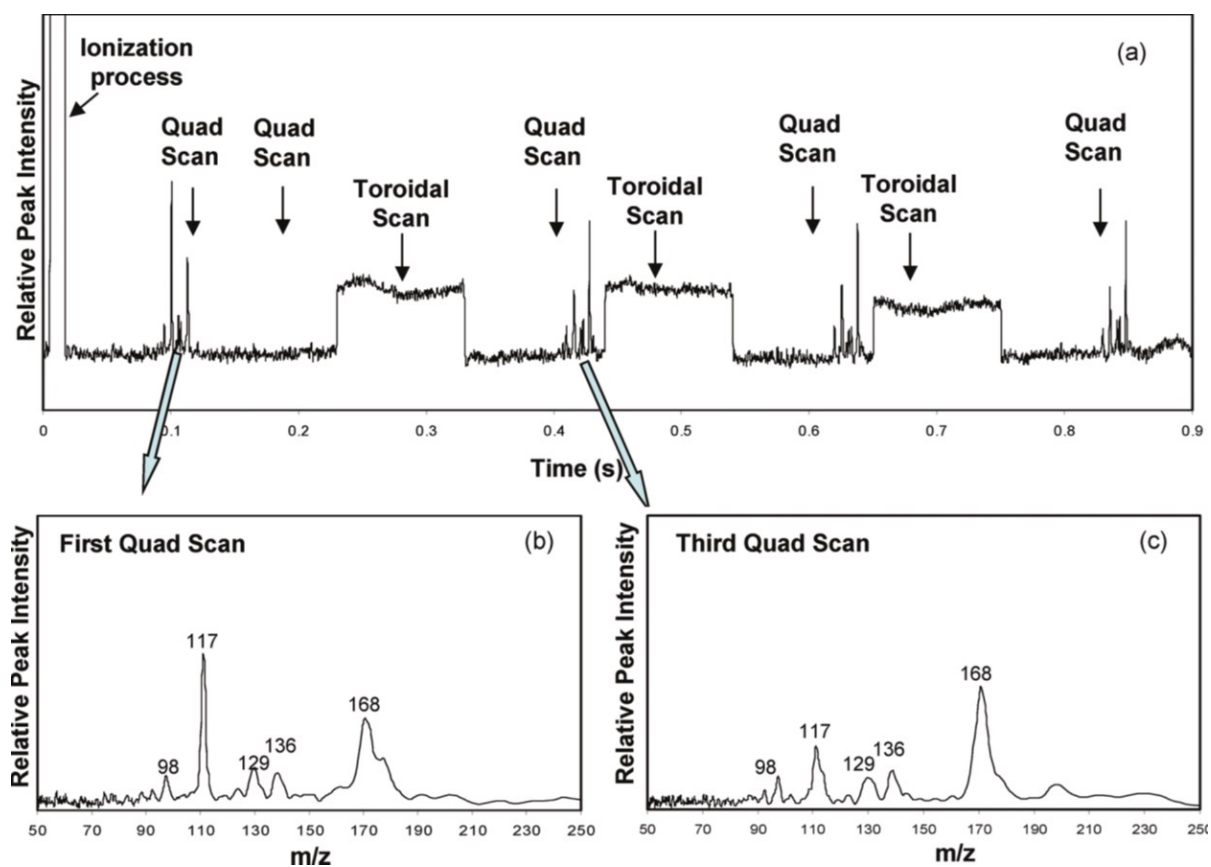


Figure 5-21: Coaxial ion trap mass spectrum of bromopentafluorobenzene: (a) data acquired during entire experiment (b) mass spectrum for the first quadrupole scan, (c) mass spectrum for the third quadrupole scan (after the first toroidal transfer). Figure from "Coaxial Ion Trap Mass Spectrometer: Concentric Toroidal and Quadrupolar Trapping Regions," *Anal. Chem.*, 83, pp. 5578-5584, 2011.

References

- [1] D. E. Austin, M. Wang, S. E. Tolley, J. D. Maas, A. R. Hawkins, A. L. Rockwood, H. D. Tolley, E. D. Lee and M. L. Lee, "Halo Ion Trap Mass Spectrometer," *Anal. Chem.*, vol. 79, pp. 2927-2932, 2007.
- [2] M. Wang, H. E. Quist, B. J. Hansen, Y. Peng, Z. Zhang, A. R. Hawkins and D. E. Austin, "Performance of a Halo Ion Trap Mass Analyzer with Exit Slits for Axial Ejection," *J. Am. Soc. Mass Spectrom.*, vol. 22, no. 2, pp. 369-378, 2011.
- [3] Z. Zhang, Y. Peng, B. J. Hansen, I. W. Miller, M. Wang, M. L. Lee, A. R. Hawkins and D. E. Austin, "Paul Trap Mass Analyzer Consisting of Opposing Microfabricated Electrode Plates," *Anal. Chem.*, vol. 81, no. 13, pp. 5241-5248, 2009.
- [4] D. E. Austin, B. J. Hansen, Y. Peng and Z. Zhang, "Multipole expansion in quadrupolar devices comprised of planar electrode arrays," *Int. J. Mass Spectrom.*, vol. 295, no. 3, pp. 153-158, 2010.
- [5] J. Franzen, R. -H. Gabling, M. Schubert and Y. Wang, *Practical Aspects of Ion Trap Mass Spectrometry*, vol. 1, p. 49, New York, USA: CRC Press, 1995.
- [6] J. C. Schwartz, J. E. P. Syka and I. Jardine, *J. Am. Soc. Mass Spectrom.*, vol. 2, p. 198, 1991.
- [7] D. E. Goeringer, S. A. McLuckey and G. L. Glish, in *Proc. 39th ASMS Conf. Mass Spectrometry and Allied Topics*, Nashville, TN, 1991, p. 32.
- [8] J. Williams, K. Cox, K. Morand, R. Cooks, R. J. Jr. and R. Kaiser, "Proc. 39th ASMS Conf. Mass Spectrometry and Allied Topics," p. 1481, Nashville, TN, 1991.
- [9] R. Kaiser, R. Cooks, G. Stafford, J. Syka and P. Hemberger, *Int. J. Mass Spectrom. Ion Process.*, vol. 106, p. 79, 1991.
- [10] J. Williams, K. A. Cos, R. G. Cooks, S. A. McLuckey, K. J. Hart and D. E. Goeringer, "Resonance Ejection Ion Trap Mass Spectrometry and Nonlinear Field Contributions - The Effect of Scan Direction on Mass Resolution," *Anal. Chem.*, vol. 66, pp. 725-729, 1994.
- [11] G. Dobson, J. Murrell, D. Despeyroux, F. Wind and J. -C. Tabet, "Investigations into the use of a reverse scan in a quadrupole ion trap mass spectrometer," *Rapid Commun. Mass Spec.*, vol. 17, pp. 1657-1664, 2003.
- [12] M. Wang, in *Proc. 43rd ASMS Conf. Mass Spectrometry and Allied Topics*, p.1121, Atlanta, GA, 1995.

- [13] V. M. Doroshenko and R. J. Cotter, "Losses of ions during forward and reverse scans in a quadrupole ion trap mass spectrometer and how to reduce them," *J. Am. Soc. Mass. Spectrom.*, vol. 8, pp. 1141-1146, 1997.
- [14] J. M. Wells, W. Plass and R. Cooks, "Control of Chemical Mass Shifts in the Quadrupole Ion Trap through Selection of Resonance Ejection Working Point and rf Scan Direction," *Anal. Chem.*, vol. 72, pp. 2677-2683, 2000.
- [15] N. Rajanbabu, A. Chatterjee and A. Menon, "Motional coherence during resonance ejection of ions from Paul traps," *Int. J. Mass Spectrom.*, vol. 261, pp. 159-169, 2007.
- [16] Y. Peng, Z. Zhang, B. J. Hansen, M. Wang, M. L. Lee, A. R. Hawkins and D. E. Austin, "Coaxial Ion Trap: Two Superimposed Trapping Regions in One Analyzer," in *Pittcon*, Orlando, FL, 2010.
- [17] Y. Peng, B. J. Hansen, H. Quist, Z. Zhang, M. Wang, A. R. Hawkins and D. E. Austin, "Coaxial Ion Trap Mass Spectrometer: Concentric Toroidal and Quadrupolar Trapping Regions," *Anal. Chem.*, vol. 83, no. 14, pp. 5578-5584, 2011.

6 THE PLANAR LINEAR ION TRAP

6.1 Introduction

The most recent design of planar electrode traps is a planar linear ion trap (PLIT) [1]. The general theory of this device has been covered in previous chapters, but some key points will be emphasized here for convenience. This trap design carries several theoretical advantages over previous ion traps. The PLIT, like the toroidal trap, has an expanded trapping volume compared to the Paul trap [2, 3]. However, the PLIT avoids some of the mathematical problems that come from the toroidal trap, and maintains the relative simplicity of the equations governing the Paul trap. The equations governing the PLIT are a two dimensional form of the Paul trap equations. A schematic view of the electrode design used for this trap is shown in Figure 6-1.

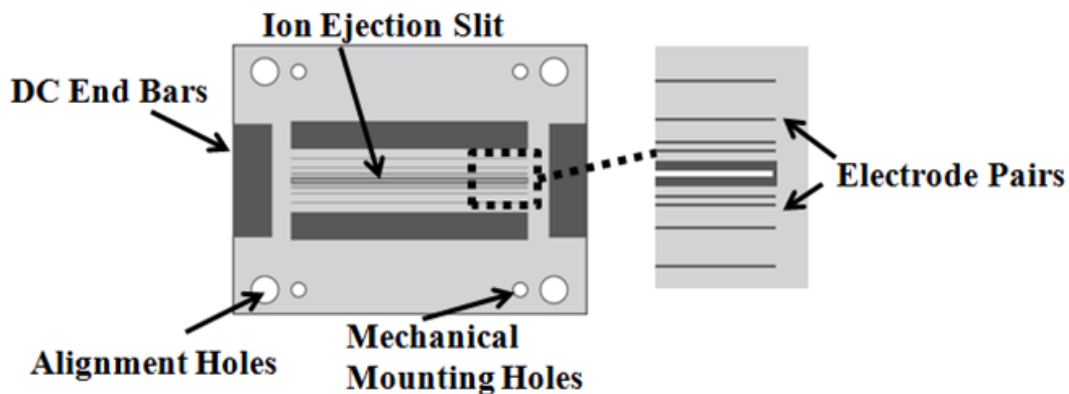


Figure 6-1: Schematic view of the PLIT plate design. Figure from “A Lithographically Patterned Discrete Planar Electrode Linear Ion Trap Mass Spectrometer,” *J. Microelectromech. Sys.*, (in press).

The PLIT plate substrate is the same 0.635” thick ceramic used in the other planar electrode designs. The space between plates is 4.38 mm. There is a slit 500 μm wide along the center of the plate. This slit provides the path for ion ejection from the trapping volume to a detector. On either side of the slit lays a pattern of symmetric pairs of metal electrodes. There are a total of eleven electrodes, one that covers the central slit and five symmetric pairs about the central slit. The nearest four pairs have a line width of 25 μm , while the outermost pair has a width of 4.5 mm. The highest trapping potentials are applied to the outermost line pair. The 5th line pair is wider to help ensure a geometrically large trapping boundary, making it more difficult for ions to leak out of the trap. This pair can be wider without negatively impacting the potential function because the lines are located far from the center of the trapping volume. The locations of these electrodes within the trapping volume are summarized in Table 6.1. The two metal bars on the ends of the plates are given a constant DC potential for axial confinement of ions. The shape of this electrode was chosen to approximate the shape of a conventional PLIT. The arrangement of the plates and the trapping volume are depicted in Figure 6-2.

Table 6.1: Locations of the electrodes on the PLIT.

Line Pair	Electrode location (mm)
1	0.90-0.92
2	1.25-1.27
3	2.18-2.20
4	3.78-3.80
5	5.5-10.0

Some simulation work has been done to further understand operation of this trap. Figure 6-3 shows the results of simulations done in SIMION. These figures show the trapping well formed in both the y axis and the z axis with this type of electrode pattern. Simulations have also

shown that as ions are ejected out of the trap, they are ejected in the direction of the slit and not out of the side of the trap along the x axis.

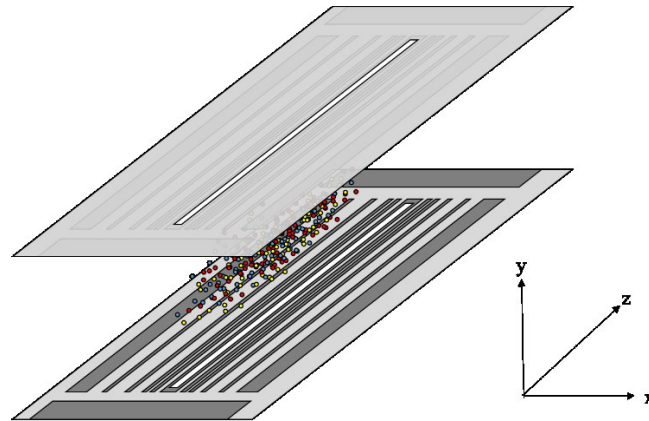


Figure 6-2: The electrode arrangement and stored ions in a planar electrode PLIT.

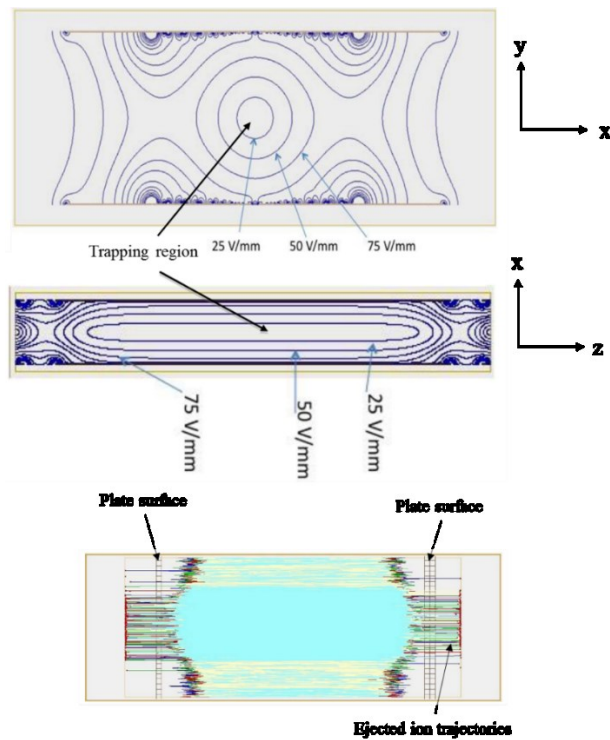


Figure 6-3: (top) Electropotential contour plots of the PLIT at $z = 0$, or the center of the slit. (middle) Electropotential contour plots of the PLIT at $y = 0$, or halfway between the plates. (bottom) SIMION simulation of ejected ion trajectory.

6.2 Field Design

When analyzing the trapping fields of the PLIT, it is most useful to analyze the fields with respect to y for $z = 0$ and for $x = 0$ (using the axes defined in Figure 6-2). The y direction is most important as this is the axis of ejection. While ions are stored along the length of the line pairs, the majority will be concentrated towards the center of the plate due to the DC applied to the end bars. The potential function will describe the potential between the centers of the two plates.

The 2D equation for the potential function takes the form

$$\Phi(x, y, t) = \Phi_0 \sin(\Omega t) \sum_{N=0}^{\infty} A_N \Phi_N, \quad (6.1)$$

where Φ_0 and Ω are the amplitude and angular frequency of the applied RF, and A_N is the amplitude of the individual multipole Φ_N , and Φ_N is described by the set of 2-dimensional Legendre polynomials [4]. The electric potential in the trap is typically dominated by the quadrupole (quadratically varying) term, but includes terms representing all higher-order components (octopole, 12-pole, etc.) allowed by the symmetry of the device. The above equation ignores the DC trapping field in the z direction, along the length of the device. Due to the nature of the Laplace equation and the superposition principle in the PLIT, the trapping potential within the whole device can be represented as the sum of the potentials created by each individual electrode. Each symmetric pair of lines has its own values for the multipole expansion. The total trapping field is a linear summation of the field formed from each line pair.

The potential distribution in the space between plates was calculated using SIMION 8.0 (Scientific Instrument Services, Ringoes, NJ) for each line pair separately. The resulting 2-dimensional multipole expansions were then calculated with Matlab (Mathworks, Natick, MA)

using the procedure outlined in Appendix C. The individual contribution from each line pair is depicted graphically in Figure 6-4. When these curves are fitted to a 20th order polynomial, the fitted equations are shown in Table 6.2. Due to the symmetry of the device, the odd ordered terms are negligible.

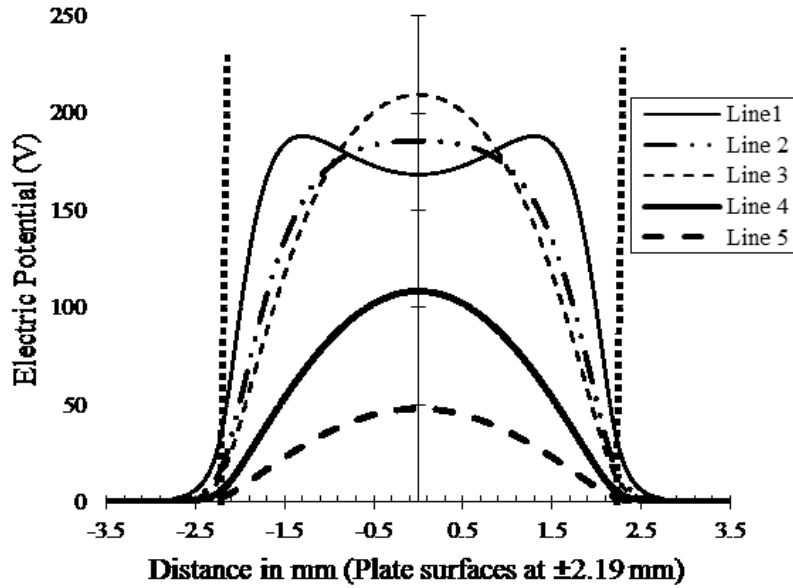


Figure 6-4: The potential created in the trapping region (between the plates) by each line pair with 1000 V applied to a single line pair and independent of other pairs. The plate surfaces are represented by dashed vertical lines. Area on the graph not between these lines is the potential seen as particles travel through the ejection slit. Figure from “A Lithographically Patterned Discrete Planar Electrode Linear Ion Trap Mass Spectrometer,” *J. Microelectromech. Sys.*, (in press).

Table 6.2: Calculated equations for the curves in Figure 6-4.

Line Pair	A2(x ²)	A4(x ⁴)	A6(x ⁶)	A8(x ⁸)	A10(x ¹⁰)
1	18.4	-2.525	2.06	-5.0509	4.389
2	-7.0538	-6.2327	0.8457	-2.3571	2.1646
3	-34.6738	-3.8072	1.3366	-1.7502	1.62
4	-25.6412	0.2638	0.567	-0.7763	0.7001
5	-12.2671	0.4456	0.2134	-0.3428	0.3083

The desired trapping field is determined by selecting an appropriate coefficient by which to multiply each of the curves in Table 6-2, and then adding up the results. The quadrupole component should be dominant, but there will also exist some higher-order contributions. The multiplying coefficients correspond to the specific RF voltage amplitudes to apply to each line pair on the plate surface. This summation not only helps calculate the total trapping potential, but also the components of the individual higher order multipoles. This is calculated by

$$A_2 = A_{21}\Phi_{01} + A_{22}\Phi_{02} + A_{23}\Phi_{03} + \cdots + A_{2m}\Phi_{0m}, \quad (6.2)$$

$$A_4 = A_{41}\Phi_{01} + A_{42}\Phi_{02} + A_{43}\Phi_{03} + \cdots + A_{4m}\Phi_{0m}, \quad (6.3)$$

$$A_6 = A_{61}\Phi_{01} + A_{62}\Phi_{02} + A_{63}\Phi_{03} + \cdots + A_{6m}\Phi_{0m}, \quad (6.4)$$

where for A_{nm} , n is the multipole number (A_2 , A_4 , A_6 , etc.), m is the line pair numbered from the center slit, and Φ_m is the RF amplitude applied to line m . By selecting proper RF amplitudes for each line pair, a field profile can be formed with values of higher order multipoles that yield more efficient ion ejection and better resolved mass spectra. An example of a potential field is shown in Figure 6-5.

It is beneficial to view how calculated fields based on a real instrument compare to ideal fields. One possible configuration of electric field is shown in Figure 6-6. This field is designed to match an ideal field over a large percentage of the plate spacing, but sacrifices some overall potential well depth. The higher order multipoles for this field are 0.803% octopole and -2.676% octopole. Just as in the Paul trap, it is beneficial to have a component of positive octopole when performing a forward mass scan, or in other words, ejecting ions from the trap from low to high mass. There are sharp deviations from the ideal field and the calculated field right at the edges

of the trapping volume. These deviations represent the edge effects on the field caused as an ion approaches the ejection slit.

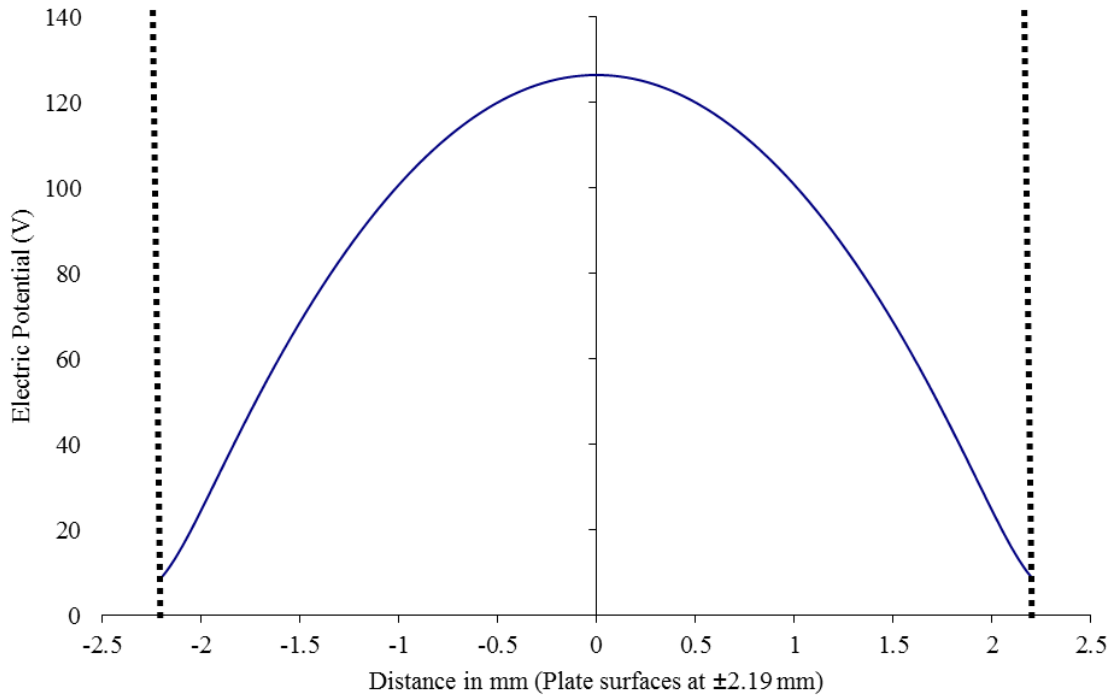


Figure 6-5: A trapping potential used when adding weighted individual line pair functions.

One successful field configuration has an octopole of 2.14% and a dodecapole of -2.58%. This electric field was designed to approximate the high-performance field of the planar electrode Paul trap. This is a useful approach due to the similarity in the equations governing the two types of traps. The PLIT field has the same octopole value, and as close of dodecapole value as was possible with the Paul trap with this electrode configuration. The comparison of this field to an ideal field is shown in Figure 6-7. While the dodecapole is different between this trap and the Paul trap, the octopole component has the most influence on resolution [5].

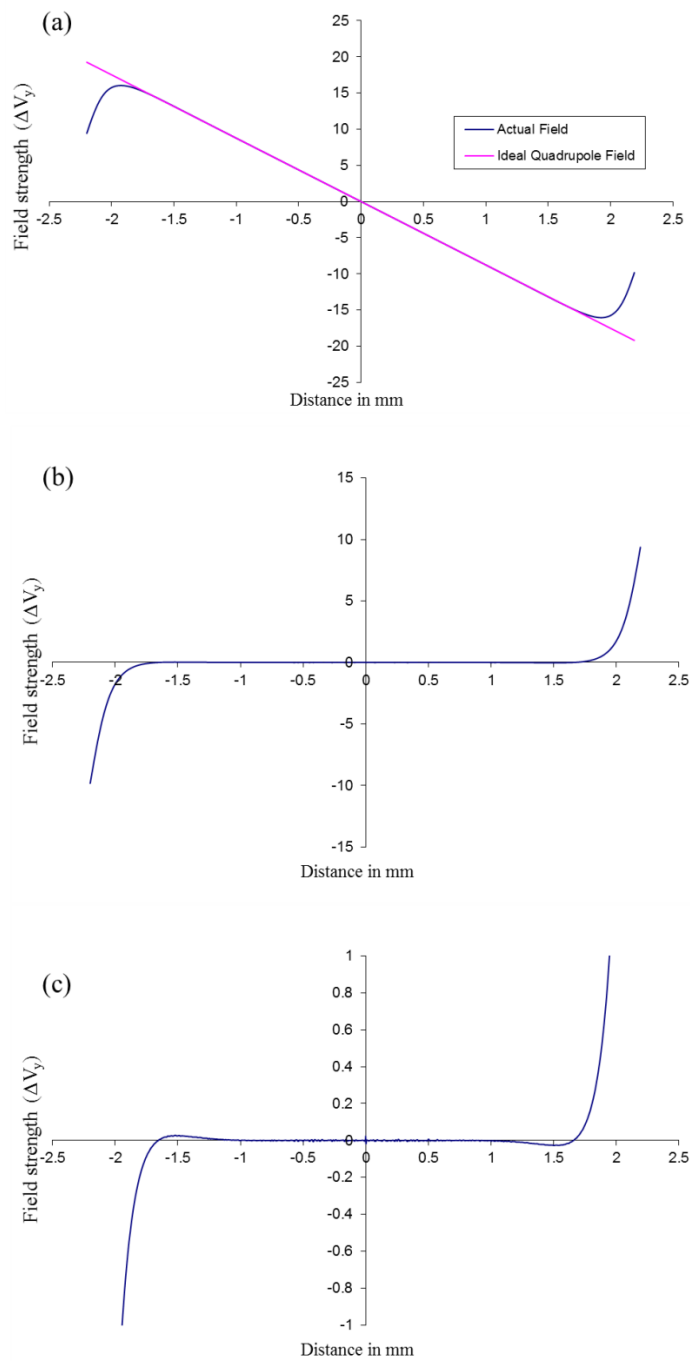


Figure 6-6: A field with higher order components of 0.803% octopole and -2.676% dodecapole. (a) The electric field of the PLIT compared to an ideal field. (b) The difference between the ideal field and the calculated field. (c) A zoomed in view of plot (b).

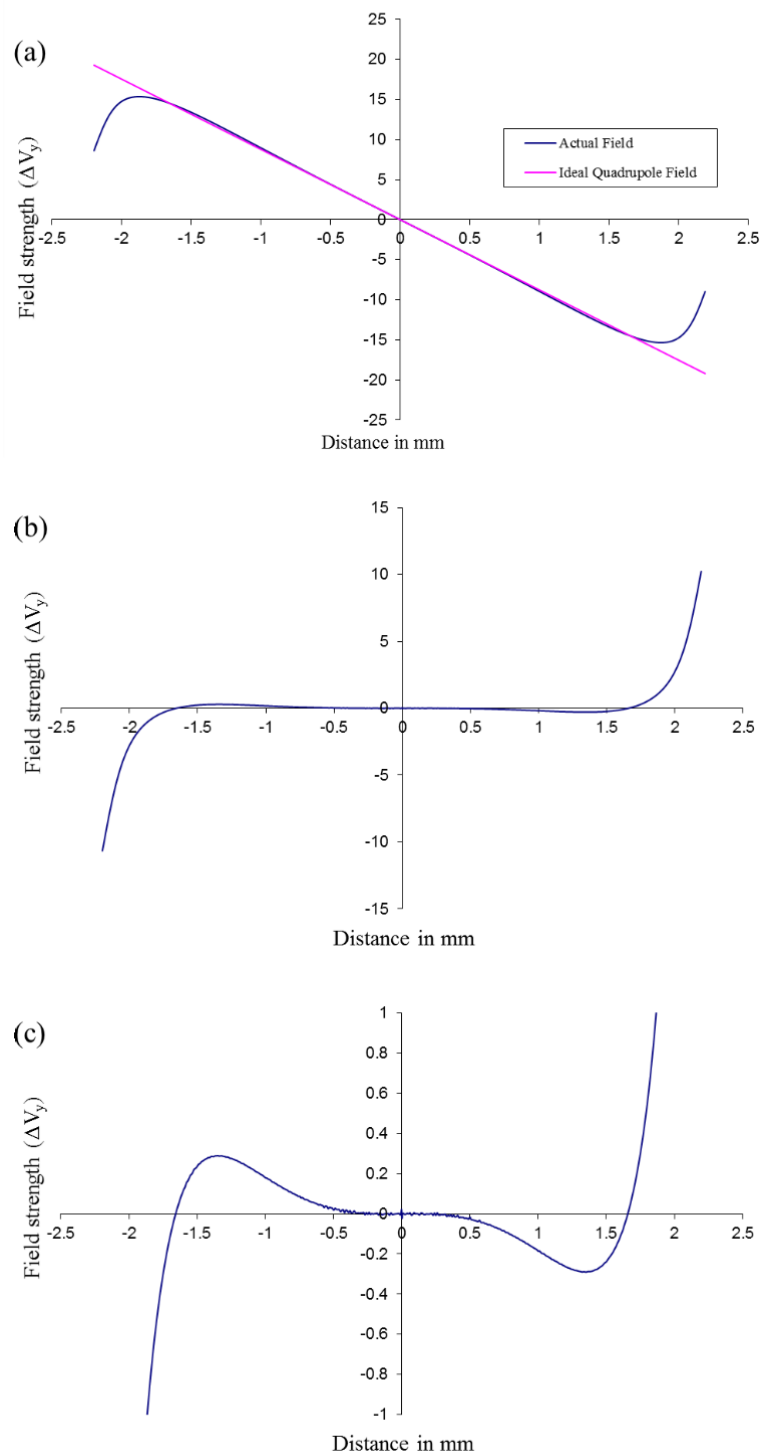


Figure 6-7: A field with higher order components of 2.14% octopole and -2.58% dodecapole. (a) The electric field of the PLIT compared to an ideal field. (b) The difference between the ideal field and the calculated field. (c) A zoomed in view of plot (b).

6.3 Experimental Setup

6.3.1 Trap Assembly

The experimental setup of this trap is very similar to that of the designs discussed in Chapter 5. A 0.635” thick piece of alumina is prepared by a vendor (Hybrid-Tek, Clarksburg, NJ) that laser cuts all of the holes and has the vias filled with metal (Questech, Garland, TX). Metal, either aluminum or the chrome/gold stack described in Chapter 4, is patterned by the BYU IML into the arrangement shown in Figure 6-8. The trapping side is patterned with parallel metal lines, while the back side is patterned with contact squares for pogo pins and metal traces that lead to the vias. Each line electrode has two vias, one on either side of the line. The redundant via helps increase the overall yield of the IML processing. A PCB with a capacitive voltage divider circuit and gold-coated spring-loaded pogo pins is mounted to the back side of each plate. The PCB-plate assembly is shown in Figure 6-9.

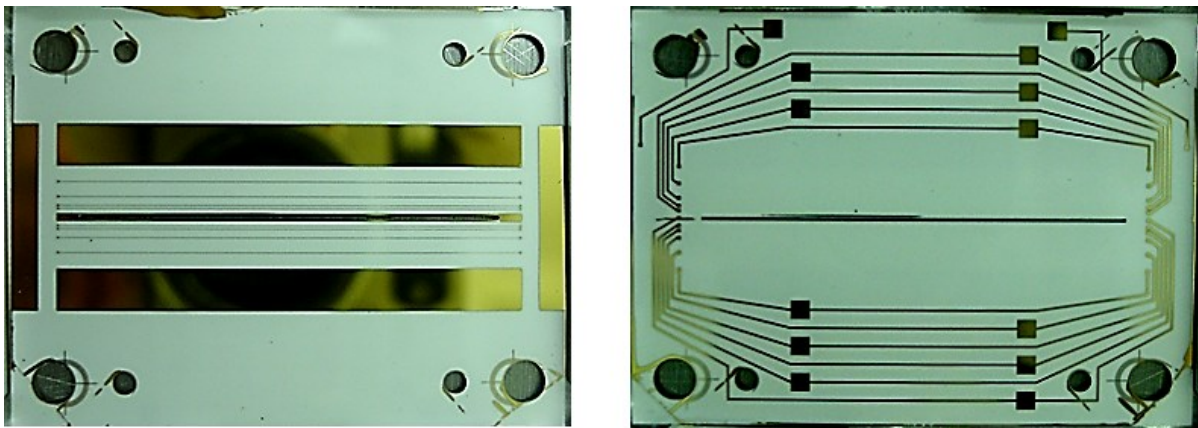


Figure 6-8: (left) Trapping side of the PLIT. (right) Voltage connection side of the PLIT.

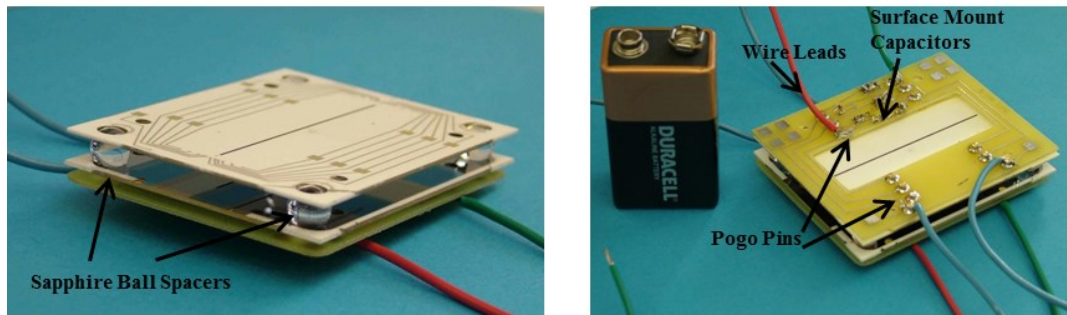


Figure 6-9: Actual plate/PCB assembly. (left) Top PCB removed. (right) Complete plate/PCB assembly. Figure from “A Lithographically Patterned Discrete Planar Electrode Linear Ion Trap Mass Spectrometer,” *J. Microelectromech. Sys.*, (in press).

The plate/PCB assembly is mounted and secured using screws through the mechanical mounting holes in the ceramic and the PCBs. The screws are tightened with springs to avoid over tightening of the plate/PCB assembly, which can crack the ceramic plate. The total trap assembly with electrical connections is shown in Figure 6-10. On the detector side of the trap, a copper box shields ejected ions from being diverted by electric fields emanating from the PCB. The shielding box extends past the PCB to 0.010” under the ejection slit on the detector side plate, providing a shielded path from plate to detector, which is also shielded with a copper assembly. The wires carrying RF voltage are also shielded to limit RF noise generated throughout the vacuum chamber.

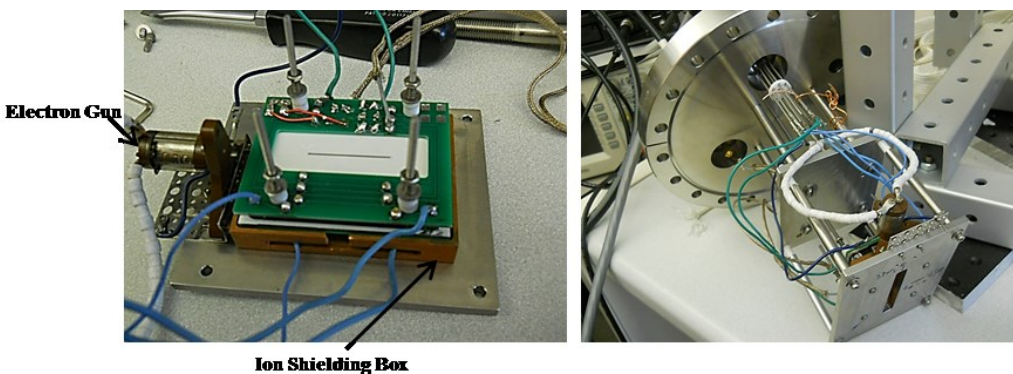


Figure 6-10: (left) The ion trap assembly secured together with electron gun. (right) Trap assembly mounted to a vacuum flange in its completed operational form.

6.3.2 Equipment Specifications

RF power was supplied by a self-tuning Ar dara power supply (PSRF 100, Ar dara, PA). The frequency of the RF supply was 2.5 MHz and was capable of 1700 V_{0-p}. The detector used was a continuous dynode electron multiplier by DeTech (Palmer, MA). An electron gun from Torion Technologies (American Fork, UT) was placed to inject electrons into the trapping area between the two plates down the long axis of the plates, creating ions within the trapping region. Additional control signals for the RF power supply and for the AC resonant ejection signal were supplied by DS345 function generators (Stanford Research Systems, Sunnyvale, CA). Additional timing and control pulses were produced by a pulse generator (BNC, Model 565, San Rafael, CA), and custom built electronics. Output signal was amplified using a current amplifier (Model 427, Keithley Instruments, Cleveland, OH) and recorded using a digital oscilloscope (Wave Runner 6000A, LeCroy, Chestnut Ridge, NY). Figure 6-11 diagrams the various control signals and Figure 6-12 is a picture of the entire lab bench assembly.

The vacuum chamber is evacuated by a 230 L/s turbopump (Oerlikon Leybold, Model 4280A, Export, PA). Sample gas is leaked first through Swagelok fittings and a Granville-Phillips 203 variable leak valve (Longmont, CO). An ion gauge (MDC, Hayward, CA) is used to measure sample pressure. Helium gas is then leaked into the vacuum chamber using a leak valve (Swagelok, Solon, OH). Helium pressure is measured using uncorrected pressure measurements from a pirani gauge (Kurt J. Lesker, Clairton, CA).

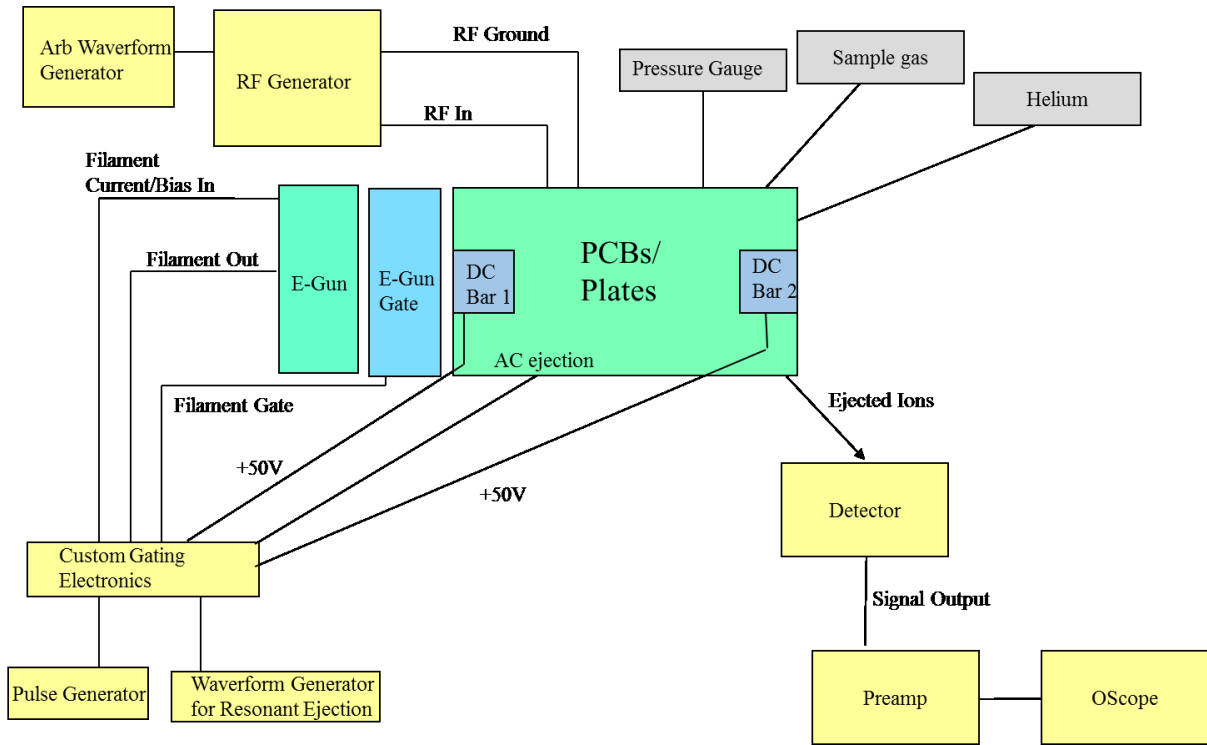


Figure 6-11: Diagram of trap inputs and outputs.

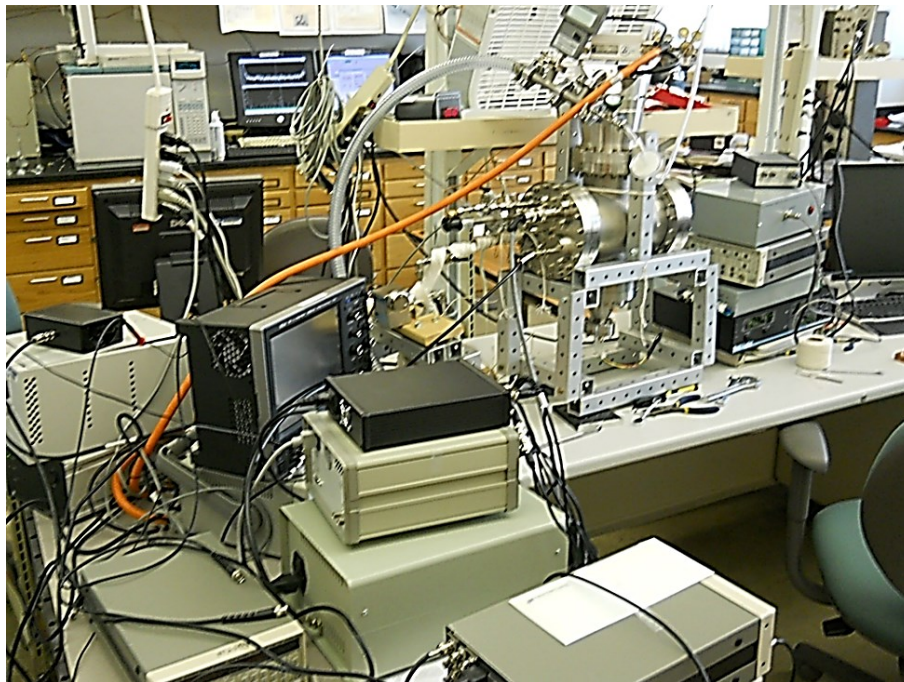


Figure 6-12: Lab bench for the PLIT setup.

6.3.3 Experimental Parameters

There were two types of experiments run with the PLIT. One experiment was to perform mass analysis with a frequency sweep of the resonant ejection signal while maintaining a constant RF amplitude. The other type of experiment was done with a constant resonant ejection signal on top of a ramping amplitude of the RF power supply. The ramping RF would increase the secular frequencies of the trapped ions until their frequencies matched the constant resonant ejection signal.

Each type of scan consists of the same basic steps. First, RF power was turned on, forming the trapping well. Next, the electron gun gate was opened which created the ions of a sample gas inside the trap. After the gate was closed, ions were allowed to collisionally cool inside the trap. Next, a mass scan was performed. Finally, the RF power was set to 0 to allow any remaining ions to clear out of the trap. The relative timing of these signals is shown in Figure 6-13.

One important factor in ion trap performance is a proper number of ions within the trap. A method of controlling the total number of ions in a trap is to control the total amount of sample pressure leaked into the vacuum chamber. An example of mass analysis signals under different sample pressures, but with other identical experimental conditions, is shown in Figure 6-14. If there are too many ions in the trap, space charge effects will alter the trapping fields in such a way to cause degenerated resolution.

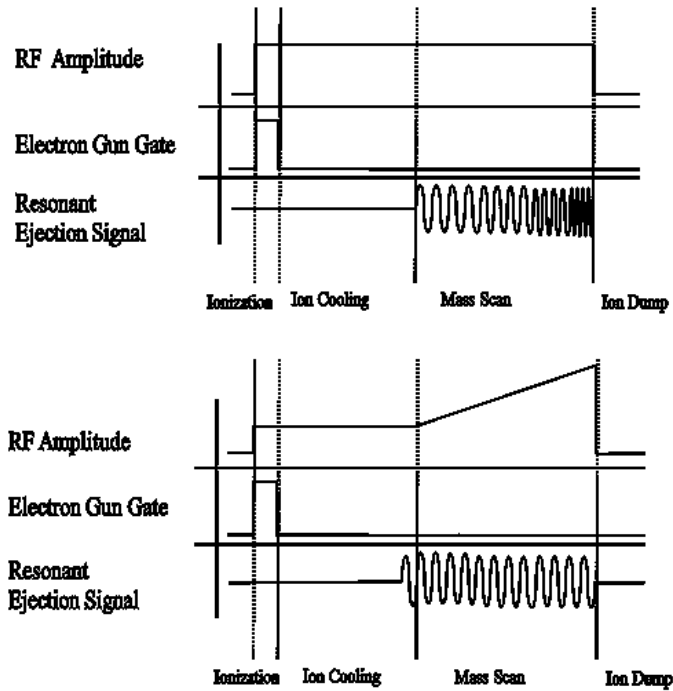


Figure 6-13: A diagram showing the timing of various control signals of the LIT system. (top) Frequency sweep scan. (bottom) Linear amplitude ramp. Figure from "A Lithographically Patterned Discrete Planar Electrode Linear Ion Trap Mass Spectrometer," *J. Microelectromech. Sys.*, (in press).

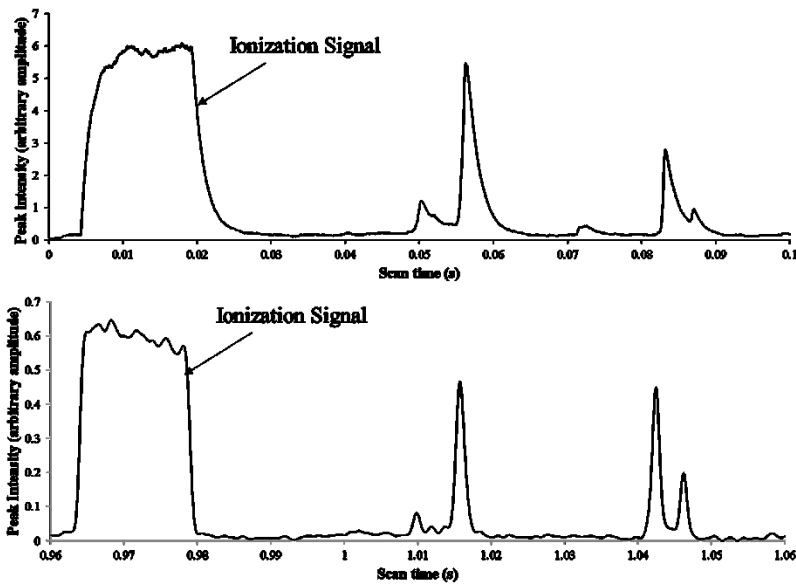


Figure 6-14: A comparison between two identical mass analysis experiments but with different sample pressure. (top) 5×10^{-5} torr sample pressure, (bottom) 1×10^{-5} torr sample pressure.

6.4 Results

6.4.1 Frequency Sweep

A mass frequency scan was used with an electric field consisting of 0.803% octopole and -2.676% dodecapole. The voltages from lines 1 to 5 were 0.035, 0.035, 0.117, 0.38, and 1 times the output of the RF power supply, respectively. During the frequency sweep mass scan, the RF power supply was set at 720 V_{0-p} at a frequency of 2.3 MHz. The RF power supply also had a DC offset of 3.5 V. An additional AC signal of 3.5 V_{0-p} was applied to the central line of one of the plates to cause resonant mass dependent ion ejection. The frequency of this resonant signal was swept from 1.1 MHz to 100 kHz over a time period of 100 ms. Sample gasses were leaked into the vacuum chamber at a pressure of 5×10⁻⁶ torr as measured with an ion gauge. Additionally, a background helium buffer gas was also leaked in at a pressure of 3×10⁻³ torr as measured with a pirani gauge. Both pressures are uncorrected for response of the pressure gauge. The raw data and a calculated mass scale are shown in Figure 6-15. The compound measured in this experiment was isobutylbenzene.

The peaks of lower *m/z* values in this experiment have a FWHM of 0.35 mass units, for a resolution (*m/Δm*) of 110-120. However, as mass increases, resolution rapidly begins to suffer. The peak at *m/z* 77 has a FWHM of 1.7 mass units, for a resolution of 45. Like the frequency scans in the toroidal trap, this trap suffers from a rapid degradation in resolution at higher masses. The scan in the figure is an average of 20 different mass scans.

The results of this frequency scan are similar in principle to those of the toroidal trap frequency scans. It is likely that some of the same resolution issues that beset the toroidal design with high *m/z* values also apply with the PLIT frequency sweep scans. Ions of higher *m/z* values are in shallower wells, and are able to be scanned out over a wider range of frequencies when

using a frequency sweep scan. A higher trapping voltage can help to narrow this range of frequencies by creating a deeper trapping well.

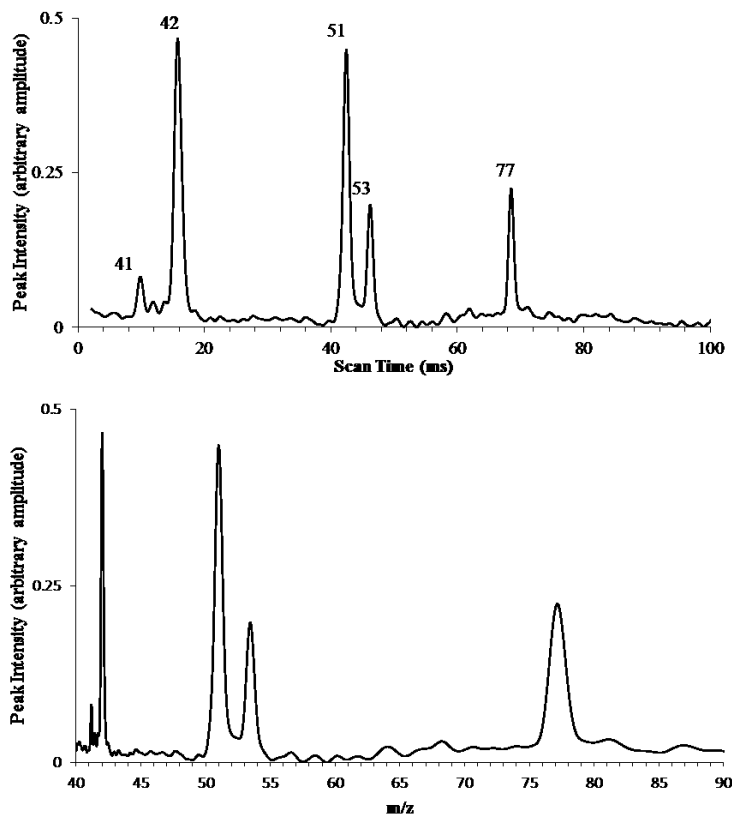


Figure 6-15: Frequency sweep with 0.803% octopole and -2.676% dodecapole. Isobutylbenzene mass analysis data. (top) Raw mass scan data over the 100 ms scan. (bottom) Mass scale for the top plot. Figure adapted from “A Lithographically Patterned Discrete Planar Electrode Linear Ion Trap Mass Spectrometer,” *J. Microelectromech. Sys.*, (in press).

Another possible issue with resolution is the linear frequency sweep. The relationship between secular frequency and m/z is not linear. Mass analysis of higher mass peaks requires more scan frequency points per unit of scan time in order to improve resolution. Slower mass scans can improve resolution. However, slower scans also decrease signal intensity.

Figure 6-17 shows the 84/86/88 m/z group of dichloromethane with a slower scan. This scan was done at a trapping voltage of 800 V_{0-p} at a frequency of 2.5 MHz. The higher trapping

voltage helped to improve resolution. The noise was higher because the signal intensity was weaker, requiring a higher voltage on the detector. The signal intensity was weaker because the deeper trapping well made it more difficult to eject ions. In fact, the mass peaks at m/z 49/51 were not visible at the higher trapping voltages. As a further cause for increased noise in the figure, averaging multiple scans was unfeasible as higher RF voltage outputs would start to cause heating instabilities in the RF circuit. These instabilities would cause the location of the peak to bounce around a range of several milliseconds. The width of these peaks is approximately one mass unit wide at the FWHM, corresponding to unit mass resolution.

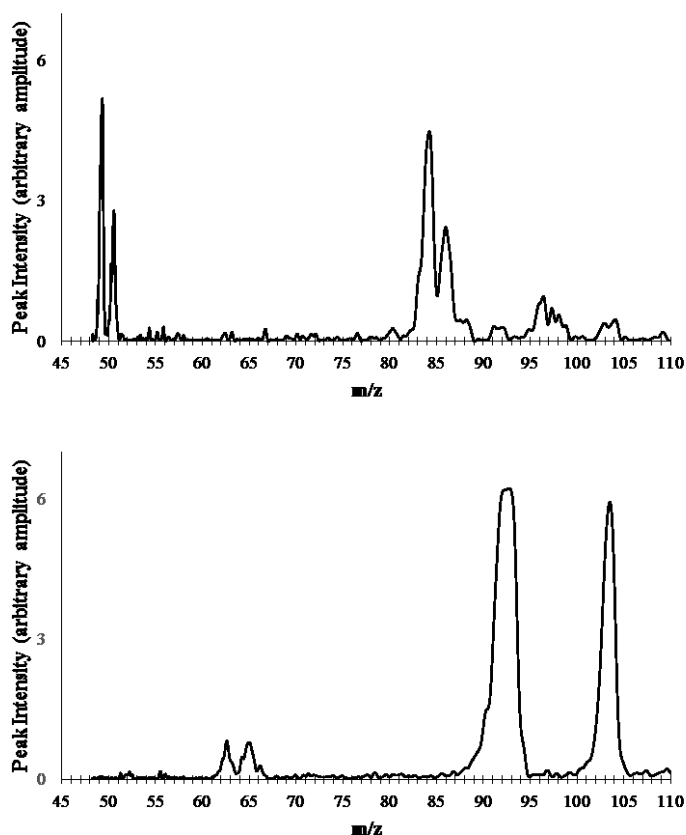


Figure 6-16: Frequency sweep with 2.14% octopole and -2.56% dodecapole of (a) dichloromethane, and (b) toluene.

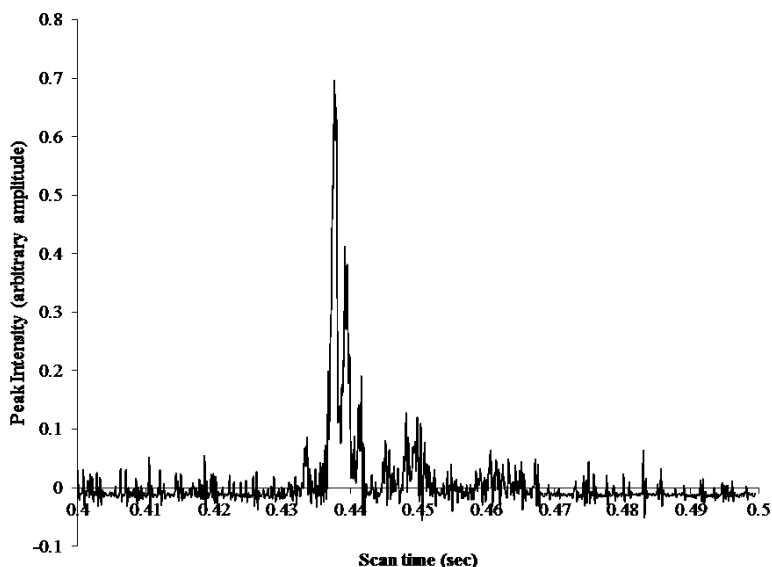


Figure 6-17: A frequency sweep scan of dichloromethane at a higher trapping voltage. The three dominant peaks shown are the m/z 84/86/88 peaks.

6.4.2 Amplitude Ramp

The alternative method for scanning ions out of the trap was to apply a constant AC resonant ejection signal, and ramp the RF trapping amplitude. As the RF amplitude is ramped, the secular frequencies of trapped ions also changes. The RF amplitude ramp performed better than the frequency sweep. One reason for this is because when the RF amplitude is ramped, the secular frequencies of ions also change linearly. This allows for a more constant level of performance across the entire mass range of the instrument.

Figure 6-18 shows mass spectra obtained with dichloromethane and toluene using an RF amplitude ramp from 300-1200 V_{0-p} over a period of 350 ms. An AC signal of 560 kHz at an amplitude of 1.1 V_{0-p} was applied during the scanning phase of the trap. Starting the AC signal 10-20 ms before the start of the RF ramp helped reduce noise during the scan by allowing excess

ions to leak out of the trap prior to beginning a mass-selective scan. Mass analysis data were averaged over 8 separate mass scans, with each scan including the ionization, ion cooling, mass scan, and ion dump phases of the scan.

To compare performance of the PLIT with commercial ion trap instruments, samples of toluene and dichloromethane were analyzed in a Thermo Scientific (Waltham, MA) IT900 GC-MS instrument. The toluene spectra presented in Figure 6-18 show significant agreement between the commercial instrument and the PLIT. Resolution for the toluene peaks in the m/z 90-105 range was 150-160, representing a peak width of 0.5-0.6 mass units.

A low mass range was selected for these experiments based on available power supplies. Higher mass ranges can be achieved using different plate spacing, RF amplitudes, RF frequencies, and ejection AC frequencies. With the current plate spacing, there is a practical limit on the magnitude of the RF amplitude that can be applied to the system. This limit is dictated by the voltage tolerance of the surface mount capacitors in the voltage divider circuit on the PCBs, and by the maximum capable amplitude of the RF power supply.

One significant benefit of the amplitude ramp was in the SNR of the system. Peak signals were much stronger in this configuration, to the point that the detector voltage was turned down to 1500 V for these scans. The stronger peak signals is due to ions being more efficiently resonantly ejected out of the trap by changing the secular frequencies of the ions themselves instead of matching the resonant ejection frequency to a constant secular frequency.

The base peak in toluene is the m/z 92 mass peak. The m/z 91 peak is from the loss of a single hydrogen. The m/z 105 peak is the result of a known ion-molecule reaction common to ion traps. The other peaks are other ion fragments commonly seen with toluene.

Dichloromethane in the commercial instrument showed mass peaks that matched well with the linear ion trap in the m/z 50-90 mass range. However, difficulty in separating air contamination from the sample in the commercial instrument resulted in poor matching for peaks of mass lower than m/z 50.

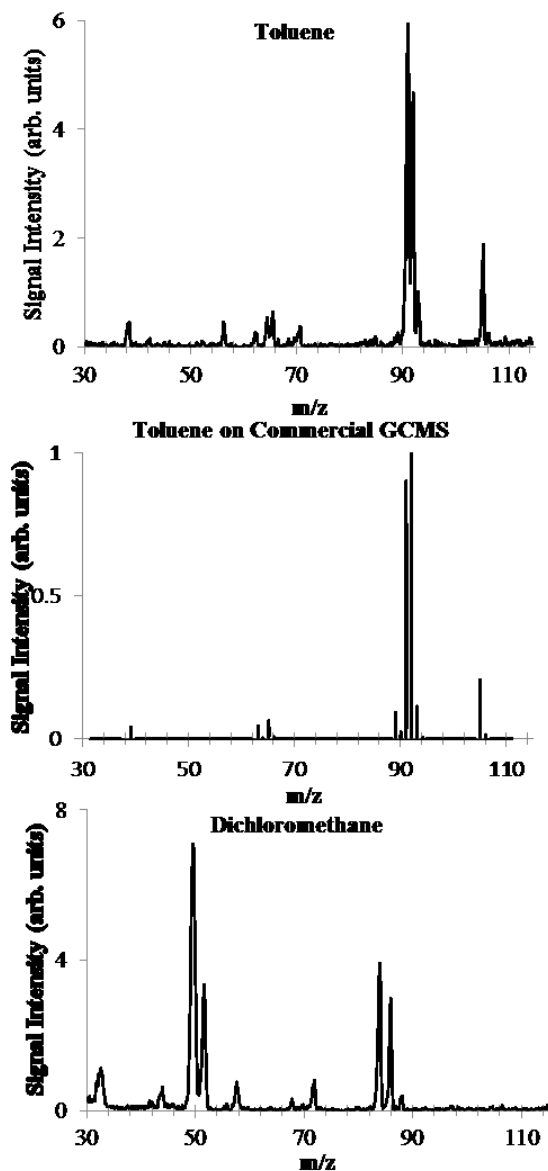


Figure 6-18: (top) Mass spectrum of toluene obtained from the PLIT using a linear RF ramp. (middle) A comparison toluene spectrum from the Thermo Scientific ITQ900. (bottom) Mass spectrum obtained on the PLIT using a linear RF ramp. Figure from "A Lithographically Patterned Discrete Planar Electrode Linear Ion Trap Mass Spectrometer," *J. Microelectromech. Sys.*, (in press).

6.5 Miniaturized Trap Spacing

6.5.1 Theory and Simulation

Miniaturization of conventional machined ion traps requires making smaller electrodes. Simulation work has been done investigating miniaturized patterned planar electrode traps using the toroidal trap as a model [6]. The boundary conditions, or electrode surfaces, must have the same shape to produce fields with the same shape. However, with planar electrode patterns, the potential function on the electrode can be changed without changing the size of the physical electrode. An interesting result of this behavior is illustrated in Figure 6-19, electric field contours in an ion trap with plate spacing, d , of 4, 2, and 1 mm. With a quadratic potential function on both plates, the field between the electrodes remains quadrupolar regardless of the spacing between electrodes. The potential function on the plates in Figure 6-19 is identical for each set, and the resulting field shapes and magnitudes are identical (ignoring edge effects).

For each successively closer set of plates, the trapping frequency increases by a factor of 2, and the helium pressure increases by roughly a factor of 2. Under these conditions, ions are confined to a smaller and smaller volume. This smaller volume shows a decrease in the mean free path, which allows higher operating pressures. As the plates are moved together, the potential well depth perpendicular to the plates (the one used in the PLIT) is reduced. This is due to the potential well being described by the equation

$$D_z \approx q_z \frac{V}{8}. \quad (6.5)$$

This equation shows that the well is dictated by the RF potential V and the trapping parameter q_z . In previous sections, it was discussed that q_z varies linearly with V and varies quadratically with the inverse of the trapping volume radius. If the same values for q_z are to be used in an

experiment between more closely spaced plates, the value of V must be dropped, which in turn decreases the potential well depth. Changing the frequency of the trapping field is the easiest way to compensate for this drop in the potential well depth. A change in frequency allows values of q_z to be maintained without requiring a change in RF voltage.

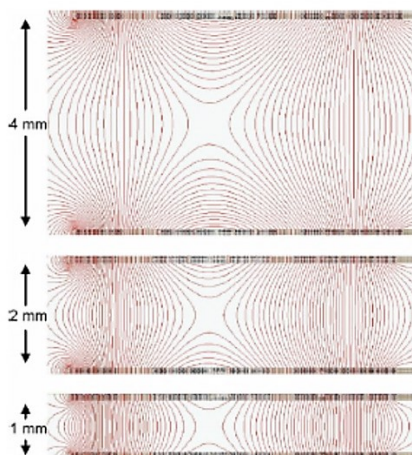


Figure 6-19: Electric fields shown in electrode surfaces spaced at different distances. Figure from “Novel Ion Traps Using Planar Resistive Electrodes: Implications for Miniaturized Mass Analyzers,” *J. Am. Soc. Mass Spectrom.*, 35, pp. 1435-1441, 2008

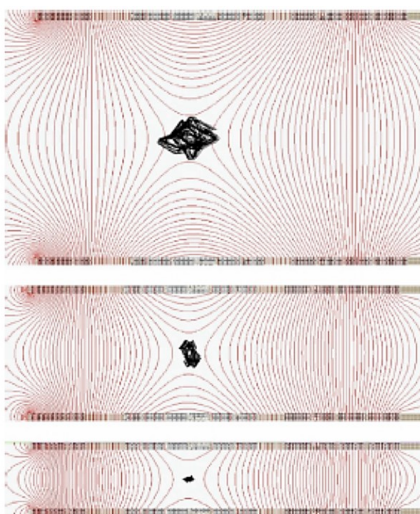


Figure 6-20: Simulated ion trajectories in miniaturized trapping volumes. Figure from “Novel Ion Traps Using Planar Resistive Electrodes: Implications for Miniaturized Mass Analyzers,” *J. Am. Soc. Mass Spectrom.*, 35, pp. 1435-1441, 2008

6.5.2 Experimental Investigations with the PLIT

Experiments have been run with the PLIT to evaluate its feasibility in miniaturizing ion traps. The original spacing of the plates was 4.38 mm. In miniaturization experiments, this distance was changed to a distance of 1.9 8mm. The trapping RF voltage was set to 300 V_{0-p} , with a ramp from 300-775 V_{0-p} over 10 0ms. The trapping frequency was 2.4 MHz. The additional AC resonant ejection signal was 1.1 V_{0-p} at a frequency of 560 kHz. Figure 6-21 shows spectra measured from analyzing perflouorotributylamine, bromonaphthalene, and toluene.

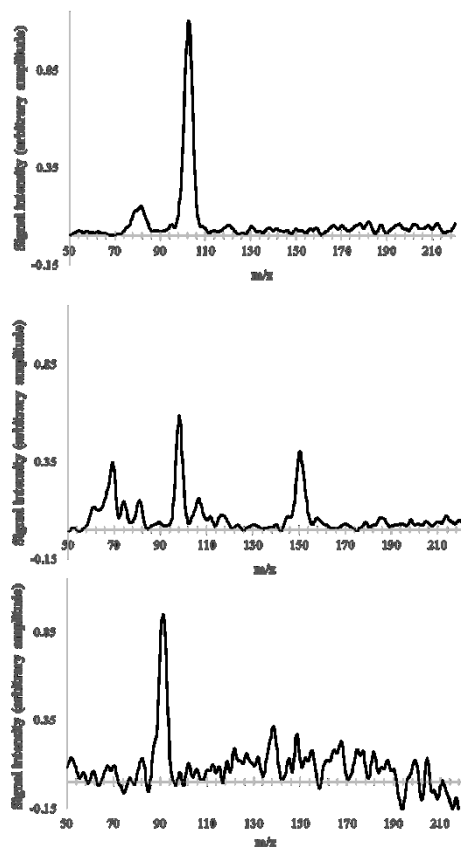


Figure 6-21: Mass spectra taken from the miniaturized planar linear ion trap with (top) PFTBA, (middle) bromonaphthalene, and (bottom) toluene.

The resolution with these spectra is relatively poor, with a FWHM of approximately 4 mass units. This poor resolution is due to the relative lack of flexibility with the current

electrode layout. As the plates are more narrowly spaced, the central electrode over the slit become more and more dominant. This electrode is grounded to ensure a lack of interference on ions leaving the trap. This grounded but increasingly dominant electrode decreases the effective potential within the trap. In order to compensate for this loss of potential, the relative potential on the line pairs must be higher. This constraint limits the flexibility on the electric field higher order multipoles. This in turn leads to fields that have very high A_8 and A_{10} terms, which likely contribute to the loss of resolution. Furthermore, it was found that peripheral components such as the aperture of the electron gun were not well designed for this size of ion trap, creating an overly sensitive experimental setup. However, these results do show the flexibility and viability of the planar linear ion trap for trap miniaturization. It is noteworthy that the same components designed for a 4.38 mm spacing could yield mass spectra for a 1.98 mm spacing arrangement. Relatively small adjustments to the electrode layout, ejection slit width, and electron gun arrangement should yield improved results for the miniaturized trap.

References

- [1] B. J. Hansen, R. J. Niemi, A. R. Hawkins, S. A. Lammert and D. E. Austin, "A Lithographically Patterned Discrete Planar Electrode Linear Ion Trap Mass Spectrometer," *J. Microelectromech. Syst.*, 2013 (in press).
- [2] J. Hager, "A new linear ion trap mass spectrometer," *Rapid Commun. Mass Spectrom.*, vol. 16, pp. 512-526, 2002.
- [3] J. Schwartz, M. Senko and J. Syka, "A two-dimensional quadrupole ion trap mass spectrometer," *J. Am. Soc. Mass Spectrom.*, vol. 13, pp. 659-669, 2002.
- [4] D. Douglas, A. Frank and M. D., "Linear ion traps in mass spectrometry," *Mass Spectrom Rev.*, vol. 24, no. 1, pp. 1-29, 2005.

- [5] Z. Zhang, Y. Peng, H. Quist, J. Wang, B. J. Hansen, A. R. Hawkins and D. E. Austin, "Optimization of Multipole Components in a Planar Paul Trap," in *58th ASMS Conference on Mass Spectrometry*, Salt Lake City, UT, 2010.

7 CONCLUSIONS AND FUTURE WORK

7.1 Conclusions

Ion traps are a significant part in the development of mass spectrometer systems. Ion traps are prime candidates for miniaturized, portable mass spectrometer systems due to their inherent sensitivity and specificity, and because they can be miniaturized and operated at higher pressures relative to other mass analyzer types. Conventional ion traps utilize machined electrode surfaces that are hyperbolic in shape in order to produce the desired ion trapping electric fields. These types of surfaces can be difficult to fabricate with the required level of precision.

This work has presented a method for designing and building planar electrode ion traps. The ion traps presented in this work consist of two planar ceramic surfaces. Because this trap only uses two planar surfaces, it provides a possible pathway to miniaturized traps.

A pattern of electrodes on the ceramic surface is used to create an ion trapping field. The electrodes are patterned using photolithography processes in the BYU cleanroom. By using microfabrication methods in creating the trapping electrodes, the ion trap design is easier to miniaturize and allows the experimental exploration of nonideal trapping fields. The methods for microfabrication presented in Chapter 4 describe processes for spinning and patterning photoresist on substrates with high aspect ratios. The procedures for patterning on a double-sided substrate of a nonstandard size are also described.

In order to create a viable planar electrode ion trap, electrical connections through vias in the substrate are necessary. Generating and connecting different RF potentials to specific electrodes must be done out of the trapping region in order to avoid distorting the shape of the trapping field. A printed circuit board (PCB) with a capacitive voltage divider and gold-coated pogo pins is mounted to the back side of the ceramic substrates in order to connect the desired voltage potentials to the trapping side of the plate.

Four successful trapping designs have been presented: the quadrupole, the toroidal, the coaxial, and the linear trap. In Chapter 5, a quadrupole trap, a toroidal trap, and a coaxial trap were described. The quadrupole trap is the simplest to design and optimize, and currently has the best overall performance out of these designs. The toroidal trap has superior sensitivity due to its increased ion storage volume. The coaxial trap is a hybrid trap that includes quadrupole and toroidal trapping regions within a single trap and demonstrates an ability to transfer ions between traps. In Chapter 6, the planar electrode linear ion trap was presented. This trap combines the simplicity of the quadrupole trap with the increased ion storage capacity of the toroidal trap.

7.2 Future Work

There is room to both improve current traps and use existing trap designs as a foundation for developing future configurations of traps. One weakness in the current ion trap design is the voltage divider network on the PCBs. A high degree of symmetry is required between the two PCBs in order to create a symmetric trapping field. Perfect symmetry is impractical when using two individual voltage divider circuits. A packaging scheme that electrically connects both plates to a single circuit would yield improved symmetry.

Another option for improving performance would be to use voltage-controlled capacitors (varactors) as part of the voltage-divider circuits. Varactors could be used in parallel with other capacitors to make fine adjustments on line voltages and on the trapping field. A possible configuration of the capacitive voltage divider circuit with a varactor is shown in Figure 7-1. The varactor requires a reverse bias to be applied in a way that does not affect the operation of the RF circuit of which it is part, but also prevents the changing RF voltages from changing the capacitance of the varactor. Figure 7-1 also shows a standard circuit used to isolate varactors from RF circuits.

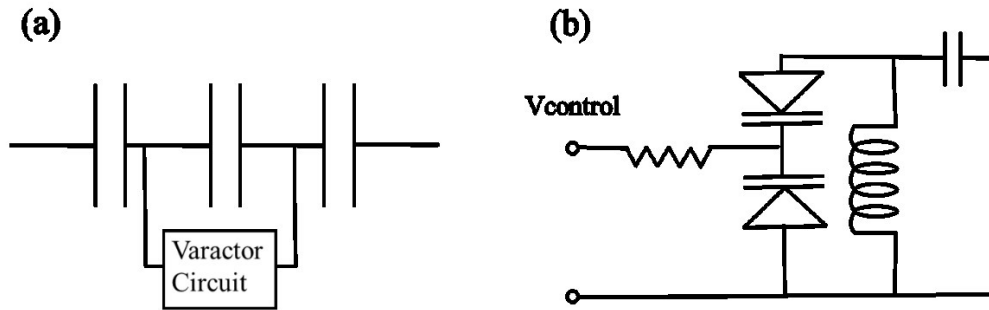


Figure 7-1: (a) The capacitive voltage divider circuit in the ion trap with a varactor used in parallel with standard surface mount capacitors. (b) A commonly used isolating circuit to employ varactors, but isolate them from RF.

The use of varactors would allow real-time adjustments to the trapping field. One aspect of understanding ion trap behavior is knowing the magnitude of the higher order multipole components of the trapping field. Being able to adjust this field and immediately observe experimental results would allow much quicker and more comprehensive understanding of ion trap designs.

Another avenue for real-time analysis of trap performance is with the alignment of the plates themselves. Currently, trap designs used fixed spacers to set the distance between the two electrode surfaces. These spacers are either machined metal pieces or precision sapphire balls.

There will be a necessary amount of tolerance in mounting the plate/PCB assembly together, and this tolerance will mean there are microscopic misalignments of the two electrode surfaces with respect to each other. Real-time adjustment to the plate alignment would be possible using piezoelectric actuators [1]. An arrangement of piezoelectric actuators could be used to make adjustments to plate alignment to achieve optimized alignment.

A piezoelectric alignment system would need to account for five degrees of freedom. These degrees of freedom are illustrated in Figure 7-2. The variables are the spatial coordinates x , y , z , and the angular coordinates ϕ and θ . These are the same variables used in spherical coordinates. Figure 7-3 shows a possible arrangement of the piezoelectric actuators to make adjustments for these coordinates.

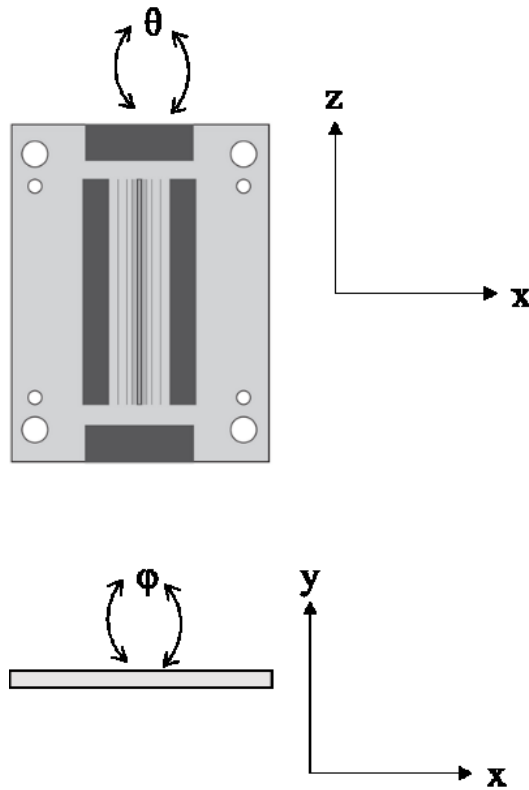


Figure 7-2: The five degrees of freedom of plate alignment.

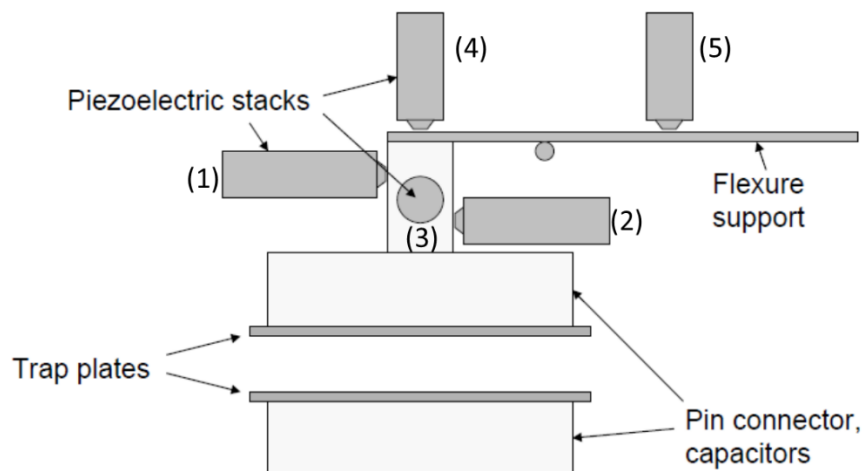


Figure 7-3: Five piezoelectric actuators to allow positions for all directions and angles of plate alignment. Figure adapted from "Novel ion traps using planar resistive electrodes: implications for miniaturized mass analyzers," in 6th Workshop of Harsh-Environment Mass Spectrometry, Cocoa Beach, FL, 2007.

The piezoelectric stacks in Figure 7-3 could be programmed to work together to achieve movements in all five variables of motion. Stacks 1 and 2 could move together to achieve motion in x , and in opposite directions to change θ . Stack 3 can adjust alignment in z . Stack 4 can adjust alignment in y . Stack 5 can adjust ϕ ,

Additionally, by combining piezoelectric actuators with variable capacitors, miniaturized trapping volumes could be explored more easily. Normally, when adjustments in plate spacings are made, this requires both breaking vacuum and replacing the PCBs to create an identically shaped electric trapping field. With piezoelectrics and variable capacitors, the plates could be pushed together with the actuators, and then the capacitive voltage divider circuits could be adjusted to create the same shape of electric trapping field for the miniaturized volume all in vacuum and in real-time.

One more avenue of exploration with the planar electrode linear ion trap is with the electrode layout of this device. Examining this aspect of the design could lead to a more

optimized spacing of the parallel line electrodes for tuning specific multipoles. The parallel lines are currently spaced approximately quadratic at this time. Furthermore, during the course of experiments and designs with the linear ion trap, it was observed that the lines closest to the slit had the greatest effect on the trapping field. A future electrode layout for the linear trap should include a greater concentration of electrodes near the central ejection slit in order to increase the range of fields that can be employed by the design.

Another facet that could be explored is the shape of the DC end bars on the linear ion trap. The current bar shape was chosen to try to best approximate the field of the rectilinear ion trap. However, this may not be the ideal shape. In conventional linear ion traps, for example, the DC axial electrodes have the exact same shape and layout as the trapping electrodes. This helps smooth edge effects in the electric field. A possible arrangement of these electrodes is shown in Figure 7-4. The advantage of this design is that it would match the electrode geometries of the RF and the DC regions, but could also be done with the current designs of plates. Only a small change in the mask for patterning on this side would be necessary. Figure 7-5 shows the difference in the electric field profile when RF and DC electrode geometries are matched, and when they are not. The distortions at the end of the trap length are known as fringe fields.

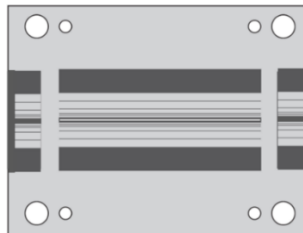


Figure 7-4: Possible electrode arrangement that matches the electrode geometry between the RF and DC regions.

Finally, other methods of ion ejection can be explored in the linear ion trap, methods that actually employ effects seen from the fringe fields at the end of the ion trap. An ion ejection method that ejects ions in a different direction, one that does not require a slit as is currently done, would simplify the microfabrication of the device. Some work has been done to eject ions axially, or along the length of the trap [2] [3] [4].

Axial ejection is possible due to the shape of the RF fields at the edge of the length of the trapping electrodes. When an appropriately located and biased exit lens is placed at the end of the linear ion trap, the field between the trap and the lens (the fringe fields) form a region that is known as the cone of reflection. When ions are excited radially in linear ion traps, as is done in this work, they are also excited axially due to motion coupling along the two axes. If ions are sufficiently excited radially when they interact with the fields in the cone of reflection, they also experience a proportionally greater excitation axially. This axial excitation can be used for mass-selective axial ejection.

Axial ejection provides several benefits. Eliminating the need for an ejection slit would allow more precise and finer electrode patterning right at the center of the trapping volume. The trapping fields themselves would also be more ideal when not having to compensate for a slit. Additionally, most commercially available detectors are geometrically more suited to collect ions from the axial end of the trap rather than from a rectangular ejection area.

Current research using axial ejection in linear ion traps utilizes end plates with a DC bias to create the fringe fields and the cone of reflection. The technique of patterning electrode surfaces opens up new possibilities in not only forming the trapping field, but in shaping the fringe fields by altering the electrode geometry or potentials on the electrode patterns on the end of the planar linear ion trap. Further investigation of this electrode geometry and its effect on the

fringe fields and the cone of reflection could also yield interesting results on mass-selective axial ejection.

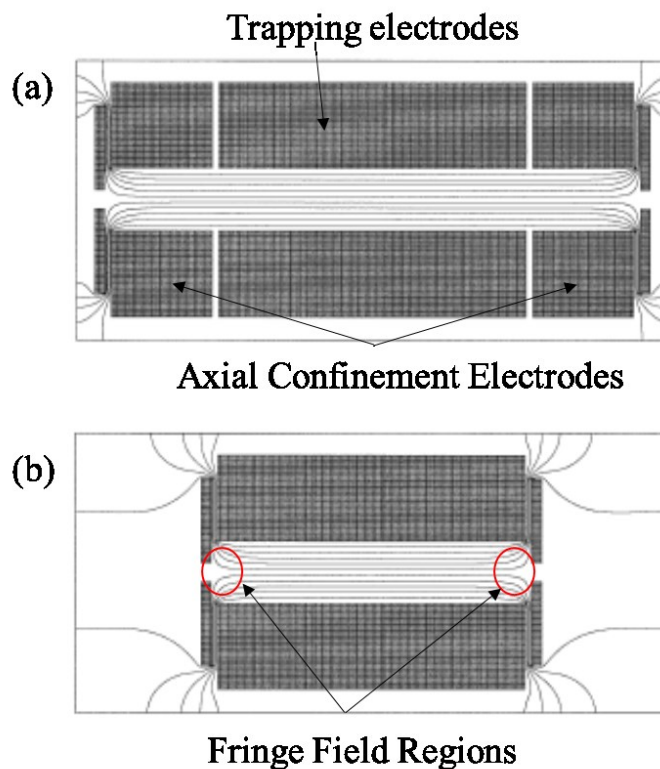


Figure 7-5: Electropotential contour plots for the electric trapping fields in linear ion traps. (a) A linear ion trap with electrode geometries matched. (b) A linear ion trap with biased end plates for axial trapping. Figure adapted from "A two-dimensional quadrupole ion trap mass spectrometer," *J. Am. Soc. Mass Spectrom.*, 13, pp. 659-669, 2002.

References

- [1] D. E. Austin, Y. Peng, M. Wang, M. Lee, A. Hawkins and S. Tolley, "Novel ion traps using planar resistive electrodes: implications for miniaturized mass analyzers," in *6th Workshop of Harsh-Environment Mass Spectrometry*, Cocoa Beach, FL, 2007.
- [2] J. Hager, "A new linear ion trap mass spectrometer," *Rapid Commun. Mass Spectrom.*, vol. 16, pp. 512-526, 2002.

- [3] J. Schwartz, M. Senko and J. Syka, "A two-dimensional quadrupole ion trap mass spectrometer," *J. Am. Soc. Mass Spectrom.*, vol. 13, pp. 659-669, 2002.
- [4] F. A. Londry and J. W. Hager, "Mass selective axial ion ejection from a linear quadrupole ion trap," *J. Amer. Soc. Mass Spectrom.*, vol. 14, pp. 1130-1147, 2003.

APPENDIX A – PUBLICATION LIST

Papers

- [1] D. E. Austin, Y. Peng, **B. J. Hansen**, I. W. Miller, A. L. Rockwood, A. R. Hawkins and S. E. Tolley, "Novel Ion Traps Using Planar Resistive Electrodes: Implications for Miniaturized Mass Analyzers," *J. Am. Soc. Mass Spectrom.*, vol. 19, no. 10, pp. 1435-1441, 2008.
- [2] Z. Zhang, Y. Peng, **B. J. Hansen**, I. W. Miller, M. Wang, M. L. Lee, A. R. Hawkins and D. E. Austin, "Paul Trap Mass Analyzer Consisting of Opposing Microfabricated Electrode Plates," *Anal. Chem.*, vol. 81, no. 13, pp. 5241-5248, 2009.
- [3] D. E. Austin, **B. J. Hansen**, Y. Peng and Z. Zhang, "Multipole expansion in quadrupolar devices comprised of planar electrode arrays," *Int. J. Mass Spectrom.*, vol. 295, no. 3, pp. 153-158, 2010.
- [4] Z. Zhang, H. Quist, Y. Peng, **B. J. Hansen**, J. Wang, A. R. Hawkins and D. E. Austin, "Effects of higher-order multipoles on the performance of a two-plate quadrupole ion trap mass analyzer," *Int. J. Mass Spectrom.*, vol. 299, no. 2-3, pp. 151-157, 2011.
- [5] M. Wang, H. E. Quist, **B. J. Hansen**, Y. Peng, Z. Zhang, A. R. Hawkins and D. E. Austin, "Performance of a Halo Ion Trap Mass Analyzer with Exit Slits for Axial Ejection," *J. Am. Soc. Mass Spectrom.*, vol. 22, no. 2, pp. 369-378, 2011.
- [6] Y. Peng, **B. J. Hansen**, H. Quist, Z. Zhang, M. Wang, A. R. Hawkins and D. E. Austin, "Coaxial Ion Trap Mass Spectrometer: Concentric Toroidal and Quadrupolar Trapping Regions," *Anal. Chem.*, vol. 83, no. 14, pp. 5578-5584, 2011.
- [7] **B. J. Hansen**, R. J. Niemi, A. R. Hawkins, S. A. Lammert and D. E. Austin, "A Lithographically Patterned Discrete Planar Electrode Linear Ion Trap Mass Spectrometer," *J. Microelectromech. Syst.*, (in press), 2013.
- [8] **B. J. Hansen**, A. Li, A. Powell, A. R. Hawkins, D. E. Austin, "Approaches to Miniaturization with a Planar Electrode Ion Trap Mass Spectrometer," (in review).

Conference Proceedings

- [1] S. Tolley, A. R. Hawkins, D. E. Austin, **B. J. Hansen**, E. D. Lee and M. L. Lee, "Coaxial Ion Trap Using Concentric Planar Electrode Arrays," in Pittcon, March 2-6, New Orleans, LA, 2008.
- [2] D. E. Austin, S. Tolley, M. Wang, Y. Peng, **B. Hansen**, A. Hawkins, M. Lee and E. Lee, "New Types of Ion Traps Using Planar Electrode Arrays," in Pittcon, March 2-6, New Orleans, LA, 2008.
- [3] Y. Peng, I. W. Miller, Z. Zhang, **B. Hansen**, M. Wang, S. Tolley, M. Lee, A. Hawkins and D. Austin, "Planar Resistive Electrode Ion Traps," in 56th ASMS Conference on Mass Spectrometry & Allied Topics, Denver, CO, 2008.
- [4] Y. Peng, I. W. Miller, Z. Zhang, **B. J. Hansen**, M. Wang, S. E. Tolley, M. L. Lee, A. R. Hawkins and D. E. Austin, "Planar Resistive Electrode Ion Traps," in Annual Meeting of the American Society for Mass Spectrometry, Denver, Colorado, June 1-5, 2008.
- [5] E. D. Lee, S. E. Tolley, A. R. Hawkins, D. E. Austin, **B. J. Hansen**, M. L. Lee and D. L. Later, "Planar Electrode Array Ion Traps including a unique Coaxial Geometry," in 56th ASMS Conference on Mass Spectrometry & Allied Topics, Denver, CO, 2008.
- [6] Y. Peng, I. W. Miller, Z. Zhang, **B. J. Hansen**, S. E. Tolley, M. L. Lee, A. R. Hawkins and D. E. Austin, "Novel Planar Ion Traps with Resistive Electrodes," in Joint Northwest & Rocky Mountain Regional Meeting of the American Chemical Society, Park City, UT, 2008.
- [7] M. Wang, D. E. Austin, S. E. Tolley, **B. J. Hansen**, A. R. Hawkins and M. Lee, "Design and Performance of a Halo Ion Trap Mass Analyzer," in Joint Northwest & Rocky Mountain Regional Meeting of the American Chemical Society, Park City, UT, 2008.
- [8] Y. Peng, Z. Zhang, I. Miller, **B. Hansen**, S. E. Tolley, M. L. Lee, A. R. Hawkins and D. Austin, "Designing Custom Electric Fields in Resistive Electrode Ion Traps," in Pittcon, Chicago, IL, 2009.
- [9] D. E. Austin, Z. Zhang, Y. Peng, **B. J. Hansen**, M. Wang, M. L. Lee and A. R. Hawkins, "Planar Electrode Ion traps," in Annual Meeting of the American Society for Mass Spectrometry, Philadelphia, PA, May 31 - June 2, 2009.
- [10] Z. Zhang, Y. Peng, M. Wang, **B. J. Hansen**, A. R. Hawkins and D. E. Austin, "Ion Trap Mass Analyzers Made Using Microfabricated Electrode Plates," in The 18th International Mass Spectrometry Conference, Bremen, Germany, Aug 30-Sept 4, 2009.
- [11] D. E. Austin, Z. Zhang, Y. Peng, **B. Hansen**, A. Hawkins and M. Wang, "Progress in Two-plate Ion Trap Mass Analyzers," in 7th Harsh Environment Mass Spectrometry Workshop, Santa Barbara, CA, Sept 21-24, 2009.

- [12] D. E. Austin, **B. J. Hansen** and et. al, "Microfabricated Planar Electrode Ion Traps: Combining Accuracy with Simplicity for Miniaturization," in Pittcon, Orlando, FL, Feb 28-Mar 4, 2010.
- [13] M. Wang, D. E. Austin, **B. J. Hansen**, H. E. Quist, A. R. Hawkins, E. D. Lee and M. L. Lee, "Custom Electric Fields in a Halo Ion Trap Mass Analyzer," in Pittcon, Orlando, FL, 2010.
- [14] Z. Zhang, Y. Peng, **B. J. Hansen**, M. Wang, M. L. Lee, A. R. Hawkins and D. E. Austin, "High Mass Resolution and Tandem Capabilities of a Microfabricated Two-Plate Paul Trap Mass Spectrometer," in Pittcon, Orlando, FL, 2010.
- [15] Y. Peng, Z. Zhang, **B. J. Hansen**, M. Wang, M. L. Lee, A. R. Hawkins and D. E. Austin, "Coaxial Ion Trap: Two Superimposed Trapping Regions in One Analyzer," in Pittcon, Orlando, FL, 2010.
- [16] D. E. Austin, **B. J. Hansen** and et. al, "Microfabricated planar ion trap mass spectrometers," in Pittcon, Atlanta, GA, Mar 13-17, 2011.
- [17] D. E. Austin, Z. Zhang, **B. J. Hansen** and Y. Peng, "Planar Quadrupole and Coaxial Ion Trap Mass Analyzers: Effects of Field SHape," in 59th annual conference of the American Society for Mass Spectrometry, Denver, CO, June 5-9, 2011.
- [18] **B. J. Hansen**, H. E. Quist, A. R. Hawkins, Z. Zhang, Y. Peng, M. Wang, M. L. Lee and D. E. Austin, "Quadrupole Ion Traps Realized by Planar Microfabricated Electrodes for Compensation of High Order Multipole Effects," in Pittcon, Orlando, FL, 2010.
- [19] Z. Zhang, Y. Peng, H. Quist, J. Wang, **B. J. Hansen**, A. R. Hawkins and D. E. Austin, "Optimization of Multipole Components in a Planar Paul Trap," in 58th ASMS Conference on Mass Spectrometry, Salt Lake City, UT, 2010.
- [20] D. E. Austin, Y. Peng, Z. Zhang, **B. J. Hansen** and A. R. Hawkins, "Ion Trap Mass Analyzers Consisting of Lithographically Patterned Plates," in 2011 FACSS Meeting, Oct 2-6, 2011.
- [21] **B. Hansen**, H. Quist, B. Barney, A. Hawkins and D. Austin, "A Linear-type Ion Trap Realized with Two Lithographically Patterned Substrates," in 58th ASMS Conference on Mass Spectrometry, Salt Lake City, UT, 2010.
- [22] D. E. Austin, Z. Zhang, **B. J. Hansen**, Y. Peng and A. R. Hawkins, "Microfabricated ion trap mass spectrometers for planetary missions: the planar Paul trap and the coaxial ion trap," in International Workshop on Instrumentation for Planetary Missions, Greenbelt, MD, Oct 10-12, 2012.
- [23] Y. Peng, Z. Zhang, **B. J. Hansen**, M. Wang, M. Lee, A. R. Hawkins and D. E. Austin, "Design and Performance of a Coaxial Ion Trap: Transferring Ions between Two Trapping Regions in One Mass Analyzer," in 58th ASMS Conference on Mass Spectrometry, Salt Lake City, UT, 2010.

Publications unrelated to Ion Traps

- [1] Z. Liu, R. Brant, Y. Yahagi, **B. Hansen**, B. Harteneck, J. Bokor, S. Cabrini, A. Hawkins, H. Schmidt, "Detecting single nanomagnet dynamics beyond the diffraction limit in varying magnetostatic environments," *App. Phys. Lett.*, vol. 98, 052502, (2011).
- [2] Z. Liu, R. Brandt, **B. Hansen**, B. Harteneck, S. Cabrini, A. R. Hawkins, J. Bokor, H. Schmidt, "Detecting single nanomagnet dynamics in varying magnetostatic environments," INTERMAG conference, Sacramento, CA, May 4-8, 2009.
- [3] Z. Liu, R. Brandt, B. Harteneck, **B. Hansen**, S. Cabrini, J. Bokor, A. R. Hawkins, H. Schmidt, "Detecting dynamic magnetic information beyond the optical spatial resolution in a Ni nanomagnet array", 53rd Conference on Magnetism and Magnetic Materials, Austin, TX, Nov 10-14, 2008.
- [4] **B. J. Hansen**, C. J. Carron, A. R. Hawkins, S. M. Schultz, B. D. Jensen, "Plastic-latching accelerometer based on bistable compliant mechanisms," *Smart Materials and Structures*, vol. 16, pp. 1967-1972, (2007).
- [5] **B. J. Hansen**, C. J. Carron, A. R. Hawkins, S. M. Schultz, "Zero-power shock sensors using bistable compliant mechanisms," *Proceedings of the SPIE* 6525, 65251W, (2007).

APPENDIX B – MICROFABRICATION RECIPES

These procedures were written for the BYU IML in May 2012. They were intended for new students who were unfamiliar with microfabrication equipment.

B.1 Plate Cleaning

1. If recycling old plates, stick plate in appropriate metal etchant to remove old metal (Aluminum etch should be at $\sim 50^{\circ}\text{C}$).
2. Rinse in bath on acid bench for ~ 10 minutes (every rinse step is ~ 10 minutes).
3. Scrub plates with a mixture of alconox (detergent) and water.
4. Rinse.
5. Spray plates with acetone and Isopropanol (IPA), remembering not to allow the acetone to dry on the plate before spraying with isopropanol.
6. Rinse.
7. Soak for 2 minutes in a 10:1 water:HCl (hydrochloric acid) mixture. The plates can stay in the white carrier on this step.
8. Rinse.
9. Soak for 2 minutes in a 10:1 water:NH₄OH (Ammonium Hydroxide) mixture. The plates can stay in the white carrier for this step.
10. Rinse.
11. Remove plates one at a time from the water to avoid letting the water dry and leave water spots on the plate. Rinse plate with IPA. Place in metal holder that we use in ebeam planetary during Ge deposition. Place in oven for 20-30 minutes. This will dehydrate the plates. By this point, there shouldn't be any visible spots on the plates.

B.2 Metal Deposition

1. Plates are placed in oven immediately prior to metal deposition. If this step is done on a different day as the plate cleaning, place plates in oven for ~ 10 minutes.
2. Do a 15-20 second O₂ descum in the planer etch 2 (PE2).

3. Tape plates on to 4" wafers using the brown vacuum tape.
4. Turn on the power to the thermal evaporator. This switch is on the left side of the machine. Turn on the vent switch until air is felt coming out of the bell jar. Turn off the vent. Set the bell jar switch to "raise". After a slight delay, the bell jar will begin to rise. Flip the switch back to the middle position once the jar is appropriately high to load wafers into the planetary.
5. Place wafers in the planetary on the thermal evaporator.
6. Load three aluminum pellets into a tungsten boat. Use a little aluminum wire to wrap and secure the pellets to the boat to ensure that they do not fall off if the machine vibrates.
7. Insert the boat into one of the three slots on the thermal evaporator (usually the center slot).
8. Ensure the thick metal ring/collar is placed back around the boat area inside the evaporator.
9. Turn on the crystal monitor (the box that sits left of the bell jar).
10. Check the life of the crystal by hitting the button on the number pad with "XTAL" over it. Mark down the crystal life (it is a percent value) on the log. If it is getting close to 100%, get someone to help you change the crystal.
11. Turn on the green "START" button on the wall to turn on the roughing pump.
12. Before lowering the bell jar, take a paper towel wet with IPA, and wipe all the edge of the bell jar down to ensure that there is no debris that will interfere with the rubber seal the bell jar will make with the base.
13. Move the bell jar switch to "lower". After a slight delay, the jar will lower.
14. Turn on the roughing pump switch. I think it is labeled "rough". The pressure will slowly start to drop on the gauge just to the left of the bell jar. You will use this pump to get down to <100 mTorr.
15. Once pressure is below 100 mTorr. TURN OFF the roughing pump on the evaporator.
16. Turn on the cryo pump with the switch labeled "Hi-Vac". NEVER run these pumps at the same time. Allow any "hissing" that occurs when turning off a pump to finish before turning on the other pump.
17. On the top left of the evaporator is a series of three rectangular buttons. These control the ion gauge, which you will use to measure the pressure now that you are out of the range of the roughing pump gauge. Press the power button, then press the filament button to turn on this gauge. The gauge will register about a foot to the right of those buttons. The dial to the right of the gauge will tell you the exponent value of the pressure you are reading (4 means 10^{-4} torr, 5 means 10^{-5} torr, etc.) This dial should start at the 4, and be lowered as the pressure drops accordingly. The lower

you get on the pressure, the better, but you should be at least somewhere in the 10^{-6} range before depositing. Generally in the 5×10^{-6} is a good pressure to get down to. This will probably take 20-30 minutes of pumping with the hi-vac.

18. When you are ready to deposit, turn on the planetary with a switch on the right side of the machine. When you flip this switch, you will see a gear on the very top of the bell jar start spinning.
19. Close the shutter if it is not closed already.
20. Turn on the power for the current. This switch is located in the middle top area on the machine.
21. Press the Open and Close buttons on the crystal monitor to zero out the display. Ensure that you are programmed for depositing aluminum. This means the film number (will read 1, 2, or 3) should correspond with the label placed on the crystal monitor.
22. Slowly turn up the current (at a rate of ~ 10 amps /10 seconds) using the large round dial in the middle bottom area of the machine. Be sure the small dial to the right of the current dial correctly corresponds with the boat position you are using (front, middle, or back).
23. Aluminum will start to melt and evaporate in the 275-325 amp range. Find the appropriate angle inside the bell jar window to look at the boat and see when melting occurs (this angle can be a little difficult to find, and you likely won't see it before you reach 250 amps). When the pellets melt, the boat will periodically go dark and then will begin to glow orange again. Once it appears this has happened, open the shutter. You should start to see a deposition rate register on the crystal monitor. If you don't slowly raise the current until you do.
24. Deposit at a rate of ~ 5 -10 angstroms/second. Generally with these plate, we want as thick of an aluminum layer as we can get. Make subtle adjustments on the current to maintain the deposition rate.
25. Around 400-600nm (will read 4-6 on the crystal monitor), the deposition rate should start to quickly drop. This means the boat is running low on aluminum. Slowly, but steadily turn down the current all the way to 0. Turn off the power for the current supply.
26. Let machine sit for 5-10 minutes to allow the boat to cool. This will help the boat last longer should you want to use it in a later run.
27. Turn off the power to the ion gauge and the planetary.
28. TURN OFF the cryo pump (hi-vac). NEVER run the cryo pump when either the roughing pump or the vent switches are on.
29. After any "hissing" that occurs when turning off the cryo pump, vent the bell jar.
30. Raise the bell jar and remove wafers.

31. Detach ceramic plates from the wafers, flip the plates over, and retape them to the wafers to coat the other side of the plates.
32. Repeat the metal deposition process for the second side of the wafers.
33. When done, turn off the crystal monitor, run the roughing pump for a couple of minutes (the machine shouldn't be left open to atmosphere indefinitely, in the 1000-2000 mTorr range is fine), turn off the roughing pump switch on the wall, turn off the power to the evaporator.

B.3 Lithography

This lithography process is for the planar Paul trap plates. See B.4 for specialized toroidal trap and linear trap spinning recipes. All other steps are identical.

1. Remove plates from wafers used in metal deposition step.
2. Place plates in metal carriers, and dehydrate in oven for ~5-10 minutes.
3. Using brown vacuum tape, attach a single plate to a wafer. Try to attach the plate right in the center of the wafer. For the first run, use the side that will match up with the squares mask first, and the rings second.
4. Turn on the two hot plates on the spinner bench. One will be at 90°C, the other at 110°C.
5. Program the spinner so that it will spin for 1 minute, 4000 rpm, and acceleration set at 009. The F1 button is used to change the parameters. (Note: See B.4 for spinning program for toroidal or linear ion trap spinning program.
6. Place wafer with taped on plate on spinner. Offset the wafer so that the plate is centered over the spinning axis (the better you do step 3, the easier this will be). Press the vacuum button to secure the wafer to the spinner.
7. Put 10-20 drops of HMDS on the plate (enough to cover the plate). Spin for 5-8 seconds at spin settings from step 5, enough to get the HMDS layer on. Manually stop the spinning with the run/stop button.
8. Reset the timer by pressing the F1 button twice.
9. Cover the plate in AZ3330 photoresist, making sure to fill in the holes and cover the plate surface.
10. Spin for 60 seconds.
11. Raise the lid, and press the vacuum button to turn off the vacuum. "Soft bake" the wafer (place on the 90° hotplate) for 60 seconds.
12. Program aligner with the following parameters: 10-12 seconds exposure, soft contact, soft contact delay of 8 seconds, manual align.

13. Run the short program setting on the aligner (this will guide you through the process of loading the wafer and mask). The shiny side of the mask should be up in this process. If you set the mask down while working, set it on a paper towel with the shiny side down.
14. Adjust microscopes to be as close together as possible. Align mask with plate. If the joysticks aren't letting you move the screen how you would expect, you may need to toggle the buttons on the right joystick (cont. step, single step) to a different mode. I think you want cont step on and single step off. Use the buttons on the left joystick to toggle moving the mask, the microscope, or a combination of the two. Use the panel underneath the screen to adjust which microscope view is displayed on the screen, and to focus if necessary.
15. When ready to expose, turn off the cont mode button on the right joystick. The expose button on the right side of the machine will light up. Press the expose button to begin the exposure process.
16. Follow the screen prompt instructions to unload the mask and the wafer. Spray down the mask with acetone and IPA when you are done, being careful not to scratch the surface.
17. Prepare the wafers to be placed in developer. Remove the tape. Grab a brush, place 3 or 4 drops of AZ3330 on the unexposed side of the plate, and paint over the plate. Developer will slowly etch aluminum. Place a paper towel on the 90° hot plate, and place the plate with the recently exposed side down onto the hotplate, and bake for 3 minutes.
18. Place wafer in 300 MIF developer in a glass container. Develop until it seems all the undesired resist appears to be removed. This usually takes anywhere from 30 seconds to a minute, but can take longer from time to time.
19. Inspect under microscope to make sure everything looks ok.
20. Bake wafer on 110° hotplate for 3 minutes with exposed side up.
21. Once again look over both sides of plate, and make sure resist looks like it will protect the necessary parts of the plate in etchant.
22. Place plate in aluminum etchant heated to 50°C (you could start this heating up earlier in the process) until all of the excess aluminum is etched away.
23. Again inspect the plate under the microscope and make sure all of the desired aluminum is etched away.
24. Remove photoresist from both sides with an acetone/IPA rinse, followed by a 15-20 second O₂ plasma descum in the PE2 on both sides of the plate.
25. If you pattern the square side first, you can check to see if the electrical connections are all in place. When you have a patterned square side, and solid aluminum on the other side, you should be able to take an ohm meter and measure a small amount of resistance when touching different squares on the plate.

26. Repeat process (from step 2-24) for patterning the ring side of the plate.
27. Deposit 100nm of germanium on the trapping side with the electron beam evaporator.

B.4 Specialized Spin Recipes

B.4.1 Toroidal Trap (large central hole)

1. Identical spin program to planar Paul trap.
2. Do not cover large central hole in resist.

B.4.2 Toroidal Trap (slit design)

This design requires a slow ramp to a slow spin, followed by a long high speed spin.

1. 30 second spin, 1500 rpm, slow acceleration (110rpm/sec).
2. Ramp up to 5000 rpm at acceleration of 1500rpm/sec.
3. Spin for 3:00.

Pattern is not flawless, but it is consistent and nearly perfect. Redesigns in electrode and slit width would be required for flawless photoresist spinning.

B.4.3 Linear Trap

This design requires a slow acceleration to a moderate speed spin.

1. Spin for 1:00 at 4000rpm, acceleration is 110rpm/sec.
2. Any photoresist bulges should lie within the patterned electrode covering the slit. If excessive bulges exist, increase speed and time.
3. Longer slits require a spin program similar to the toroidal trap in B.4.2.

APPENDIX C – GERMANIUM AND MULTIPOLE CALCULATION CONVENTIONS

This document was created in September 2009 as a way to establish uniform calculation methods of the resistive electrode surfaces and the higher order multipole components of the potential function of the various ion traps being developed at BYU. One key of the procedure is to ensure proper boundary conditions to allow for accurate calculations. This is noted in the amount of points in a SIMION array that must extend out of the trapping region.

C.1 SIMION

1. Use 1 grid unit = 10 μm .
2. Model fields simulating the Germanium layer.
3. Draw bars all the way across Potential Array (PA) and set voltages.
4. Refine Array using a low convergence objective.
5. Modify the Array again.
6. Use the Find button to highlight all points greater than an arbitrary large voltage.
7. Change non-electrode points between bars to electrode (with Find button on).
8. Change excess electrode points to non-electrode (no longer will have bars going across entire PA).
9. Add extra features (hole in middle of plate, spacers, shields behind hole, etc.) **Note:** The number of points beyond the hole (outside of the trap) should be 8x the number of points that make the width of the center hole.
10. Save PA, Refine again using Iteration Limit of at least 100,000, then **Save Again after refining the second time.**
11. Fly a neutral particle all the way through the center of the trap.
12. **Measure the field from inner plate surface to inner plate surface.**
13. Use computational quality of 0.
14. Record position and potential, use Ion's Every Time Step.
15. Normalize the voltages.

C.2 Matlab

1. Use a 20th order fit with the *polyfit* function. The function in matlab will look something like `c = polyfit(x,y,20)`, with x being particle position and y being the normalized voltage at that position. The value c will become an array that is all the coefficients of the equation of the field.
2. In calculating higher order pole percents, base percentage off of the quadrupole term ($A4/A2 =$ octupole percent, $A6/A2 =$ dodecapole percent, etc.)

C.3 Sample MATLAB code

```
clear all;
```

```
close all;
```

```
% used computation quality 0 for ion flight on SIMION, with 10um/grid point
```

```
% Total distance between plates is 4.38mm, (r0 of 2.19mm)
```

```
% 8 mm ion flying distance (+- 4.0mm)
```

```
% read in points of potential function calculated from SIMION from plate
```

```
% surface to plate surface. In this case from +2.19mm to -2.19mm
```

```
x = xlsread('D:\Work\Angle Spacing Field and Octupole Calculation','a222:a689');
```

```
y = xlsread('D:\Work\Angle Spacing Field and Octupole Calculation','g222:g689');
```

```
% read in voltages used from spreadsheet to allow record of test voltages
```

```
voltages = xlsread('D:\Work\Angle Spacing Field and Octupole Calculation','b5:f5');
```

```
% calculate coefficients of fitted polynomial
```

```
c = polyfit(x,y,20);
```

```
A2 = c(length(c)-2);
```

```
A4 = c(length(c)-4);
```

```

A6 = c(length(c)-6);

% display results of calculations
voltages
A2
octopole_percent = A4/A2 * 100
dodecapole_percent = A6/A2 * 100
c

%%%%%%%%%%%%%%%%%%%%%%%%%%%%%%%%%%%%%%%%%%%%%%%%%%%%%%%%%%%%%%%%%%%%%%%%
%%%%%%%%%%%%%%%%%%%%%%%%%%%%%%%%%%%%%%%%%%%%%%%%%%%%%%%%%%%%%%%%%%%%%%%%
%%%%%% Graphical test of calculated function to verify validity of
% results calculated in Excel, this is only for verifacation
% purposes and is not critical to multipole calculations%%%%%%%%

% calculated fitted polynomial and plot with data points
fitx = min(x):(max(x)-min(x))/length(x):max(x);
fity = 0;
for n = 1:length(c)
    fity = (c(n).*fitx.^(length(c)-n)) + fity;
end
% normalize to data points and plot
fity = fity./max(fity);
fity = fity.*max(potentials);
plot(x,y,fitx,fity);
legend('Actual data','Fitted poly');

```